

Meson Properties in the Quark Model: A Look at Some Outstanding Problems

by

Harry G. Blundell, B.Sc.

A thesis submitted to
the Faculty of Graduate Studies and Research
in partial fulfilment of
the requirements for the degree of
Doctor of Philosophy

Ottawa-Carleton Institute for Physics

Department of Physics

Carleton University

Ottawa, Ontario, Canada

July 19, 1996

©Harry G. Blundell, 1996

The undersigned recommend to
the Faculty of Graduate Studies and Research
acceptance of the thesis

Meson Properties in the Quark Model: A Look at Some Outstanding Problems

submitted by **Harry G. Blundell, B.Sc.**
in partial fulfilment of the requirements for
the degree of Doctor of Philosophy

Chair, Department of Physics

Thesis Supervisor

External Examiner

Carleton University

Date _____

Abstract

This thesis examines three problems of the quark model, split between two general areas.

The first area involves models of meson decay. The calculations of decay widths in two such models, the 3P_0 model and the flux-tube breaking model, were automated so that they could be easily done for any decay. The models were then used to investigate two particular problems. The first is the nature of the $f_4(2220)$ – although tentatively identified as the 3F_4 $s\bar{s}$ meson by the Particle Data Group, its identity has been uncertain since its discovery in 1983. An exhaustive calculation of the strong decay modes of the 3F_2 and 3F_4 $s\bar{s}$ mesons was performed in order to examine the possibility that the state is a meson. It was found that the $f_4(2220)$ cannot be the 3F_2 $s\bar{s}$ meson, and is unlikely to be the 3F_4 , although given the uncertainties of the models the latter possibility cannot be ruled out. Instead the following explanation is proposed: that the broad state seen in hadron beam experiments is the 3F_4 $s\bar{s}$ meson, and the narrow state seen in J/ψ radiative decay is a glueball. Further experimental data is needed to finally identify the $f_4(2220)$.

The second problem investigated using meson decay models is the determination of the mixing angle between the $K_1(1270)$ and $K_1(1400)$ mesons. This was done by comparing predictions of the meson decay models for five partial decay widths and two ratios of D to S amplitudes to experimental data. A mixing angle of approximately 44° was extracted, and the implications to the quark model Hamiltonian are discussed.

The third problem falls in the second general area: final state interactions (FSI's). The effect of the strong interactions between the outgoing pions was examined for the reaction $\gamma\gamma \rightarrow \pi\pi$ near threshold. For charged pions, the experimental data agrees with the results calculated both with and without the effects of FSI's – better

data is need to distinguish between the two. However, agreement was not obtained for neutral pions. It is believed that the discrepancy may be due to the effects of resonance production. If this proves to be the case, then the techniques used in this work could be extended to try to understand a long-standing puzzle: the nature of the unexplained structures seen in the cross sections of $\gamma\gamma \rightarrow$ two vector mesons.

Acknowledgments

This work was made possible by the support of a large number of people. I would especially like to thank my supervisor Stephen Godfrey, for doing those things that supervisors do. Also our collaborator (on the $\gamma\gamma \rightarrow \pi\pi$ work) Eric Swanson. A large number of other people answered physics questions (or tried to) – in particular Peter Watson and Mike Doncheski (Mike also read this thesis for me). A number of people answered computer questions – in particular Mike Boyce, Matthew Jones, Alan Barney and Wade Xiong. The theory post-docs and my fellow grad students in physics kept life interesting – in particular Mike Boyce, Alan Dekok, Mike Doncheski, Larry Gates, Matthew Jones, Ted Lawrence, Greg Stuart, Steve Taylor, and Sherry Towers. And finally, thanks to Deborah Schneider, for inspiring me to actually finish.

Contents

Abstract	iii
Acknowledgments	v
List of Tables	ix
List of Figures	xi
1 Introduction	1
1.1 The Standard Model of Particle Physics	2
1.1.1 The Particles that Constitute Matter	2
1.1.2 The Interactions	4
1.2 The Hadrons	6
1.2.1 The Mesons	8
1.2.2 The Quark Model	9
1.3 The Work of this Thesis	12
2 Two Models of Meson Decay	15
2.1 The 3P_0 Model of Meson Decay	15
2.2 Calculating Meson Decay Widths with the 3P_0 Model	19
2.3 The Flux-tube Breaking Model of Meson Decay	22
2.4 Calculating Meson Decay Widths with the Flux-tube Breaking Model	25
3 Models of Meson Decay: Two Applications	31

3.1	Setting the Parameters of the Models	31
3.2	The $f_4(2220)$ Reexamined - What Is it Really?	43
3.3	Constraining the K_1 Mixing Angle	53
4	Effects of Final State Interactions	60
4.1	Introduction to Final State Interactions	60
4.2	Solving the Schrödinger Equation with the FSI Potential	61
4.3	The Fermi Approximation	63
4.4	Applying FSI's to the Flux-tube Breaking Model of Meson Decay . .	64
4.5	Applying FSI's to QED Amplitudes	66
5	Final State Interactions: An Application	70
5.1	The Interaction $\gamma\gamma \rightarrow \pi\pi$	70
5.2	$\gamma\gamma \rightarrow \pi^+\pi^-$ in Tree-level Scalar QED	73
5.3	Applying the FSI Correction	76
5.3.1	The Effective Potentials We Use	76
5.3.2	The FSI Apparatus Applied to the Pions	80
5.3.3	The Problem of Limited Polar Acceptance	83
5.3.4	Numerical Details	85
5.4	Results	85
6	Conclusions	93
A	Some Tools of Particle Physics	96
A.1	Cross-section and Width	96
A.2	Feynman Diagrams	97
A.3	Clebsch-Gordan Coefficients and the Wigner nj Symbols	98
A.4	Conservation Laws and Invariance Principles	99
A.5	Relative Coordinates	100

A.6	The OZI Rule	101
A.7	Meson Mixings	101
B	Meson Wavefunctions Used in this Work	104
B.1	Space Wavefunctions	104
B.2	Flavour Wavefunctions	106
C	Field Theory Conventions Used in this Work	108
D	Evaluating the Colour, Flavour and Spin Overlaps for Models of Meson Decay	110
D.1	Colour Overlap	110
D.2	Flavour Overlap	112
D.3	Spin Overlap	113
E	Converting to Partial Wave Amplitudes for Models of Meson Decay	116
E.1	Converting by a Recoupling Calculation	117
E.2	Converting with the Jacob-Wick Formula	118
Bibliography		119

List of Tables

1.1	Masses of the quarks and leptons	3
1.2	The known meson spectrum for the light quarks	10
3.1	The 28 meson decays used in our fits of the decay models' parameters	34
3.2	The details of the various fits of the decay models' parameters, and the resulting χ^2/dof	40
3.3	The values of $\bar{\gamma}$, σ_γ and $\sigma_\gamma/\bar{\gamma}$ for the 28 decays used in the fits, where the γ (γ_0) value for a decay matches the model prediction to the experimental value	41
3.4	Summary of measurements of the $f_4(2220)$	45
3.5	The calculated partial decay widths and total width of the $f_4(2050)$ meson. The available experimental results are also shown	47
3.6	The calculated partial decay widths and total width of the $K_4^*(2045)$ meson. The available experimental results are also shown	48
3.7	The calculated partial decay widths and total width of the 3F_2 $s\bar{s}$ meson	49
3.8	The calculated partial decay widths and total width of the 3F_4 $s\bar{s}$ meson	50
3.9	The calculated partial decay widths and total width of the 3F_3 $s\bar{s}$ meson	51

3.10 The partial decay widths and ratios of D to S amplitudes used in our fits of the $K_1(1270)$ and $K_1(1400)$ mixing angle θ_K	57
5.1 The parameters of the potentials used in this work	80

List of Figures

2.1	The two possible diagrams contributing to the meson decay $A \rightarrow BC$ in the 3P_0 model	16
2.2	The position-space coordinates used in the flux-tube model	23
3.1	Ratios of the predictions of the 3P_0 model of meson decay to the experimental values, for the widths of the 28 decays used in the fits. In this figure SHO wavefunctions with a common β were used	35
3.2	Ratios of the predictions of the 3P_0 model of meson decay to the experimental values, for the widths of the 28 decays used in the fits. In this figure SHO wavefunctions with effective β 's were used	36
3.3	Ratios of the predictions of the flux-tube breaking model of meson decay to the experimental values, for the widths of the 28 decays used in the fits. In this figure SHO wavefunctions with a common β were used	37
3.4	Ratios of the predictions of the flux-tube breaking model of meson decay to the experimental values, for the widths of the 28 decays used in the fits. In this figure SHO wavefunctions with effective β 's were used	38

3.5	Ratios of the predictions of the flux-tube breaking model of meson decay to the experimental values, for the widths of the 28 decays used in the fits. In this figure RQM wavefunctions were used	39
3.6	Ratios of the predictions of the 3P_0 model of meson decay to the experimental values, for the widths of the 28 decays used in the fits. In this figure SHO wavefunctions with a common β were used, but both β and γ were fit simultaneously	42
3.7	The original data from the discovery of the $f_4(2220)$ by the MARK III Collaboration. The distribution of the K^+K^- invariant mass in $e^+e^- \rightarrow J/\psi \rightarrow \gamma K^+K^-$ is shown, revealing three resonances	44
3.8	Graphs of the $K_1(1270)$ partial decay widths and ratio of D to S amplitudes considered in this work, vs. the mixing angle θ_K	56
3.9	Graphs of the $K_1(1400)$ partial decay widths and ratio of D to S amplitudes considered in this work, vs. the mixing angle θ_K	58
5.1	Graph of the $\gamma\gamma \rightarrow \pi^+\pi^-$ total cross-section vs. \sqrt{s} , for the tree-level scalar QED and BDI predictions, and recent data	71
5.2	The tree-level Feynman diagrams for the scalar QED interaction $\gamma\gamma \rightarrow \pi^+\pi^-$	73
5.3	The geometry of the $\gamma\gamma \rightarrow \pi^+\pi^-$ interaction in the CM frame.	74
5.4	Graph of the $\gamma\gamma \rightarrow \pi^+\pi^-$ tree-level scalar QED cross-sections vs. \sqrt{s}	76
5.5	Example diagrams of the two classes of interactions included in the quark model used to find the effective potentials	77
5.6	Graphs of the $\pi-\pi$ potentials used in this work vs. r	79
5.7	Graphs of the $I = 2$ $\pi-\pi$ scattering phase shift vs. \sqrt{s} , for our predictions, the quark model prediction, and experimental data	87
5.8	Graphs of the $I = 0$ $\pi-\pi$ scattering phase shift vs. \sqrt{s} , for our predictions, the quark model prediction, and experimental data	88

5.9	Graph of the $\gamma\gamma \rightarrow \pi^+\pi^-$ total cross-section vs. \sqrt{s} , for our predictions, the tree-level scalar QED prediction, and experimental data	89
5.10	Graphs of the $\gamma\gamma \rightarrow \pi^0\pi^0$ cross-section vs. \sqrt{s} , for our predictions (cases A, A', B1 and B1') and experimental data	90
5.11	Graphs of the $\gamma\gamma \rightarrow \pi^0\pi^0$ cross-section vs. \sqrt{s} , for our predictions (cases B and B') and experimental data	91

Chapter 1

Introduction

Particle physics is the study of the particles that make up the universe, and the interactions that take place between them. It is also referred to as elementary particle physics, by which we mean that we would ideally like to understand the universe in terms of its “elementary” constituents (should such things exist), that are not composed of other particles.

Why study particle physics? The questions “What is the universe made of?” and “How does it work?” are of fundamental interest for their own sake. In addition, understanding the universe as it is now might help us answer the question “Where did it come from?”

Aside from these weighty questions, what about immediate material benefits? Like much of fundamental research, it is impossible to know now what benefits might be realized from particle physics. However, it is worth noting that in 1897 the quest to understand the universe led to the discovery of the electron by J.J. Thompson. It is safe to say that this early particle physicist could not have predicted the huge effect his work would have on humanity.

1.1 The Standard Model of Particle Physics

We assume that the reader is familiar with modern physics. Familiarity with the field of particle physics would also be useful, but hopefully not necessary; in addition to the introduction to the field that follows, Appendix A contains descriptions of some of the terms and tools of particle physics that may be useful to specialists in other fields.

1.1.1 The Particles that Constitute Matter

At present, the elementary particles that make up matter are thought to be the quarks (six of them, plus their antiparticles) and the leptons (again, six of them, plus antiparticles). We think of them as elementary because, so far, we do not have any indication that they are not. The quarks are the up (u), charm (c) and top (t), all with electric charge $+\frac{2}{3}$ (on a scale where the electron has charge -1), and the down (d), strange (s) and bottom (b), all with charge $-\frac{1}{3}$. The leptons are the electron (e), mu (μ) and tau (τ), all with charge -1 , and the three corresponding neutrinos, ν_e , ν_μ and ν_τ , all with charge 0 . We say corresponding because all these particles are usually thought of as being arranged in doublets,

$$\begin{aligned}
 \text{Quarks :} \quad & \begin{array}{ll} \text{charge } +\frac{2}{3} : & \begin{pmatrix} u \\ d \end{pmatrix}, \begin{pmatrix} c \\ s \end{pmatrix}, \begin{pmatrix} t \\ b \end{pmatrix}, \\ \text{charge } -\frac{1}{3} : & \end{array} \\
 \text{Leptons :} \quad & \begin{array}{ll} \text{charge } 0 : & \begin{pmatrix} \nu_e \\ e \end{pmatrix}, \begin{pmatrix} \nu_\mu \\ \mu \end{pmatrix}, \begin{pmatrix} \nu_\tau \\ \tau \end{pmatrix}. \\ \text{charge } -1 : & \end{array}
 \end{array} \tag{1.1}$$

As one moves to the right in the first, second and fourth rows¹, the particles become more massive. The particles in the third row, the neutrinos, have masses smaller

¹Each column is called a generation; there appear to be only three generations.

Quark	Quark Mass		Lepton	Lepton Mass
	Current	Constituent		
u	2 to 8 MeV	~ 300 MeV	ν_e	< 5.1 eV (95% CL)
c	1.0 to 1.6 GeV	~ 1.5 GeV	ν_μ	< 0.16 MeV (90% CL)
t	180 ± 12 GeV	~ 180 GeV	ν_τ	< 31 MeV (95% CL)
d	5 to 15 MeV	~ 300 MeV	e	$0.51099906(15)$ MeV
s	100 to 300 MeV	~ 500 MeV	μ	$105.658389(34)$ MeV
b	4.1 to 4.5 GeV	~ 5 GeV	τ	$1777.1^{+0.4}_{-0.5}$ MeV

Table 1.1: Masses of the quarks and leptons. The numbers in parentheses denote the 1 standard deviation uncertainty in the end digits of the value. The \pm errors are also 1 standard deviation uncertainties. CL means confidence limit (e.g. we are 95% sure that $m_{\nu_e} < 5.1$ eV).

than the experiments can currently measure, and may be massless. The present experimental values of the masses² are listed in Table 1.1 [1]. Two different masses are listed for the quarks. The current mass is the mass that appears in the Lagrangian describing the strong interaction (see below). The constituent mass is the effective mass the quark has when it is bound inside a hadron (the hadrons are the strongly interacting particles – see below) – the numbers given are approximate because they depend on the hadron model used.

Associated with each type of quark and lepton is its antiparticle, which has the same mass, but opposite quantum numbers (such as charge). Antiparticles are denoted by an overbar (e.g. \bar{u}). Each type of quark or lepton is referred to as a flavour; a particle and its antiparticle have opposite flavour. Each quark and lepton has an intrinsic angular momentum, called spin, of $\frac{1}{2}$, making them fermions (they obey Fermi-Dirac statistics, which hold for particles of half-integral spin).

In addition to their electric charge, each quark has an additional “charge” referred

²Note that the masses in Table 1.1 are given in units of energy (eV), when the units of mass would normally be eV/c^2 . We are following the particle physics convention of setting $c \equiv \hbar \equiv 1$, which expresses mass and momentum in units of energy, and length and time in units of energy $^{-1}$. When converting from these ‘natural units’ to more standard units at the end of a calculation, factors of \hbar and c are inserted as needed to give the required units.

to as colour (but having absolutely nothing to do with the colours of the everyday world). There are three possible values of a colour charge, plus the three anti-colours of the antiquarks. It appears to be a property of nature that coloured objects cannot exist freely by themselves, so quarks are confined inside hadrons in configurations that produce an object with no net colour.

1.1.2 The Interactions

There are four different types of interactions that take place between the particles; to each of them there corresponds one or more gauge bosons (they obey Bose-Einstein statistics, which hold for particles of integral spin), a type of particle that carries the effects of the interaction when it is exchanged between the two particles involved.

The electromagnetic interaction occurs between objects with electric charge, including neutral particles composed of charged constituents (e.g. the neutron interacts via its magnetic moment). It is carried by the photon γ , which is massless and has a spin of 1 (making it a vector particle). As a quantum of electromagnetic radiation, it will be most familiar to the reader as visible light. The theory governing the electromagnetic interaction is called Quantum Electrodynamics (QED).

The weak interaction occurs between leptons and quarks, and involves the interacting particles being transformed into their partners in the doublets of particles shown in (1.1).³ It is carried by the Z^0 and W^\pm bosons (spin 1) with the charges shown and masses of 91.187 ± 0.007 GeV and 80.33 ± 0.15 GeV, respectively. Because the weak interaction deals with the flavour of the involved particles, the theory that describes it is sometimes called Quantum Flavourdynamics. The theories of the electromagnetic and weak interactions have been combined into a single theory, called

³For the quarks at least this is a simplification: while the quarks prefer to be transformed into their partners, they may also be transformed into one of the other two quarks in the same row as their partners. It is not clear if the leptons also have this type of cross-generational mixing.

the Electroweak Theory. The weak interaction is the cause of certain decays, such as the decay of the neutron $n \rightarrow p e^- \bar{\nu}_e$.

The strong interaction occurs between coloured objects, including colourless particles composed of coloured constituents. It is carried by eight gluons g , which have spin 1, no mass and no charge. However, they themselves have colour, which complicates the theory of the strong interaction, Quantum Chromodynamics (QCD). The strong interaction binds the quarks together to form hadrons, including the nucleons. The residual strong forces between the colourless nucleons bind the nucleus together.

The particles and interactions discussed above, and a spontaneous symmetry breaking mechanism (called the Higgs mechanism) that gives the fermions their masses make up what is called the Standard Model of Particle Physics. The Higgs mechanism gives rise to the Higgs boson, a massive (> 58.4 GeV, 95% CL), neutral scalar (spin 0) particle, which has not yet been seen.

The remaining interaction, gravity, is well described by a classical theory, General Relativity, but so far no way has been found to incorporate it into a quantum field theory (such as the electroweak theory or QCD). That has not prevented physicists from naming its hypothetical carrier the graviton – it would be massless, neutral, and have spin 2.

One drawback of the standard model is that it has 19 (23 if the neutrinos have mass) parameters that must be fitted to the data (e.g. the 12 quark and lepton masses). This doesn't mean that the theory is wrong, but suggests that there is probably a more complete theory out there. The electroweak theory has been extremely successful; despite extensive experimental programs designed to test it, no statistically significant deviations from it have been found.

Calculations in the electroweak theory are carried out perturbatively, in powers of the fine structure constant $\alpha = 1/(137.0359895 \pm 0.0000061)$ for a momentum transfer of zero (at higher momentum transfers α increases somewhat; at the Z mass

it is approximately $1/128$). Because α is small, the perturbation theory converges reasonably well. However, for QCD, the situation is rather different. Because the gluons carry a colour charge, they can interact among themselves, leading to a coupling constant α_s that *decreases* for larger momentum transfer, and increases as the momentum transfer goes towards zero. This behaviour at large momentum transfer is known as asymptotic freedom, and means that perturbative QCD is valid for high momentum transfers, but breaks down at the lower momentum transfers where the coupling becomes strong.

Unfortunately, the strong interactions found in the everyday world (the binding of quarks into nucleons, and of these into atomic nuclei) occur at low energies (and hence low momentum transfers). At present, lattice methods are the only rigorous way to do non-perturbative calculations with QCD. However, while great progress has been made using these techniques, it is not yet clear how long it will be until reliable results can be obtained, especially for complicated problems such as the calculation of decay widths of excited states.

1.2 The Hadrons

The six quarks and six leptons (plus their antiparticles) may make up matter, but only three of them make up the everyday matter around us. All of the matter in our everyday world is made up of atoms. An atom consists of a dense core, the nucleus, surrounded by a cloud of electrons. The structure of the electron cloud is responsible for the chemical properties of the atom.

The nucleus is made up of a number of nucleons (protons (charge +1) and, usually, neutrons (charge 0)) bound together by the strong interaction. The atomic number of the atom is given by the number of protons; a neutral atom also has the same number of electrons. The number of neutrons is very approximately equal to the number of

protons. Both protons and neutrons are made up of three light quarks: the proton from two u 's and a d , and the neutron from a u and two d 's. (Note how the charges of the quarks add to give the correct nucleon charges.) Everyday matter is made up of these three constituents (e^- , u and d) because being the lightest members of their rows in (1.1), they are stable against decay⁴; neutrinos are also common, but because they only interact via the weak interaction they interact with everyday matter very rarely, and we are not aware of them.

Protons and neutrons are examples of baryons, one of the two known types of structures which quarks can form. Baryons are made up of three quarks (qqq); an anti-baryon would be made up of three antiquarks. The other known type of structure is the meson, which is made up of a quark and an antiquark, $q\bar{q}$ (so an anti-meson is just a meson). The complicated structure of QCD means that groups of quarks can be bound together only for certain configurations which can have no net colour (so they are in a colour singlet state). It also means that the attractive force between coloured objects is huge, so they are always confined together into colourless objects. This property is called confinement.

In a baryon each quark is a different colour, and the three colours mixed together produce a colourless object. In a meson the quark has a colour and the antiquark has the corresponding anti-colour to cancel it, again producing a colourless object. It may also be possible to have bound $qqqqqq$ or $q\bar{q}q\bar{q}$ states, etc., but no observed states have been firmly identified as such. Even more interesting would be glueballs (states consisting only of gluons) or hybrids (states consisting of both quarks and gluons – see below). Once again, no observed states have been firmly identified with these structures. These strongly-interacting states built up of quarks and gluons are collectively called hadrons.

⁴Actually, a u quark can decay into a d via the weak interaction, and vice versa. However, a u or d always remains, so taken together they are stable.

In order to explain glueballs and hybrids, it helps to introduce the flux-tube picture of QCD. At higher energies, where perturbative QCD is valid, the picture of a gluon as a discrete particle exchanged by quarks is appropriate. However, at lower energies where the coupling becomes stronger there are indications that a more appropriate picture is that of tubes of chromoelectric flux connecting the quarks [2]. These could be thought of as being similar to the lines of an electric field connecting electrically charged objects, but because of the self-interacting nature of the gluons the lines collapse down to a tube. This picture incorporates confinement – if the flux tubes have a certain energy per unit length, then as the quarks get further apart the energy of the tube would go up linearly, making it impossible to separate the quarks.

A meson or baryon is specified by the flavours of the quarks, the space wavefunction of the quarks, and the wavefunction describing how the quark spins combine. Much like a hydrogen atom, the space wavefunction can have angular and/or radial excitations which are identified as different meson or baryon states. It has been theorized (see for example Reference [3]) that the flux-tube can also be excited, either vibrationally (like a vibrating string) or topologically (more complicated topologies of the flux-tube than just a single line). The resulting particles would be meson and baryon hybrids. The glueball can also be thought of in this picture as a flux-tube connected into a loop, with no quarks present.

The experimental identification of hadrons other than baryons and mesons would be an important confirmation of our understanding of QCD.

1.2.1 The Mesons

As mentioned above, a meson is specified by its flavour, and its spin and space wavefunctions. The flavour wavefunctions that we will deal with in this work are given in Appendix B.2. The spin wavefunction is particularly simple: the two spins of $\frac{1}{2}$ can add to give $S = 0$ (a singlet) or $S = 1$ (a triplet); for more details see

Appendix D.3. Like the space wavefunction of the hydrogen atom, meson space wavefunctions also have a radial quantum number n and a quantum number for orbital angular momentum, L (but unlike the hydrogen atom, n and L are independent). The total angular momentum is given by $\vec{J} = \vec{L} + \vec{S}$. The space and spin state of a meson is often specified by spectroscopic notation, $n^{2S+1}L_J$, where the $2S + 1$ is 1 or 3 for the singlet or triplet, respectively, and L is given by a letter (S, P, D, F, G, H,... being 0, 1, 2, 3, 4, 5,...). If $n = 1$ it will often be neglected in the notation. It is also useful to give the parity and charge conjugation⁵ (where applicable) quantum numbers of the state – these are usually expressed with J as J^{PC} .

In Table 1.2 we list the known mesons constructed of the light u , d and s quarks (which are all that we will be concerned with in this thesis) according to the Particle Data Group [1]. The rows have different space and spin states and the columns represent different flavours. For the $I = 1$ and $I = \frac{1}{2}$ column headings the quark states listed are considered to be different charge states of the same meson (and the antiparticles), because of the isospin symmetry between the u and d quarks. For the $I = 0$ column the two mesons in each row are listed together because the proportion of $\frac{1}{\sqrt{2}}(u\bar{u} + d\bar{d})$ and $s\bar{s}$ states in each is not the same for all of the rows. The C assignment in J^{PC} only refers to the neutral members of the row. The names of the mesons are related to their flavours, the optional subscript after the name gives J , and the optional number in parentheses after the name is the mass of the meson in MeV.

1.2.2 The Quark Model

Because perturbative QCD does not work at low energies, and non-perturbative calculations have yet to produce detailed results, we try to calculate the properties of

⁵Parity, charge conjugation, and other conservation laws and invariance principles are discussed briefly in Appendix A.4.

$n^{2S+1}L_J$	$J^P\mathcal{C}$	$I = 1$ ($-u\bar{d}$, $\frac{1}{\sqrt{2}}(u\bar{u}-d\bar{d})$, $d\bar{u}$)	$I = 0$ ($\frac{1}{\sqrt{2}}(u\bar{u}+d\bar{d})$, $s\bar{s}$)	$I = \frac{1}{2}$ ($-u\bar{s}$, $-d\bar{s}$, $-s\bar{d}$, $s\bar{u}$)
1^1S_0	0^{-+}	π	η, η'	K
1^3S_1	1^{--}	ρ	ω, ϕ	$K^*(892)$
1^1P_1	1^{+-}	$b_1(1235)$	$h_1(1170), h_1(1380)^\heartsuit$	$K_1(1270), K_1(1400)^\dagger$
1^3P_0	0^{++}	$a_0(980)$	$f_0(1300), f_0(980)$	$K_0^*(1430)$
1^3P_1	1^{++}	$a_1(1260)$	$f_1(1285), f_1(1510)$	$K_1(1270), K_1(1400)^\dagger$
1^3P_2	2^{++}	$a_2(1320)$	$f_2(1270), f_2'(1525)$	$K_2^*(1430)$
1^1D_2	2^{-+}	$\pi_2(1670)$,	$K_2(1770)$
1^3D_1	1^{--}	$\rho(1700)$	$\omega(1600),$	$K^*(1680)^\ddagger$
1^3D_2	2^{--}		,	$K_2(1820)$
1^3D_3	3^{--}	$\rho_3(1690)$	$\omega_3(1670), \phi_3(1850)$	$K_3^*(1780)$
1^3F_4	4^{++}	$a_4(2040)^\heartsuit$	$f_4(2050), f_4(2220)^\heartsuit$	$K_4^*(2045)$
2^1S_0	0^{-+}	$\pi(1300)$	$\eta(1295),$	$K(1460)^\heartsuit$
2^3S_1	1^{--}	$\rho(1450)$	$\omega(1420), \phi(1680)$	$K^*(1410)^\ddagger$
2^3P_2	2^{++}		$f_2(1810)^\heartsuit, f_2(2010)$	$K_2^*(1980)^\heartsuit$
3^1S_0	0^{-+}	$\pi(1770)^\heartsuit$	$\eta(1760)^\heartsuit,$	$K(1830)^\heartsuit$

Table 1.2: The meson spectrum for the light quarks. This table is mostly taken from the Review of Particle Properties [1] by the Particle Data Group.

◊ These states are not included in the Meson Summary Table of the Review of Particle Properties.

† The Particle Data Group believes that the 1^1P_1 and 1^3P_1 strange mesons are nearly equal (45°) mixtures of the $K_1(1270)$ and $K_1(1400)$. See Section 3.3 and Appendix A.7.

‡ The Particle Data Group notes that the $K^*(1410)$ could be replaced by the $K^*(1680)$ as the 2^3S_1 strange meson.

hadrons using models inspired by QCD rather than the full theory itself. The quark model⁶ is one such attempt, and a very successful one.

In a quark model of a meson, the wavefunction describing the relative motion of the quark and antiquark is obtained by solving the Schrödinger equation with a Hamiltonian inspired by QCD. As an example of such a model, consider that of Godfrey and Isgur [4]. Their effective potential, $V_{q\bar{q}}(\vec{p}, \vec{r})$, contains the effects of

⁶In this thesis, when we refer to the quark model, we mean the constituent quark model in particular.

a Lorentz-vector one-gluon-exchange interaction at short distances and a Lorentz-scalar linear interaction that models confinement. $V_{q\bar{q}}(\vec{p}, \vec{r})$ was found by equating the scattering amplitude of free quarks, using a scattering kernel with the desired Dirac structure, with the effects of the effective potential. Because of relativistic effects the potential is momentum dependent in addition to being coordinate dependent. To first order in $(v/c)^2$, $V_{q\bar{q}}(\vec{p}, \vec{r})$ reduces to the standard nonrelativistic result:

$$V_{q\bar{q}}(\vec{p}, \vec{r}) \rightarrow V(\vec{r}) = H_{q\bar{q}}^{\text{conf}} + H_{q\bar{q}}^{\text{cont}} + H_{q\bar{q}}^{\text{ten}} + H_{q\bar{q}}^{\text{SO}}, \quad (1.2)$$

where

$$H_{q\bar{q}}^{\text{conf}} = C + br + \frac{\alpha_s(r)}{r} \vec{F}_q \cdot \vec{F}_{\bar{q}} \quad (1.3)$$

includes the spin-independent linear confinement term and Coulomb-like (from one-gluon-exchange) interaction,

$$H_{q\bar{q}}^{\text{cont}} = -\frac{8\pi}{3} \frac{\alpha_s(r)}{m_q m_{\bar{q}}} \vec{S}_q \cdot \vec{S}_{\bar{q}} \delta^3(\vec{r}) \vec{F}_q \cdot \vec{F}_{\bar{q}} \quad (1.4)$$

is the contact part of the colour-hyperfine interaction,

$$H_{q\bar{q}}^{\text{ten}} = -\frac{\alpha_s(r)}{m_q m_{\bar{q}}} \frac{1}{r^3} \left[\frac{3\vec{S}_q \cdot \vec{r} \vec{S}_{\bar{q}} \cdot \vec{r}}{r^2} - \vec{S}_q \cdot \vec{S}_{\bar{q}} \right] \vec{F}_q \cdot \vec{F}_{\bar{q}} \quad (1.5)$$

is the tensor part of the colour-hyperfine interaction, and

$$H_{q\bar{q}}^{\text{SO}} = H_{q\bar{q}}^{\text{SO(CM)}} + H_{q\bar{q}}^{\text{SO(TP)}} \quad (1.6)$$

is the spin-orbit interaction with

$$H_{q\bar{q}}^{\text{SO(CM)}} = -\frac{\alpha_s(r)}{r^3} \left(\frac{\vec{S}_q}{m_q m_{\bar{q}}} + \frac{\vec{S}_{\bar{q}}}{m_q m_{\bar{q}}} + \frac{\vec{S}_q}{m_q^2} + \frac{\vec{S}_{\bar{q}}}{m_{\bar{q}}^2} \right) \cdot \vec{L} \vec{F}_q \cdot \vec{F}_{\bar{q}} \quad (1.7)$$

its colour magnetic piece arising from one-gluon-exchange and

$$H_{q\bar{q}}^{\text{SO(TP)}} = -\frac{1}{2r} \frac{\partial H_{q\bar{q}}^{\text{conf}}}{\partial r} \left(\frac{\vec{S}_q}{m_q^2} + \frac{\vec{S}_{\bar{q}}}{m_{\bar{q}}^2} \right) \cdot \vec{L} \quad (1.8)$$

the Thomas precession term. In these formulae, m_q ($m_{\bar{q}}$) and \vec{S}_q ($\vec{S}_{\bar{q}}$) are the mass and spin of the quark (antiquark), L is the orbital angular momentum between the quark and antiquark, $\alpha_s(r)$ is the running coupling constant of QCD, and the \vec{F} 's are related to the Gell-Mann λ -matrices and have expectation value $\langle \vec{F}_q \cdot \vec{F}_{\bar{q}} \rangle = -4/3$ for a meson.

Godfrey and Isgur's model is actually a *relativized* quark model, as opposed to a nonrelativistic quark model. They include relativistic effects by replacing the kinetic energy term $m_q + m_{\bar{q}} + \frac{p^2}{2m_q} + \frac{p^2}{2m_{\bar{q}}}$ in the Hamiltonian by the relativistic term $\sqrt{p^2 + m_q^2} + \sqrt{p^2 + m_{\bar{q}}^2}$ (p is the relative momentum⁷ in the CM frame), by keeping m/E factors, and by applying relativistic smearing to the potentials. They also include the effects of annihilation interactions via gluons for the isoscalar mesons.

The quark model has been highly successful at mapping the meson spectrum. Associated models of meson decay have also been quite successful at predicting the decays [4, 5].

1.3 The Work of this Thesis

We mentioned above that perturbative QCD does not work at low energies, and that non-perturbative calculations have yet to produce detailed results. (In fact, the problem arises with any strongly-interacting field theory.) Until we can make quantitative predictions of hadronic properties using QCD, we cannot say that we understand the theory, nor can we make significant headway in this important regime.

⁷See Appendix A.5 for the definitions of relative and CM coordinates.

In order to provide some quantitative predictions for the low-energy regime, an industry has sprung up that calculates hadron properties by using models inspired by QCD, rather than the full theory itself. There are three purposes of such a program. The first is to shed light on the dynamics of the model, and hence (hopefully) on QCD, by determining which facets of the model are important in predicting results that agree with experiment. The second is to understand the properties of the hadrons themselves. The third is to use these calculated properties to map the hadron spectrum. If we understand the meson and baryon spectra well, and there are extra states that do not fit into them, then these states must be something new (hybrids, glueballs, etc.)! Confirmation of these extra states would then feed back to the first purpose, understanding the dynamics of QCD.

This thesis deals with properties of mesons calculated in the quark model, which is one of these attempts to approximate QCD. The meson spectrum, with its large number of states to be studied, provides an excellent testing ground for our understanding of QCD. We examine two general areas in the quark model: models of meson decay, and final state interactions.

In the first area the properties we calculate are the decay widths⁸ for the strong decays of mesons. Because meson resonances are studied experimentally by examining the particles to which they decay, decay widths are vital in their identification. As an example of this we study the identity of the $f_4(2220)$ state – although tentatively identified as the 3F_4 $s\bar{s}$ meson by the Particle Data Group (see Table 1.2), its identity has been uncertain since its discovery in 1983. We also investigate the mixing⁹ between the $K_1(1270)$ and $K_1(1400)$ mesons, in order to see if the dynamics of the model are responsible for the mixing, or whether it occurs via a separate mechanism that has not yet been included. This is done by comparing the models' predictions

⁸See Appendix A.1 for an introduction to decay widths, resonances and cross-sections.

⁹See Appendix A.7 for an introduction to mixing.

for the decay widths of these mesons to experimental data. These works have already been published [6, 7].

In the second area we investigate the effects of the final state interactions in the reaction $\gamma\gamma \rightarrow \pi\pi$. This is again an attempt to understand the quark model dynamics responsible for the interaction. In addition, if we understand the situation in $\gamma\gamma \rightarrow$ two pseudoscalar¹⁰ mesons, we can then approach the situation in $\gamma\gamma \rightarrow$ two vector mesons with more confidence; the structures seen in the cross-sections of these processes are not well understood and are a long-standing puzzle.

In Chapter 2 we describe in detail the models of meson decay we are interested in, and the means by which we applied them. In Chapter 3 we fit the free parameter of the models, and investigate a number of choices that must be made in their application. We then apply the models to the first two chosen problems. In Chapter 4 we describe in detail the techniques we use for calculating the effects of final state interactions. In Chapter 5 we apply the techniques to our third chosen problem. In Chapter 6 we conclude.

¹⁰A pseudoscalar particle has $J^P = 0^-$, as opposed to a scalar which has $J^P = 0^+$.

Chapter 2

Two Models of Meson Decay

2.1 The 3P_0 Model of Meson Decay

The 3P_0 model [8, 9], also known as the Quark-Pair Creation (QPC) model, is applicable to OZI-allowed¹ strong decays of a meson into two other mesons, which are expected to be the dominant decay modes of a meson if they are allowed. It can also be used to describe two-body OZI-allowed strong decays of other hadrons.

In this model, meson decay occurs when a quark-antiquark pair (labelled 3 and 4) is produced from the vacuum in a state suitable for quark rearrangement to occur, as in Figure 2.1. The created pair will have the quantum numbers of the vacuum, $J^{PC} = 0^{++}$, suggesting that they are in a 3P_0 state. There is one undetermined parameter γ in the model – it represents the probability that a quark-antiquark pair will be created from the vacuum. The pair is assumed to be created in an SU(N) flavour singlet, where the number of flavours N is arbitrary, since changing it will just rescale the value of γ needed (see Appendix D.2). The rest of the model is just the description of the overlap of the initial meson (A) and the created pair (sometimes

¹See Appendix A.6 for an explanation of the OZI rule.

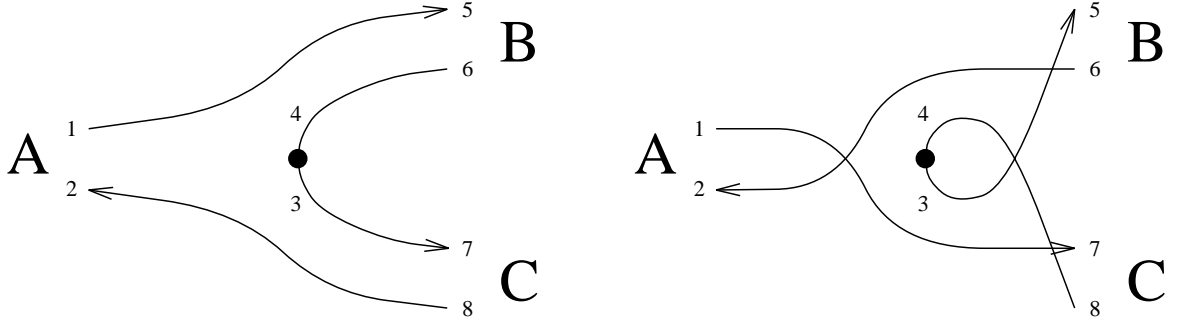


Figure 2.1: The two possible diagrams contributing to the meson decay $A \rightarrow BC$ in the 3P_0 model. In many cases only one of these diagrams will contribute.

referred to by 0) with the two final mesons (B, C), to calculate the probability that rearrangement (and hence decay) will occur.

For the meson wavefunction we use a mock meson defined by [10]

$$\begin{aligned}
 |A(n_A {}^{2S_A+1} L_A J_A M_{J_A})(\vec{P}_A)\rangle &\equiv \sqrt{2E_A} \sum_{M_{L_A}, M_{S_A}} \langle L_A M_{L_A} S_A M_{S_A} | J_A M_{J_A} \rangle \\
 &\times \int d^3 \vec{p}_A \psi_{n_A L_A M_{L_A}}(\vec{p}_A) \chi_{S_A M_{S_A}}^{12} \phi_A^{12} \omega_A^{12} \\
 &\times |q_1(\frac{m_1}{m_1+m_2} \vec{P}_A + \vec{p}_A) \bar{q}_2(\frac{m_2}{m_1+m_2} \vec{P}_A - \vec{p}_A)\rangle. \quad (2.1)
 \end{aligned}$$

Note that given our field-theory conventions of Appendix C, the mock meson is normalized relativistically to

$$\langle A(n_A {}^{2S_A+1} L_A J_A M_{J_A})(\vec{P}) | A(n_A {}^{2S_A+1} L_A J_A M_{J_A})(\vec{P}') \rangle = 2E_A \delta^3(\vec{P} - \vec{P}'), \quad (2.2)$$

but uses nonrelativistic spinors and CM coordinates. The meson has CM momentum \vec{P}_A , and the relative momentum of the $q\bar{q}$ pair \vec{p}_A is integrated over all values. The other quantities are as follows: n_A is the radial quantum number; $|L_A, M_{L_A}\rangle$, $|S_A, M_{S_A}\rangle$ and $|J_A, M_{J_A}\rangle$ are the quantum numbers of the orbital angular momentum between the two quarks, the total spin of the two quarks, and the total angular momentum of the meson, respectively; $\langle L_A M_{L_A} S_A M_{S_A} | J_A M_{J_A} \rangle$ is a Clebsch-Gordan

coefficient²; E_A is the total energy of the meson; $\chi_{S_A M_{S_A}}^{12}$, ϕ_A^{12} and ω_A^{12} are the appropriate factors for combining the quark spins to obtain $|S_A, M_{S_A}\rangle$, the flavours to obtain the correct meson flavour, and the colours to obtain a colour singlet, respectively; $\psi_{n_A L_A M_{L_A}}(\vec{p}_A)$ is the relative wavefunction of the quarks in momentum-space; m_1 and m_2 are the masses of the quark and antiquark respectively; and finally, $|q_1(\vec{p}_1) \bar{q}_2(\vec{p}_2)\rangle$ is the basic state of a free quark and antiquark.

Now we can consider the decay $A \rightarrow BC$. Define the S matrix

$$S \equiv I - 2\pi i \delta(E_f - E_i) T \quad (2.3)$$

and then

$$\langle f | T | i \rangle \equiv \delta^3(\vec{P}_f - \vec{P}_i) M^{M_{J_A} M_{J_B} M_{J_C}} \quad (2.4)$$

which gives, using relativistic phase space³ and a meson wavefunction normalized as in Eq. 2.2, the decay width in the CM frame

$$\Gamma = \pi^2 \frac{P}{M_A^2} \frac{\mathcal{S}}{(2J_A + 1)} \sum_{M_{J_A}, M_{J_B}, M_{J_C}} |M^{M_{J_A} M_{J_B} M_{J_C}}|^2. \quad (2.5)$$

Here P is the magnitude of the momentum of either outgoing meson, M_A is the mass of meson A , $\mathcal{S} \equiv 1/(1 + \delta_{BC})$ is a statistical factor that is needed if B and C are identical particles, and $M^{M_{J_A} M_{J_B} M_{J_C}}$ is the decay amplitude.

For the transition operator we use

$$T = -3\gamma \sum_m \langle 1m 1-m | 00 \rangle \int d^3\vec{p}_3 d^3\vec{p}_4 \delta^3(\vec{p}_3 + \vec{p}_4) \mathcal{Y}_1^m(\frac{\vec{p}_3 - \vec{p}_4}{2}) \chi_{1-m}^{34} \phi_0^{34} \omega_0^{34} b_3^\dagger(p_3) d_4^\dagger(p_4). \quad (2.6)$$

Here the momenta of both the created quark (3) and antiquark (4) are integrated over

²See Appendix A.3 for an explanation of Clebsch-Gordan coefficients and Wigner nj symbols.

³Note that we have used relativistic phase space (leading to Eq. 2.5) and a relativistic normalization (Eq. 2.2). We will also consider other choices of phase space/normalization in Section 3.1.

all values, with the constraint that their total momentum is zero. Other quantities are as follows: γ is the one undetermined parameter in the model⁴; $b_3^\dagger(p_3)$ and $d_4^\dagger(p_4)$ are the creation operators of the created quark and antiquark, respectively; $\mathcal{Y}_l^m(\vec{p}) \equiv p^l Y_l^m(\theta_p, \phi_p)$ is a solid harmonic that gives the momentum-space distribution of the created pair⁵; and the other quantities are as in Eq. 2.1. Here the spins and relative orbital angular momentum of the created quark and antiquark are combined in a 3P_0 state to give the pair the overall $J^P = 0^{++}$ quantum numbers.

Combining Eqs. 2.1, 2.4 and 2.6 gives for the amplitude in the CM frame (after doing the colour wavefunction overlap, and transforming one of the spin wavefunction overlaps – see Appendix D):

$$\begin{aligned}
 M^{M_{J_A} M_{J_B} M_{J_C}}(\vec{P}) = & \gamma \sqrt{8E_A E_B E_C} \sum_{\substack{M_{L_A}, M_{S_A}, M_{L_B}, M_{S_B}, \\ M_{L_C}, M_{S_C}, m}} \langle L_A M_{L_A} S_A M_{S_A} | J_A M_{J_A} \rangle \\
 & \times \langle L_B M_{L_B} S_B M_{S_B} | J_B M_{J_B} \rangle \langle L_C M_{L_C} S_C M_{S_C} | J_C M_{J_C} \rangle \\
 & \times \langle 1m 1-m | 00 \rangle \langle \chi_{S_B M_{S_B}}^{14} \chi_{S_C M_{S_C}}^{32} | \chi_{S_A M_{S_A}}^{12} \chi_{1-m}^{34} \rangle \\
 & \times \left[\langle \phi_B^{14} \phi_C^{32} | \phi_A^{12} \phi_0^{34} \rangle I(\vec{P}, m_1, m_2, m_3) \right. \\
 & \left. + (-1)^{1+S_A+S_B+S_C} \langle \phi_B^{32} \phi_C^{14} | \phi_A^{12} \phi_0^{34} \rangle I(-\vec{P}, m_2, m_1, m_3) \right]. \tag{2.7}
 \end{aligned}$$

The two terms in the last factor correspond to the two possible diagrams in Figure 2.1 – in the first diagram the quark in A ends up B ; in the second it ends up in C . The superscripts within the spin and flavour wavefunction overlaps serve to identify the (anti)quarks on the left side with the corresponding (anti)quarks on the right side.

⁴Our value of γ is higher than that used by Kokoski and Isgur [5] by a factor of $\sqrt{96\pi}$ due to different field theory conventions, constant factors in T , etc. The calculated values of the widths are, of course, unaffected.

⁵The presence of the solid harmonic can be demonstrated by examining the matrix element for the creation of a quark-antiquark pair from the vacuum with the scalar operator constructed from the field: $\langle q(p_q) \bar{q}(p_{\bar{q}}) | \Psi(x') \bar{\Psi}(x'') | 0 \rangle$. The solid harmonic and the Clebsch-Gordan coefficient can both be extracted from the spinor portion of the result.

The momentum space integral $I(\vec{P}, m_1, m_2, m_3)$ is given by

$$I(\vec{P}, m_1, m_2, m_3) = \int d^3 \vec{p} \psi_{n_B L_B M_{L_B}}^*(\frac{m_3}{m_1+m_3} \vec{P} + \vec{p}) \psi_{n_C L_C M_{L_C}}^*(\frac{m_3}{m_2+m_3} \vec{P} + \vec{p}) \times \psi_{n_A L_A M_{L_A}}(\vec{P} + \vec{p}) \mathcal{Y}_1^m(\vec{p}) \quad (2.8)$$

where we have taken $\vec{P} \equiv \vec{P}_B = -\vec{P}_C$.

2.2 Calculating Meson Decay Widths with the 3P_0 Model

In order to calculate the decay amplitudes of the 3P_0 model, we use the techniques of Roberts and Silvestre-Brac [9]. These techniques require that the radial portions of the meson space wavefunctions be expressible in certain functional forms, which encompass simple harmonic oscillator (SHO) wavefunctions. In what follows, we assume that the radial portions of the wavefunctions are expressed as linear combinations of the first $N + 1$ SHO radial wavefunctions (see Appendix B.1),

$$R_{L_A}(p_A) = \sum_{a=0}^N d_a^A R_{n_A=a, L_A}^{\text{SHO}}(p_A). \quad (2.9)$$

The β_A , etc. found below are the oscillator parameters of the wavefunctions.

The decay amplitudes of Eq. 2.7 are converted to partial wave amplitudes by means of a recoupling calculation (see Appendix E). Then the whole expression for the amplitudes, including the integrals of Eqs. 2.8 and E.4, is converted into a sum over angular momentum quantum numbers. The graphical methods for manipulating angular momentum expressions found in Zare [11] were particularly useful in this

regard. Our result, very similar to that of Roberts and Silvestre-Brac, is

$$\begin{aligned}
M^{SL}(P) = & \gamma \sqrt{\frac{8E_A E_B E_C}{3}} (-i)^{L_A + L_B + L_C} (-1)^{1 + S_B + S + J_B + J_C} \\
& \times \sum_{S'} (-1)^{S'} \begin{bmatrix} \frac{1}{2} & \frac{1}{2} & S_A \\ \frac{1}{2} & \frac{1}{2} & 1 \\ S_B & S_C & S' \end{bmatrix} \sum_{L'} \begin{bmatrix} S_B & L_B & J_B \\ S_C & L_C & J_C \\ S' & L' & S \end{bmatrix} \sum_{L''} \widehat{L''} \begin{Bmatrix} S_A & L_A & J_A \\ L'' & S' & 1 \end{Bmatrix} \\
& \times \begin{Bmatrix} S' & L' & S \\ L & J_A & L'' \end{Bmatrix} [\langle \phi_B^{14} \phi_C^{32} | \phi_A^{12} \phi_0^{34} \rangle \varepsilon(L_A, L_B, L_C, L, L', L'', P, m_1, m_2, m_3) + \\
& (-1)^{1 + S_A + S_B + S_C + L} \langle \phi_B^{32} \phi_C^{14} | \phi_A^{12} \phi_0^{34} \rangle \varepsilon(L_A, L_B, L_C, L, L', L'', P, m_2, m_1, m_3)] \tag{2.10}
\end{aligned}$$

where the modified $9j$ symbol is defined in terms of the $9j$ symbol

$$\begin{bmatrix} j_1 & j_2 & J_{12} \\ j_3 & j_4 & J_{34} \\ J_{13} & J_{24} & J \end{bmatrix} \equiv \widehat{J_{12}} \widehat{J_{34}} \widehat{J_{13}} \widehat{J_{24}} \widehat{J} \begin{Bmatrix} j_1 & j_2 & J_{12} \\ j_3 & j_4 & J_{34} \\ J_{13} & J_{24} & J \end{Bmatrix}, \tag{2.11}$$

and where $\widehat{J} \equiv \sqrt{2J + 1}$,

$$\begin{aligned}
\varepsilon(L_A, L_B, L_C, L, L', L'', P, m_1, m_2, m_3) \equiv & \frac{1}{2\beta_A^{L_A+\frac{3}{2}} \beta_B^{L_B+\frac{3}{2}} \beta_C^{L_C+\frac{3}{2}}} \frac{e^{-F^2 P^2}}{G^{L_A + L_B + L_C + 4}} \\
& \times \sum_{l_1, l_2, l_3, l_4} C_{l_1}^{L_B} C_{l_2}^{L_C} C_{l_3}^1 C_{l_4}^{L_A} \left(x - \frac{m_1}{m_1 + m_3} \right)^{l_1} \left(x - \frac{m_2}{m_2 + m_3} \right)^{l_2} (x - 1)^{l_3} x^{l_4} \\
& \times \sum_{l_{12}, l_5, l_6, l_7, l_8} (-1)^{l_{12} + l_6} \widehat{l_5} \begin{bmatrix} l_1 & l'_1 & L_B \\ l_2 & l'_2 & L_C \\ l_{12} & l_6 & L' \end{bmatrix} \begin{bmatrix} l_3 & l'_3 & 1 \\ l_4 & l'_4 & L_A \\ l_7 & l_8 & L'' \end{bmatrix} \begin{Bmatrix} L & l_{12} & l_5 \\ l_6 & L'' & L' \end{Bmatrix} \\
& \times B_{l_1 l_2}^{l_{12}} B_{L l_{12}}^{l_5} B_{l'_1 l'_2}^{l_6} B_{l_3 l_4}^{l_7} B_{l'_3 l'_4}^{l_8} \sum_{\lambda, \mu, \nu} D_{\lambda \mu \nu} I_{\nu}(l_5, l_6, l_7, l_8, L'') \frac{P^{l_1 + l_2 + l_3 + l_4 + 2\lambda + \nu}}{G^{2\mu + \nu - l_1 - l_2 - l_3 - l_4}}
\end{aligned}$$

$$\times \left(\frac{l'_1 + l'_2 + l'_3 + l'_4 + 2\mu + \nu + 1}{2} \right)!, \quad (2.12)$$

$$F^2 \equiv \frac{1}{2} \left[\frac{x^2}{\beta_A^2} + \frac{\left(x - \frac{m_1}{m_1+m_3} \right)^2}{\beta_B^2} + \frac{\left(x - \frac{m_2}{m_2+m_3} \right)^2}{\beta_C^2} \right], \quad (2.13)$$

$$G^2 \equiv \frac{1}{2} \left[\frac{1}{\beta_A^2} + \frac{1}{\beta_B^2} + \frac{1}{\beta_C^2} \right], \quad (2.14)$$

$$x \equiv \frac{\left(\frac{m_1}{m_1+m_3} \beta_C^2 + \frac{m_2}{m_2+m_3} \beta_B^2 \right) \beta_A^2}{\beta_A^2 \beta_B^2 + \beta_A^2 \beta_C^2 + \beta_B^2 \beta_C^2}, \quad (2.15)$$

$$C_{l_1}^l \equiv \sqrt{\frac{4\pi(2l+1)!}{(2l_1+1)![2(l-l_1)+1]!}}, \quad (2.16)$$

$$B_{l_1 l_2}^l \equiv \frac{(-1)^l}{\sqrt{4\pi}} \hat{l}_1 \hat{l}_2 \begin{pmatrix} l_1 & l_2 & l \\ 0 & 0 & 0 \end{pmatrix}, \quad (2.17)$$

$$I_{2p}(l_5, l_6, l_7, l_8, L'') \equiv (-1)^{L''}(2p)! \hat{l}_5 \hat{l}_6 \hat{l}_7 \hat{l}_8 \sum_{\sigma=0}^p \frac{4^\sigma (4\sigma+1)(p+\sigma)!}{(2p+2\sigma+1)!(p-\sigma)!} \times \begin{pmatrix} 2\sigma & l_5 & l_7 \\ 0 & 0 & 0 \end{pmatrix} \begin{pmatrix} 2\sigma & l_6 & l_8 \\ 0 & 0 & 0 \end{pmatrix} \left\{ \begin{array}{c} l_5 \quad l_6 \quad L'' \\ l_8 \quad l_7 \quad 2\sigma \end{array} \right\}, \quad (2.18)$$

$$I_{2p+1}(l_5, l_6, l_7, l_8, L'') \equiv 2(-1)^{L''+1}(2p+1)! \hat{l}_5 \hat{l}_6 \hat{l}_7 \hat{l}_8 \sum_{\sigma=0}^p \frac{4^\sigma (4\sigma+3)(p+\sigma+1)!}{(2p+2\sigma+3)!(p-\sigma)!} \times \begin{pmatrix} 2\sigma+1 & l_5 & l_7 \\ 0 & 0 & 0 \end{pmatrix} \begin{pmatrix} 2\sigma+1 & l_6 & l_8 \\ 0 & 0 & 0 \end{pmatrix} \left\{ \begin{array}{c} l_5 \quad l_6 \quad L'' \\ l_8 \quad l_7 \quad 2\sigma+1 \end{array} \right\}, \quad (2.19)$$

where $l'_1 \equiv L_B - l_1$, $l'_2 \equiv L_C - l_2$, $l'_3 \equiv 1 - l_3$, $l'_4 \equiv L_A - l_4$ and $D_{\lambda\mu\nu}$ can be extracted (by equating coefficients of $k^{2\lambda} q^{2\mu} (\vec{k} \cdot \vec{q})^\nu$) from

$$\begin{aligned} \sum_{\lambda, \mu, \nu} D_{\lambda\mu\nu} k^{2\lambda} q^{2\mu} (\vec{k} \cdot \vec{q})^\nu &\equiv \sum_{a, b, c=0}^N (-1)^{a+b+c} d_a^A d_b^B d_c^C \\ &\times \sqrt{8 a! b! c! \Gamma(a + L_A + \frac{3}{2}) \Gamma(b + L_B + \frac{3}{2}) \Gamma(c + L_C + \frac{3}{2})} \\ &\times \sum_{m_a=0}^a \sum_{m_b=0}^b \sum_{m_c=0}^c (-1)^{m_a+m_b+m_c} \frac{1}{\beta_A^{2m_a} \beta_B^{2m_b} \beta_C^{2m_c}} \frac{1}{(a-m_a)!(b-m_b)!(c-m_c)!} \end{aligned}$$

$$\begin{aligned}
& \times \frac{1}{\Gamma(m_a + L_A + \frac{3}{2}) \Gamma(m_b + L_B + \frac{3}{2}) \Gamma(m_c + L_C + \frac{3}{2})} \\
& \times \sum_{a_1=0}^{m_a} \sum_{a_2=0}^{m_a-a_1} \sum_{b_1=0}^{m_b} \sum_{b_2=0}^{m_b-b_1} \sum_{c_1=0}^{m_c} \sum_{c_2=0}^{m_c-c_1} \frac{2^{a_3+b_3+c_3}}{a_1! a_2! a_3! b_1! b_2! b_3! c_1! c_2! c_3!} x^{a_3+2a_1} \\
& \times \left(x - \frac{m_1}{m_1+m_3} \right)^{b_3+2b_1} \left(x - \frac{m_2}{m_2+m_3} \right)^{c_3+2c_1} (k^2)^{a_1+b_1+c_1} (q^2)^{a_2+b_2+c_2} (\vec{k} \cdot \vec{q})^{a_3+b_3+c_3},
\end{aligned} \tag{2.20}$$

where $a_3 \equiv m_a - a_1 - a_2$, $b_3 \equiv m_b - b_1 - b_2$ and $c_3 \equiv m_c - c_1 - c_2$.

These expressions are general: they can be used for any meson decay where the radial portion of the wavefunctions can be expanded in terms of SHO radial wavefunctions. In order to obtain symbolic results in terms of the various parameters, we coded these expressions into routines for the symbolic computation package Mathematica [12]. In principle, these routines are limited only by the size of the symbolic problem that results, and the available computer resources – in practice, decays involving mesons with more complicated wavefunctions (i.e. having high N in Eq. 2.9, or high L) would have to be done numerically. The overlaps of the colour, flavour and spin wavefunctions of the mesons and the created pair are calculated using the techniques of Appendix D.

2.3 The Flux-tube Breaking Model of Meson Decay

In the flux-tube picture a meson consists of a quark and antiquark connected by a tube of chromoelectric flux, which can be treated as a vibrating string. For mesons the string is in its vibrational ground state. (Vibrational excitations of the string would correspond to a type of meson hybrid, particles whose existence have not yet been confirmed.) Meson decay occurs when the flux-tube breaks at a point, and a

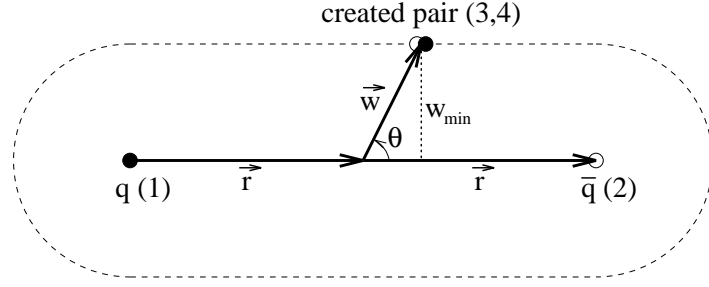


Figure 2.2: The position-space coordinates used in the flux-tube model. The cigar-shaped dashed line shows a possible surface of constant w_{\min} .

quark-antiquark pair is created from the vacuum to connect to the free ends of the flux-tubes, leaving a final state consisting of two mesons.

The flux-tube breaking model of meson decay is similar to the 3P_0 model, but extends it by considering the actual dynamics of the flux-tubes. This is done by including a factor representing the overlap of the flux-tube of the initial meson with those of the two outgoing mesons. Kokoski and Isgur [5] have calculated this factor by treating the flux-tubes as vibrating strings. They approximate the rather complicated result by replacing the undetermined parameter γ in the 3P_0 model with a function of the location of the created quark-antiquark pair, and a new undetermined parameter γ_0 :

$$\gamma(\vec{r}, \vec{w}) = \gamma_0 e^{-\frac{1}{2}bw_{\min}^2}. \quad (2.21)$$

Here b is the string tension, where a value of 0.18 GeV^2 is typically used, and w_{\min} is the shortest distance from the line segment connecting the original quark and antiquark to the location at which the new quark-antiquark pair is created from the vacuum (see Figure 2.2):

$$w_{\min}^2 = \begin{cases} w^2 \sin^2 \theta, & \text{if } r \geq w |\cos \theta| \\ r^2 + w^2 - 2rw |\cos \theta|, & \text{if } r < w |\cos \theta| \end{cases}. \quad (2.22)$$

To incorporate this into the 3P_0 model, we first Fourier transform Eq. 2.8 so that the integral is over position-space. We then pull the parameter γ (from Eq. 2.7) inside the integral, and replace it by the function of position $\gamma(\vec{r}, \vec{w})$. The expression for the amplitude in the flux-tube model is then the same as that of Eq. 2.7 except that γ is replaced by γ_0 , and $I(\vec{P}, m_1, m_2, m_3)$ is replaced by

$$I^{\text{ft}}(\vec{P}, m_1, m_2, m_3) = -\frac{8}{(2\pi)^{\frac{3}{2}}} \int d^3\vec{r} \int d^3\vec{w} \psi_{n_B L_B M_{L_B}}^*(-\vec{w} - \vec{r}) \psi_{n_C L_C M_{L_C}}^*(\vec{w} - \vec{r}) \\ \times \mathcal{Y}_1^m \left(\left[(\vec{P} + i\vec{\nabla}_{\vec{r}_A}) \psi_{n_A L_A M_{L_A}}(\vec{r}_A) \right]_{\vec{r}_A=-2\vec{r}} \right) e^{-\frac{1}{2}bw_{\min}^2} e^{i\vec{P} \cdot (m_+ \vec{r} + m_- \vec{w})} \quad (2.23)$$

where $m_+ = \frac{m_1}{m_1+m_3} + \frac{m_2}{m_2+m_3}$, $m_- = \frac{m_1}{m_1+m_3} - \frac{m_2}{m_2+m_3}$ and the ψ 's are now the relative wavefunctions in position-space. The last exponential function in Eq. 2.23 is the combination of the plane waves representing the CM motion of mesons B and C (the plane wave for A is unity, since it is at rest in the CM frame). It comes from Fourier-transforming the delta-functions implicit in Eq. 2.1 that specify that the CM momenta of the mesons are held fixed to constant values. Note also that we chose to apply the gradient in the argument of the solid harmonic to $\psi_{n_A L_A M_{L_A}}$ only. We could have manipulated the Fourier-transform⁶ to apply it to just $\psi_{n_B L_B M_{L_B}}^*$ or $\psi_{n_C L_C M_{L_C}}^*$, or some combination of all three. In fact since B and C , being lighter than A , tend to be less excited, choosing the wavefunctions of B or C would in general be simpler.

⁶A word of explanation: $\frac{\vec{p}_3 - \vec{p}_4}{2}$ in Eq. 2.6 is rewritten as \vec{p}_0 , the relative momentum of the created pair. Depending on which delta functions from the anticommutators of the annihilation and creation operators we use to replace \vec{p}_0 before doing the Fourier-transform, we end up with different combinations of \vec{p}_A , \vec{p}_B and \vec{p}_C in the argument of the solid harmonic. Each \vec{p}_i becomes a gradient applied to $\psi_{n_i L_i M_{L_i}}$ during the Fourier-transform.

2.4 Calculating Meson Decay Widths with the Flux-tube Breaking Model

In order to calculate the decay amplitudes of the flux-tube breaking model, there are a number of integrals that must be evaluated: two 3-dimensional integrals from Eq. 2.23 and, if we choose to use the recoupling calculation to convert to partial wave amplitudes (see Appendix E), another 2-dimensional integral from Eq. E.4.

We wish to develop general routines to calculate any decay amplitude. This prevents us from making the common assumptions that can simplify Eq. 2.23, such as neglecting mass differences between the quarks, restricting the orbital angular momenta of each meson to be 0 or 1 so that their spherical harmonics can be expressed as dot products of their argument and a constant vector, or simplifying the definition of w_{\min} to remove the complication that arises for $r < w |\cos \theta|$ (i.e. the definition currently used for $r \geq w |\cos \theta|$ would be used for all values). The main goal of simplifying Eq. 2.23 is to allow more of the integrals to be done analytically, to reduce the computer time required for a calculation.

In order to save ourselves two integrations, we choose to use the Jacob-Wick formula to convert to partial wave amplitudes (see Appendix E). (Remember that this involves choosing \vec{P} to lie along \hat{z} , the z axis.) This leaves us with integrals over the variables r , θ_r , ϕ_r , w , θ_w , and ϕ_w . The divided form of Eq. 2.22 suggests that we will not be able to do the integrals over any of the variables on which it depends. This immediately rules out r and w . If \vec{r} and \vec{w} are expressed in the same coordinate system, the angle between them (θ) is given by

$$\cos \theta = \sin \theta_r \sin \theta_w \cos (\phi_r - \phi_w) + \cos \theta_r \cos \theta_w \quad (2.24)$$

which presents a problem for the other variables as well. The solution is to use the

freedom to choose the coordinate system of w to set \hat{z}_w to lie along \vec{r} . We also choose to orient \hat{x}_w and \hat{y}_w such that the original $\hat{z} = \hat{z}_r$ axis has $\phi_w = 0$ in the w coordinate system. Then $\theta = \theta_w$, and

$$\begin{aligned}\vec{r} \cdot \vec{P} &= rP \cos \theta_r \\ \vec{w} \cdot \vec{P} &= wP [\sin \theta_r \sin \theta_w \cos \phi_w + \cos \theta_r \cos \theta_w].\end{aligned}\quad (2.25)$$

A wrinkle with this approach is that in Eq. 2.23 we also have expressions like $\vec{w} - \vec{r}$, where the vectors must be expressed in the same coordinate system. The expression will have to be replaced by $R^{-1}(\phi_r, \theta_r, \pi)\vec{w} - \vec{r}$, where $R(\phi_r, \theta_r, \pi)$ is the active rotation of a vector in the \vec{r} coordinate system to one in the \vec{w} coordinate system. To evaluate the angular part of an expression such as $\psi_{n_B L_B M_{L_B}}^*(-R^{-1}(\phi_r, \theta_r, \pi)\vec{w} - \vec{r})$, we first use the following identity for solid harmonics

$$\mathcal{Y}_l^m(\alpha_1 \vec{r}_1 + \alpha_2 \vec{r}_2) = \sum_{l_1=0}^l C_{l_1}^l \alpha_1^{l_1} \alpha_2^{l-l_1} \sum_{m_1=-l_1}^{l_1} \langle l_1 m_1 | l - l_1 | m - m_1 \rangle \mathcal{Y}_{l_1}^{m_1}(\vec{r}_1) \mathcal{Y}_{l-l_1}^{m-m_1}(\vec{r}_2), \quad (2.26)$$

where $C_{l_1}^l$ is defined in Eq. 2.16. Then to handle the rotation we make use of the following result

$$\mathcal{Y}_l^{*m}(R^{-1}(\phi_r, \theta_r, \pi)\vec{w}) = [\mathcal{R}(\phi_r, \theta_r, \pi)\mathcal{Y}_l^m(\vec{w})]^* = \sum_{m'=-l}^l D_{mm'}^l(\phi_r, \theta_r, \pi) \mathcal{Y}_l^{*m'}(\vec{w}), \quad (2.27)$$

where $D_{mm'}^l(\phi_r, \theta_r, \pi)$ is a rotation matrix.

The final wrinkle is that the substitution for \vec{P} required in the evaluation of $I^{\text{ft}}(-\vec{P}, m_2, m_1, m_3)$ requires more than just taking $P \rightarrow -P$ when two different coordinate systems are used for \vec{r} and \vec{w} . The solution is to first use the symmetry

properties of the angular parts of the wavefunctions to obtain

$$I^{\text{ft}}(-\vec{P}, m_2, m_1, m_3) = (-1)^{1+L_A+L_B+L_C} I^{\text{ft}}(\vec{P}, m_2, m_1, m_3), \quad (2.28)$$

after which our particular choice for the \vec{w} coordinate system can be used to evaluate the dot products. At this stage, the expression for the partial wave amplitudes is (before applying Eqs. 2.26 and 2.27)

$$\begin{aligned} M^{SL}(P) = \gamma_0 \frac{\sqrt{32\pi(2L+1)E_A E_B E_C}}{2J_A + 1} \sum_{\substack{M_{L_A}, M_{S_A}, M_{L_B}, M_{S_B}, M_{J_B}, \\ M_{L_C}, M_{S_C}, M_{J_C}, m}} & \times \langle L0S(M_{J_B} + M_{J_C}) | J_A(M_{J_B} + M_{J_C}) \rangle \langle J_B M_{J_B} J_C M_{J_C} | S(M_{J_B} + M_{J_C}) \rangle \\ & \times \langle L_A M_{L_A} S_A M_{S_A} | J_A(M_{J_B} + M_{J_C}) \rangle \langle L_B M_{L_B} S_B M_{S_B} | J_B M_{J_B} \rangle \\ & \times \langle L_C M_{L_C} S_C M_{S_C} | J_C M_{J_C} \rangle \langle 1m 1-m | 00 \rangle \langle \chi_{S_B M_{S_B}}^{14} \chi_{S_C M_{S_C}}^{32} | \chi_{S_A M_{S_A}}^{12} \chi_{1-m}^{34} \rangle \\ & \times \left[\langle \phi_B^{14} \phi_C^{32} | \phi_A^{12} \phi_0^{34} \rangle I^{\text{ft}}(P\hat{z}, m_1, m_2, m_3) \right. \\ & \left. + (-1)^{L_A+L_B+L_C+S_A+S_B+S_C} \langle \phi_B^{32} \phi_C^{14} | \phi_A^{12} \phi_0^{34} \rangle I^{\text{ft}}(P\hat{z}, m_2, m_1, m_3) \right] \end{aligned} \quad (2.29)$$

where

$$\begin{aligned} I^{\text{ft}}(P\hat{z}, m_1, m_2, m_3) = & -\frac{8}{(2\pi)^{\frac{3}{2}}} \int_0^\infty dr \int_0^\infty dw \int_{-1}^1 d(\cos \theta_w) r^2 w^2 e^{-\frac{1}{2}bw_{\min}^2} \\ & \times \int_{-1}^1 d(\cos \theta_r) e^{im_- Pw \cos \theta_r \cos \theta_w + im_+ Pr \cos \theta_r} \\ & \times \int_0^{2\pi} d\phi_r \mathcal{Y}_1^m \left(\left[(P\hat{z} + i\vec{\nabla}_{\vec{r}_A}) \psi_{n_A L_A M_{L_A}}(\vec{r}_A) \right]_{\vec{r}_A=-2\vec{r}} \right) \\ & \times \int_0^{2\pi} d\phi_w e^{im_- Pw \sin \theta_r \sin \theta_w \cos \phi_w} \psi_{n_B L_B M_{L_B}}^*(-R^{-1}(\phi_r, \theta_r, \pi) \vec{w} - \vec{r}) \\ & \times \psi_{n_C L_C M_{L_C}}^*(R^{-1}(\phi_r, \theta_r, \pi) \vec{w} - \vec{r}). \end{aligned} \quad (2.30)$$

We can now carry out the θ_r , ϕ_r and ϕ_w integrations analytically, in principle. In practice, we will only do those for ϕ_r and ϕ_w . The integral over ϕ_w is done by means of

the residue theorem. The integral over ϕ_r depends upon the form of the wavefunction of meson A – we will again assume that the radial portions of the meson wavefunctions are expressed as linear combinations of the first $N + 1$ SHO radial wavefunctions, as in Eq. 2.9. Once this assumption is made, the ϕ_r integral does not require any special techniques; the final result after doing it is rather complicated but we give it here for completeness:

$$\begin{aligned}
M^{SL}(P) = & \int_0^\infty dr \int_0^\infty dw \int_0^\pi d\theta_r \int_0^\pi d\theta_w g_1(r, w, \theta_r, \theta_w) \sqrt{2L+1} \\
& \times \sum_{M_{J_B}, M_{J_C}} \langle L0S(M_{J_B} + M_{J_C}) | J_A(M_{J_B} + M_{J_C}) \rangle \langle J_B M_{J_B} J_C M_{J_C} | S(M_{J_B} + M_{J_C}) \rangle \\
& \times \sum_{M_{L_A}, M_{L_B}, M_{L_C}} \langle L_A M_{L_A} S_A(M_{J_B} + M_{J_C} - M_{L_A}) | J_A(M_{J_B} + M_{J_C}) \rangle \\
& \times \langle L_B M_{L_B} S_B(M_{J_B} - M_{L_B}) | J_B M_{J_B} \rangle \langle L_C M_{L_C} S_C(M_{J_C} - M_{L_C}) | J_C M_{J_C} \rangle \\
& \times \langle 1(M_{L_B} + M_{L_C} - M_{L_A}) 1(M_{L_A} - M_{L_B} - M_{L_C}) | 00 \rangle \\
& \times \langle \chi_{S_B(M_{J_B} - M_{L_B})}^{14} \chi_{S_C(M_{J_C} - M_{L_C})}^{32} | \chi_{S_A(M_{J_B} + M_{J_C} - M_{L_A})}^{12} \chi_{1(M_{L_A} - M_{L_B} - M_{L_C})}^{34} \rangle \\
& \times \sqrt{\frac{(L_A - M_{L_A})!}{(L_A + M_{L_A})!}} \sum_{l_1=0}^{L_B} \sum_{l_2=0}^{L_C} (-1)^{L_C - l_2} C_{l_1}^{L_B} C_{l_2}^{L_C} r^{L_B + L_C - l_1 - l_2} w^{l_1 + l_2} \\
& \times \sum_{m_{l_1} m_{l_2}} \sum_{l_1 l_2} \langle l_1 m_{l_1} (L_B - l_1) (M_{L_B} - m_{l_1}) | L_B M_{L_B} \rangle \langle l_2 m_{l_2} (L_C - l_2) (M_{L_C} - m_{l_2}) | L_C M_{L_C} \rangle \\
& \times \sqrt{[2(L_B - l_1) + 1] [2(L_C - l_2) + 1] \frac{(L_B - l_1 - M_{L_B} + m_{l_1})! (L_C - l_2 - M_{L_C} + m_{l_2})!}{(L_B - l_1 + M_{L_B} - m_{l_1})! (L_C - l_2 + M_{L_C} - m_{l_2})!}} \\
& \times P_{L_B - l_1}^{M_{L_B} - m_{l_1}}(\cos \theta_r) P_{L_C - l_2}^{M_{L_C} - m_{l_2}}(\cos \theta_r) \\
& \times \sum_{m'=-l_1}^{l_1} \sum_{m''=-l_2}^{l_2} \sqrt{(2l_1 + 1) (2l_2 + 1) \frac{(l_1 - m')! (l_2 - m'')!}{(l_1 + m')! (l_2 + m'')!}} (-1)^{m' + m''} \\
& \times d_{m_{l_1} m'}^{l_1}(\theta_r) d_{m_{l_2} m''}^{l_2}(\theta_r) P_{l_1}^{m'}(\cos \theta_w) P_{l_2}^{m''}(\cos \theta_w) e^{im_+ P r \cos \theta_r} \\
& \times [ig_2(M_{L_A}, M_{L_B} + M_{L_C}, r, \theta_r) + g_3(M_{L_A}, M_{L_B} + M_{L_C}, r, \theta_r)] \\
& \times \left[\langle \phi_B^{14} \phi_C^{32} | \phi_A^{12} \phi_0^{34} \rangle e^{im_- P w \cos \theta_r \cos \theta_w} i^{|m' + m''|} \text{sign}^{|m' + m''|} (m_- P w \sin \theta_r \sin \theta_w) \right. \\
& \times J_{|m' + m''|}(|m_- P w \sin \theta_r \sin \theta_w|) \left. \right]
\end{aligned}$$

$$\begin{aligned}
& + (-1)^{L_A+L_B+L_C+S_A+S_B+S_C} \langle \phi_B^{32} \phi_C^{14} | \phi_A^{12} \phi_0^{34} \rangle e^{-im_- Pw \cos \theta_r \cos \theta_w} i^{|m'|+m''|} \\
& \times \text{sign}^{|m'|+m''|} (-m_- Pw \sin \theta_r \sin \theta_w) J_{|m'|+m''|} (|m_- Pw \sin \theta_r \sin \theta_w|) \Big] \quad (2.31)
\end{aligned}$$

where $d_{mm'}^l(\theta)$ is related to the rotation matrix by

$$D_{mm'}^l(\phi, \theta, \chi) \equiv e^{-im\phi} d_{mm'}^l(\theta) e^{-im'\chi}, \quad (2.32)$$

$P_l^m(x)$ is an associated Legendre function, $J_l(x)$ is a Bessel function of the first kind, and $\text{sign}(x)$ is +1 if $x \geq 0$ and -1 if $x < 0$. The g functions are given by

$$\begin{aligned}
g_1(r, w, \theta_r, \theta_w) & \equiv \frac{-\sqrt{3}}{2\pi^2} \frac{\sqrt{2L_A+1}}{2J_A+1} \sqrt{E_A E_B E_C} (-1)^{L_B} \beta_A^{L_A+\frac{3}{2}} \beta_B^{L_B+\frac{3}{2}} \beta_A^{L_B+\frac{3}{2}} \\
& \times r^2 w^2 \sin \theta_r \sin \theta_w \gamma(r, w, \theta_w) (-2r)^{L_A-1} \\
& \times e^{-2\beta_A^2 r^2} e^{-\beta_B^2(r^2 + w^2 + 2rw \cos \theta_w)/2} e^{-\beta_C^2(r^2 + w^2 - 2rw \cos \theta_w)/2} \\
& \times \left[\sum_{b=0}^N d_b^B \sqrt{\frac{2 b!}{\Gamma(b+L_B+\frac{3}{2})}} L_b^{L_B+\frac{1}{2}}(\beta_B^2(r^2 + w^2 + 2rw \cos \theta_w)) \right] \\
& \times \left[\sum_{c=0}^N d_c^C \sqrt{\frac{2 c!}{\Gamma(c+L_C+\frac{3}{2})}} L_c^{L_C+\frac{1}{2}}(\beta_C^2(r^2 + w^2 - 2rw \cos \theta_w)) \right], \quad (2.33)
\end{aligned}$$

$$g_2(M_{L_A}, M_{L_B}+M_{L_C}, r, \theta_r) \equiv$$

$$\begin{aligned}
& \left[\sqrt{2} \sin \theta_r (\delta_{M_{L_A}-M_{L_B}-M_{L_C}, 1} - \delta_{M_{L_A}-M_{L_B}-M_{L_C}, -1}) + 2 \cos \theta_r \delta_{M_{L_A}-M_{L_B}-M_{L_C}, 0} \right] \\
& \times P_{L_A}^{M_{L_A}}(\cos \theta_r) \left[\sum_{a=0}^N d_a^A \sqrt{\frac{2 a!}{\Gamma(a+L_A+\frac{3}{2})}} \left((L_A - 4\beta_A^2 r^2) L_a^{L_A+\frac{1}{2}}(4\beta_A^2 r^2) \right. \right. \\
& \quad \left. \left. - 8\beta_A^2 r^2 \begin{cases} 0, & \text{if } a=0 \\ L_{a-1}^{L_A+\frac{3}{2}}(4\beta_A^2 r^2), & \text{if } a \geq 1 \end{cases} \right) \right] \\
& + \left\{ \left[\sqrt{2} \cos \theta_r (\delta_{M_{L_A}-M_{L_B}-M_{L_C}, 1} - \delta_{M_{L_A}-M_{L_B}-M_{L_C}, -1}) - 2 \sin \theta_r \delta_{M_{L_A}-M_{L_B}-M_{L_C}, 0} \right] \right. \\
& \quad \times \frac{1}{\sin \theta_r} \left[L_A \cos \theta_r P_{L_A}^{M_{L_A}}(\cos \theta_r) - (L_A + M_{L_A}) P_{L_A-1}^{M_{L_A}}(\cos \theta_r) \right] \\
& \quad \left. + \frac{\sqrt{2} M_{L_A}}{\sin \theta_r} (\delta_{M_{L_A}-M_{L_B}-M_{L_C}, 1} + \delta_{M_{L_A}-M_{L_B}-M_{L_C}, -1}) P_{L_A}^{M_{L_A}}(\cos \theta_r) \right\}
\end{aligned}$$

$$\times \left[\sum_{a=0}^N d_a^A \sqrt{\frac{2 a!}{\Gamma(a + L_A + \frac{3}{2})}} L_a^{L_A + \frac{1}{2}}(4\beta_A^2 r^2) \right], \quad (2.34)$$

$$g_3(M_{L_A}, M_{L_B} + M_{L_C}, r, \theta_r) \equiv -4Pr \delta_{M_{L_A} - M_{L_B} - M_{L_C}, 0} P_{L_A}^{M_{L_A}}(\cos \theta_r) \\ \times \left[\sum_{a=0}^N d_a^A \sqrt{\frac{2 a!}{\Gamma(a + L_A + \frac{3}{2})}} L_a^{L_A + \frac{1}{2}}(4\beta_A^2 r^2) \right], \quad (2.35)$$

where $L_n^k(x)$ is an associated Laguerre polynomial.

We have automated the calculation of partial wave amplitudes with these expressions, using routines written for Mathematica [12] and FORTRAN. In the Mathematica code, an integrand for each partial wave amplitude is prepared symbolically and converted to FORTRAN code. The FORTRAN program carries out the integrations numerically using either adaptive Monte Carlo (VEGAS [13]) or a combination of adaptive Gaussian quadrature routines. Again, these routines are usable for any meson decay where the radial portion of the wavefunctions can be expanded in terms of SHO wavefunctions, and are limited only by the size of the problem and the available computer resources. The overlaps of the colour, flavour and spin wavefunctions of the mesons and the created pair are calculated using the techniques of Appendix D.

Chapter 3

Models of Meson Decay: Two Applications

3.1 Setting the Parameters of the Models

In order to use the models of meson decay introduced in Chapter 2 we must fit the undetermined parameter γ (γ_0 for the flux-tube breaking model), and we must decide which meson space wavefunctions to use. In addition, we must decide which phase space/normalization is best suited to our purposes – we discuss this below.

In this section we consider three types of space wavefunctions, described in some detail in Appendix B.1: SHO wavefunctions with a common oscillator parameter (β), wavefunctions from the relativized quark model (RQM) [4] of Godfrey and Isgur described in Section 1.2.2, and SHO wavefunctions with the effective β ’s of Kokoski and Isgur [5]. The RQM wavefunctions and SHO wavefunctions with effective β ’s are fully determined and have no parameters left to choose. For the SHO wavefunctions with a common β , we take $\beta = 400$ MeV, the value used by Kokoski and Isgur which lies safely within the range of the effective values fitted by them for the various mesons. We also perform another fit of both γ and β simultaneously.

We must also decide how to normalize the mock meson wavefunctions and what kind of phase space to use to calculate the decay widths [14]. We investigate three choices. In Chapter 2 we normalized the mock meson wavefunctions relativistically to $2E$ (Eq. 2.2) and used relativistic phase space (leading to Eq. 2.5), which leads to a factor of $E_B E_C / M_A$ in the final expression for a decay width in the CM frame (E is energy, M is mass). We will refer to this as relativistic phase space/normalization (RPSN). One could also argue that since our decay models are primarily nonrelativistic, it makes sense to use a nonrelativistic normalization and nonrelativistic phase space, which would replace the factor by $M_B M_C / M_A$. We will refer to this as non-relativistic phase space/normalization (NRPSN). However, there are also arguments [15] that heavy quark effective theory fixes the assumptions in the mock meson prescription and suggests that the factor be replaced by $\widetilde{M}_B \widetilde{M}_C / \widetilde{M}_A$, where the \widetilde{M}_i are the calculated masses of the meson i in a spin-independent quark-antiquark potential [5].¹ We will refer to this as the Kokoski-Isgur phase space/normalization (KIPSN).

Some comments about the details of the calculations made in this chapter are in order. For both types of SHO wavefunctions we use quark masses in the ratio $m_u : m_d : m_s = 3 : 3 : 5$ – this differs from the calculations of Kokoski and Isgur [5], which ignored the strange-quark mass difference. For the RQM wavefunctions the quark masses have already been fitted: $m_u = 220$ MeV, $m_d = 220$ MeV, and $m_s = 419$ MeV. We treat all mesons as narrow resonances. Meson masses are taken from the Review of Particle Properties 1994 [1] if the state is included in their Meson Summary Table². If it is not, then the masses predicted in Ref. [4] are used. This includes the masses of the 1^3F_2 , 1^3F_3 and 1^3F_4 $s\bar{s}$ mesons: 2240 MeV, 2230 MeV and 2200 MeV respectively. We ignore mass differences between members of the same

¹In other words \widetilde{M}_i is given by the hyperfine averaged mass that is equal to the centre of gravity of the triplet and singlet masses of a meson multiplet of given orbital angular momentum L . The main effect of KIPSN is that the widths of decays with pseudoscalars in the final state are increased.

²The one exception was the 1^3P_0 $s\bar{s}$ state – see Table 3.7.

isospin multiplet³ and average over the quoted masses, if different. Meson flavour wavefunctions are also taken from Ref. [4], and are summarized in Appendix B.2⁴.

In order to evaluate the above wavefunctions and phase space/normalization schemes and to fit the value of γ (γ_0) we carried out a series of least squares fits of the model predictions to the decay widths of 28 of the best known⁵ meson decays; we minimized the quantity defined by $\chi^2 = \sum_i (\Gamma_i^{model} - \Gamma_i^{exp})^2 / \sigma_{\Gamma_i}^2$ where σ_{Γ_i} is the experimental error.⁶ The 28 decays used, and the experimental values of their widths [1], are shown in Table 3.1.

The ratios of the model predictions to the experimental values for the widths of the 28 decays are plotted in Figures 3.1 to 3.5, on logarithmic scales. The fitted values of γ (γ_0) and the resulting χ^2 per degree of freedom (dof) are listed in Table 3.2. We do not quote errors on the fitted values of γ (γ_0) because they are negligible (being at most a change in the last digit quoted) compared to the inherent uncertainties of the models. We have performed fits for the 3P_0 model with both types of SHO wavefunctions, and for the flux-tube breaking model with all three types of wavefunctions. We did not use the RQM wavefunctions with the 3P_0 model because the large number (up to 13) of radial SHO wavefunctions in the linear combination (see Eq. 2.9) exceeds the capacity of our symbolic routines on the available computer hardware⁷. Because the results of the 3P_0 and flux-tube breaking models appear to be very similar, we

³The one exception was for the decay $\phi \rightarrow K^+K^-$ where the charged and neutral kaon mass difference is significant to the phase space.

⁴For the η and η' we assumed perfect mixing, corresponding to $\theta_P = -9.7^\circ$, but we also considered the effect that using $\theta_P = -20^\circ$ would have on the results of Tables 3.5 through 3.9. We found that while individual decay widths varied by up to a factor of approximately 2, the changes to the total widths were negligible compared to the other uncertainties of the calculations.

⁵We also required that the decays we selected not involve any particles that undergo significant mixing (e.g. η , η') in order to minimize uncertainties in the calculation.

⁶For the calculations in the flux-tube breaking model, a 1% error due to the numerical integration was added in quadrature with the experimental error.

⁷This problem arises for the 3P_0 model routines, which are symbolic (and hence are slower and require more memory), but not for the flux-tube breaking model routines, where the brunt of the work is done numerically.

Decay	Γ (MeV) from Experiment	Γ (MeV) from Models of Meson Decay					
		3P_0		Flux-tube Breaking			
		SHO		SHO		RQM	
		RPSN	KIPSN	RPSN	KIPSN	RPSN	KIPSN
$\rho \rightarrow \pi\pi$	151.2 ± 1.2	96	148	93	148	104	152
$b_1(1235) \rightarrow \omega\pi$	142 ± 8	176	115	155	104	306	190
$a_2(1320) \rightarrow \rho\pi$	75.0 ± 4.5	65	38	67	40	84	46
$a_2(1320) \rightarrow K\bar{K}$	5.2 ± 0.9	11	8.0	11	8.5	7.3	5.0
$\pi_2(1670) \rightarrow f_2(1270)\pi$	135 ± 11	147	116	143	117	327	246
$\pi_2(1670) \rightarrow \rho\pi$	74 ± 11	232	74	226	74	323	97
$\pi_2(1670) \rightarrow K^*(892)\bar{K}$ +c.c.	10.1 ± 3.4	38	17	37	17	49	21
$\rho_3(1690) \rightarrow \pi\pi$	50.7 ± 5.5	116	35	122	38	68	19
$\rho_3(1690) \rightarrow \omega\pi$	34 ± 13	36	11	39	13	45	13
$\rho_3(1690) \rightarrow K\bar{K}$	3.4 ± 0.6	9.2	3.8	9.7	4.2	4.2	1.7
$f_2(1270) \rightarrow \pi\pi$	156.8 ± 3.2	203	109	209	116	157	80
$f_2(1270) \rightarrow K\bar{K}$	8.6 ± 0.8	7.2	5.4	7.4	5.7	5.0	3.5
$f_4(2050) \rightarrow \omega\omega$	54 ± 13	53	11	54	11	94	18
$f_4(2050) \rightarrow \pi\pi$	35.4 ± 3.8	123	25	132	28	58	11
$f_4(2050) \rightarrow K\bar{K}$	1.4 ± 0.7	5.4	1.6	5.8	1.7	1.8	0.5
$\phi \rightarrow K^+K^-$	2.17 ± 0.05	2.37	2.83	2.28	2.80	2.30	2.60
$f'_2(1525) \rightarrow K\bar{K}$	61 ± 5	117	61	118	64	98	49
$K^*(892) \rightarrow K\pi$	50.2 ± 0.5	36	52	34	51	38	52
$K_0^*(1430) \rightarrow K\pi$	267 ± 36	163	84	117	63	875	430
$K_2^*(1430) \rightarrow K\pi$	48.9 ± 1.7	108	56	112	60	88	43
$K_2^*(1430) \rightarrow K^*(892)\pi$	24.8 ± 1.7	27	16	27	17	31	18
$K_2^*(1430) \rightarrow K\rho$	8.7 ± 0.8	9.3	4.9	9.6	5.2	12	5.8
$K_2^*(1430) \rightarrow K\omega$	2.9 ± 0.8	2.6	1.4	2.6	1.4	3.2	1.6
$K_3^*(1780) \rightarrow K\rho$	74 ± 10	24	7.7	25	8.4	28	8.7
$K_3^*(1780) \rightarrow K^*(892)\pi$	45 ± 7	33	11	34	12	37	12
$K_3^*(1780) \rightarrow K\pi$	31.7 ± 3.7	87	28	92	30	54	16
$K_4^*(2045) \rightarrow K\pi$	19.6 ± 3.8	55	13	59	14	28	6.2
$K_4^*(2045) \rightarrow K^*(892)\phi$	2.8 ± 1.4	3.2	1.0	3.3	1.1	4.7	1.4

Table 3.1: The 28 meson decays used in our fits of the decay models' parameters. The experimental widths are shown, as are the model results for six combinations of decay model, wavefunctions, and phase space/normalization (specified in the second, third and fourth rows of the heading, respectively).

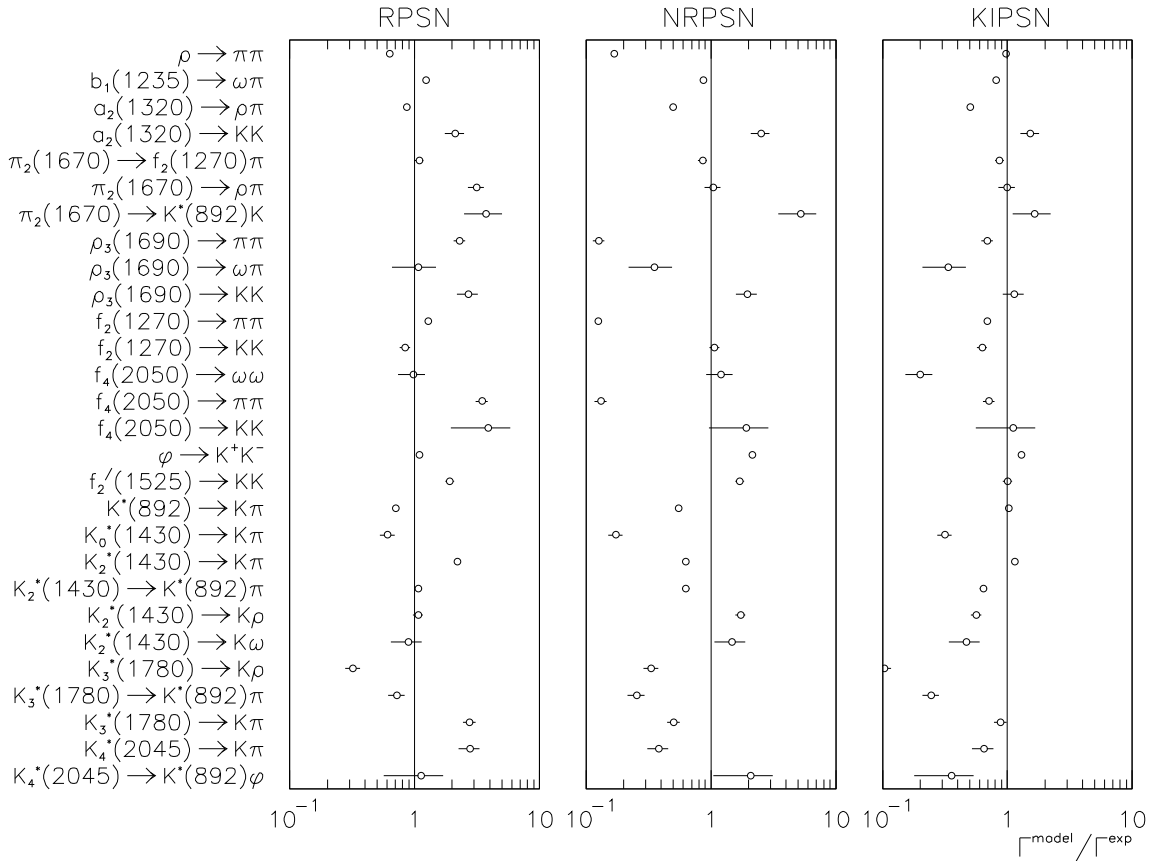


Figure 3.1: Ratios of the predictions of the 3P_0 model of meson decay to the experimental values, for the widths of the 28 decays used in the fits. In this figure SHO wavefunctions with a common β were used. The three graphs use different phase space/normalization schemes.

chose not to write a numerical version of the 3P_0 routines to enable us to use the RQM wavefunctions. For each decay model and wavefunction combination, we tried all three phase space/normalization schemes.

When examining Figures 3.1 to 3.5, note that if a particular model described the data exactly, all the points for it would lie along the vertical solid line at $\Gamma^{\text{model}}/\Gamma^{\text{exp}} = 1$. Because γ (γ_0) is an overall factor in the amplitude, changing it would move all of the points to the left or right by the same amount. Some distributions appear lopsided about $\Gamma^{\text{model}}/\Gamma^{\text{exp}} = 1$, because the experimentally well known decays dominate the

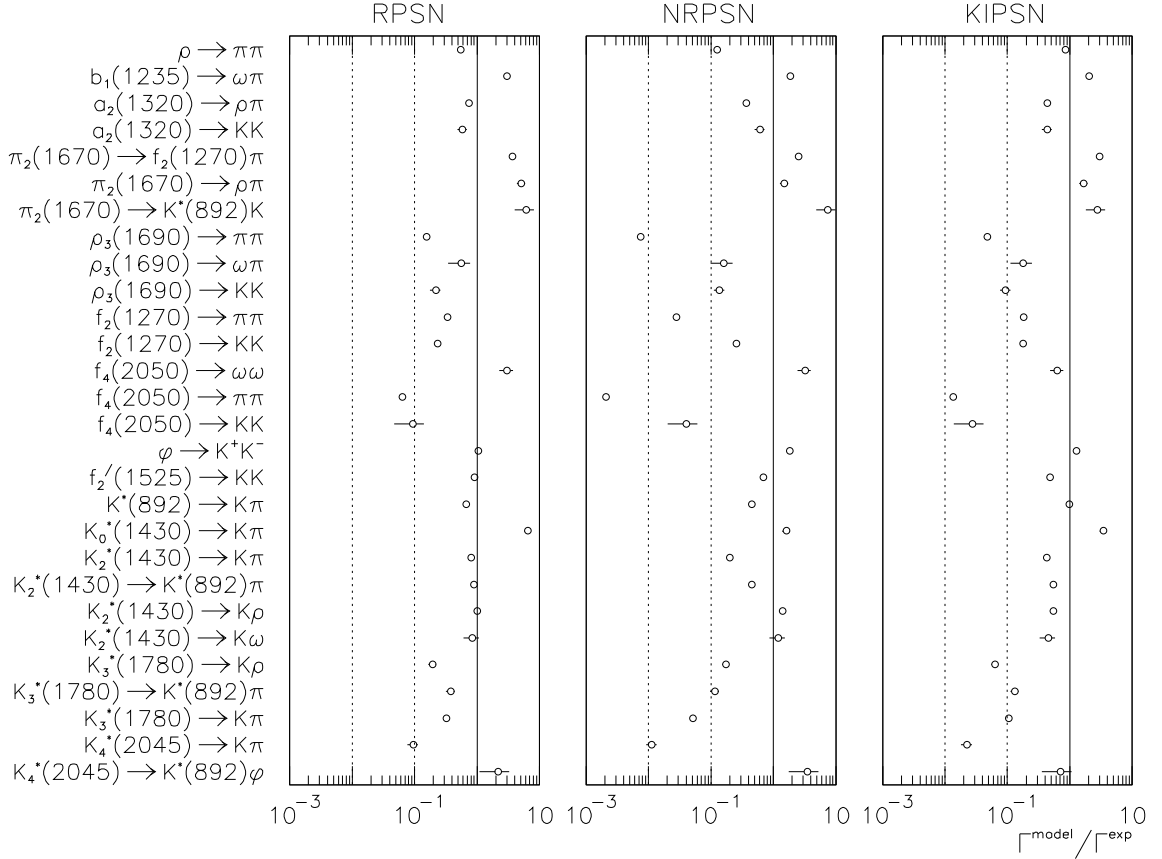


Figure 3.2: Ratios of the predictions of the 3P_0 model of meson decay to the experimental values, for the widths of the 28 decays used in the fits. In this figure SHO wavefunctions with effective β 's were used. The three graphs use different phase space/normalization schemes.

fit.

The first thing to notice from the figures and the χ^2 values of Table 3.2 is that the results with NRPSN are significantly worse than the ones using the other two choices of phase space/normalization. We will hence not use NRPSN for our calculations. Similarly, the SHO wavefunctions with effective β 's do worse than either of the other two types of wavefunctions, and we will not use them either. That leaves us with six different combinations of decay model, wavefunction, and phase space/normalization – these are the combinations given in Table 3.1. Some general comments are in order.

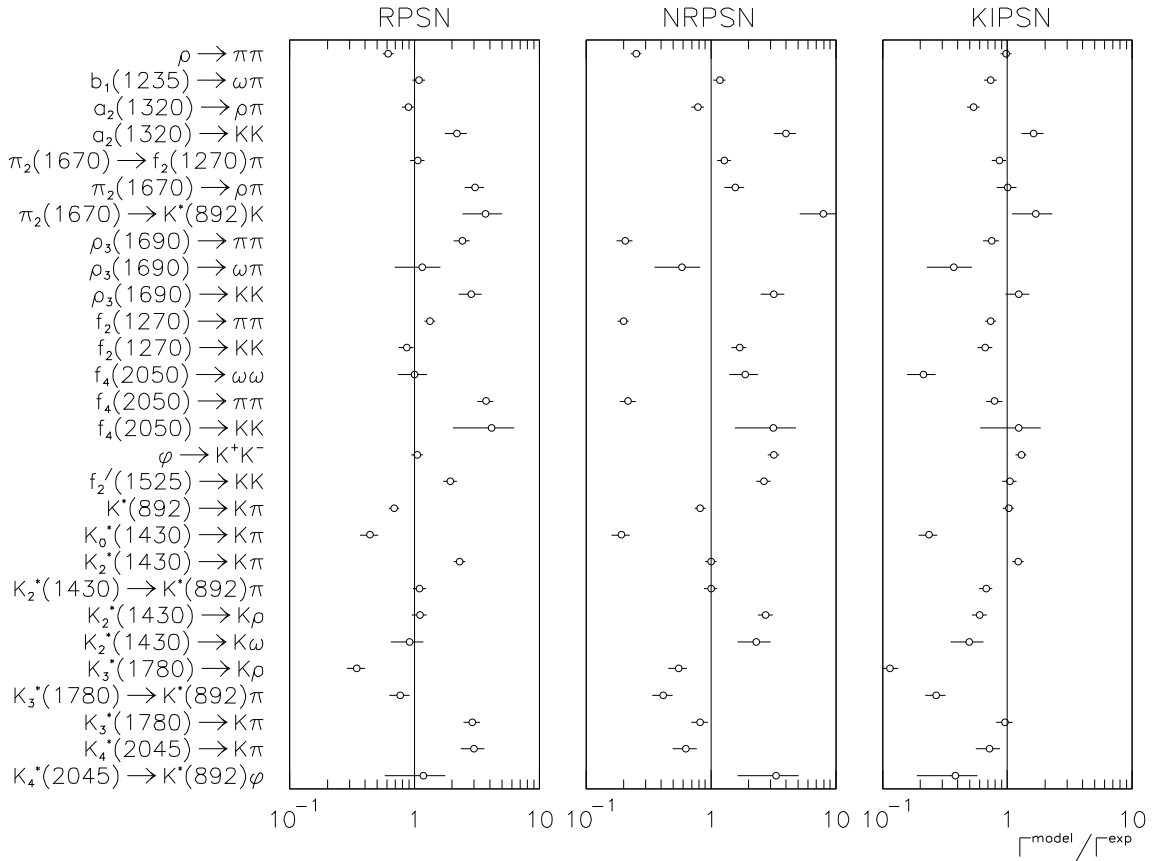


Figure 3.3: Ratios of the predictions of the flux-tube breaking model of meson decay to the experimental values, for the widths of the 28 decays used in the fits. In this figure SHO wavefunctions with a common β were used. The three graphs use different phase space/normalization schemes.

First, the χ^2 values of Table 3.2 make it clear that these models are not very accurate⁸ – the best they can hope for is to predict a decay width to within a factor of 2, and even larger deviations are common. Since they are coarse models of a complicated theory, this is not surprising. In addition, the six combinations can give rather different results. We will use this to our advantage by taking the spread in the predictions of the different combinations as a rough guide to the trustworthiness of

⁸It should be noted that past practice has often been to look for agreement in the amplitudes, rather than the widths, which tends to make the situation look better.

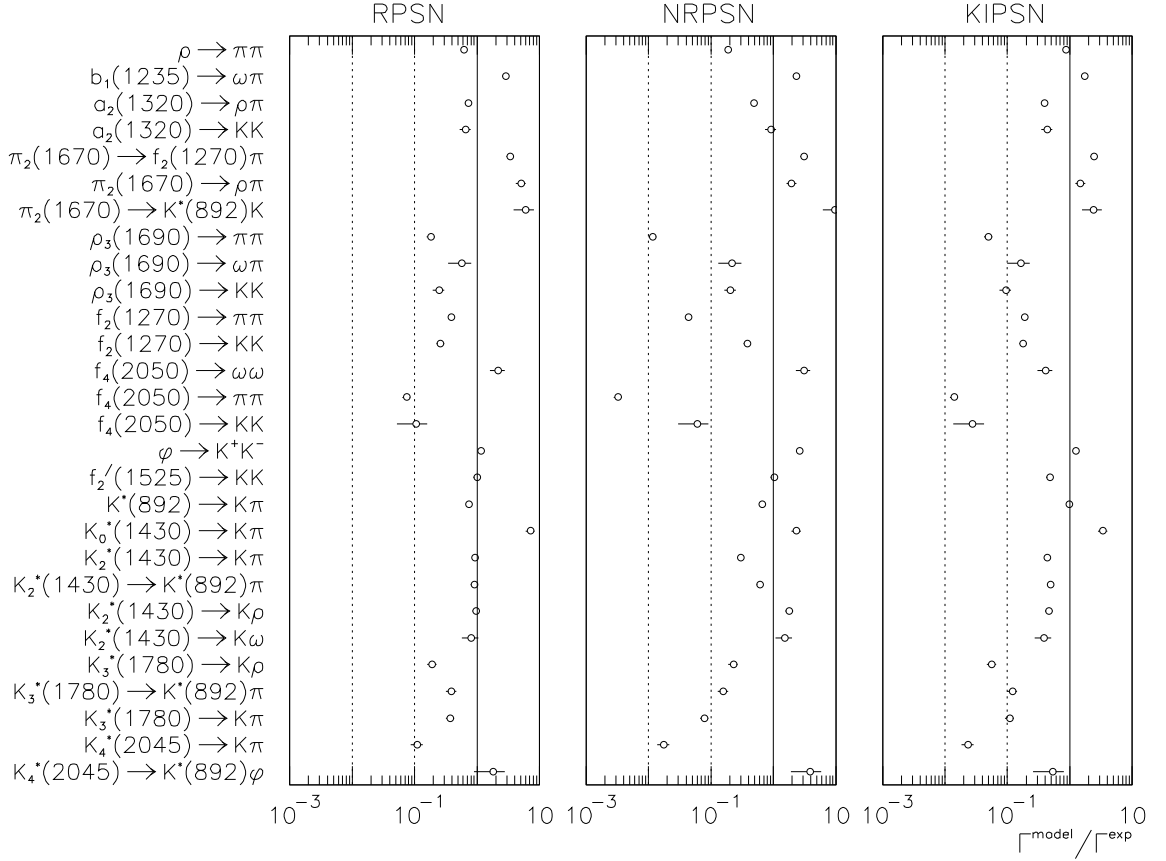


Figure 3.4: Ratios of the predictions of the flux-tube breaking model of meson decay to the experimental values, for the widths of the 28 decays used in the fits. In this figure SHO wavefunctions with effective β 's were used. The three graphs use different phase space/normalization schemes.

the calculations.

From Table 3.1 and Figures 3.1 through 3.5 one can see that the results for the 3P_0 and flux-tube breaking models for the SHO wavefunctions are very similar, as previously noted.⁹ This is in agreement with the observations of Kokoski and Isgur [5], who argued that the overlap of the space wavefunctions in the 3P_0 model makes it unlikely that the decay will proceed if the quark-antiquark pair is created far from

⁹The one exception to this is the S-wave decay $K_0^*(1430) \rightarrow K\pi$ which seems particularly sensitive to the model.

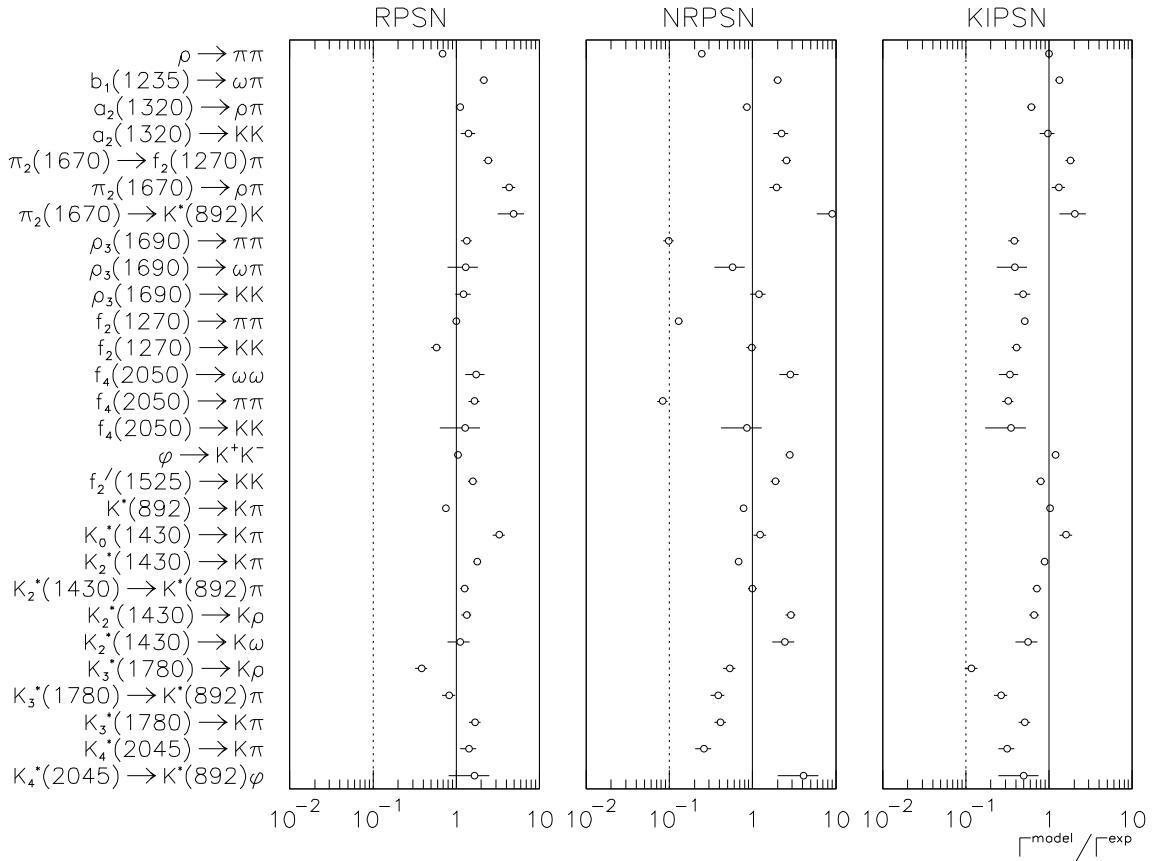


Figure 3.5: Ratios of the predictions of the flux-tube breaking model of meson decay to the experimental values, for the widths of the 28 decays used in the fits. In this figure RQM wavefunctions were used. The three graphs use different phase space/normalization schemes.

a straight line connecting the two mesons. This would have the same effect as the functional form of $\gamma(\vec{r}, \vec{w})$ in the flux-tube breaking model. Despite the similarity in the individual decays, the χ^2 values of the fits are better for the flux-tube breaking model, indicating at least some preference for this model.

In comparing the SHO wavefunctions (we will henceforth only speak of the SHO wavefunctions with a common β) to the RQM wavefunctions, we note that the RQM wavefunctions do better for RPSN, but worse for KIPSN, showing no clear preference.

KIPSN gives better overall fits to the data than RPSN. However, certain decays,

Meson Decay Model	Wavefunctions	Phase Space/Normalization	β	$\gamma (\gamma_0)$	χ^2/dof
3P_0	SHO (common β)	RPSN	400 MeV	9.73	223
		NRPSN		14.1	675
		KIPSN		6.25	26.9
3P_0	SHO (effective β 's)	RPSN	varies	17.6	410
		NRPSN		23.8	776
		KIPSN		11.4	161
Flux-tube Breaking	SHO (common β)	RPSN	400 MeV	16.0	185
		NRPSN		28.7	546
		KIPSN		10.4	22.0
Flux-tube Breaking	SHO (effective β 's)	RPSN	varies	22.1	271
		NRPSN		34.4	663
		KIPSN		13.6	130
Flux-tube Breaking	RQM	RPSN	varies	20.5	128
		NRPSN		34.4	556
		KIPSN		12.8	40.3
3P_0	SHO (common β)	RPSN	481 MeV	13.4	158
		NRPSN	444 MeV	16.5	696
		KIPSN	371 MeV	5.60	26.0

Table 3.2: The details of the various fits of the decay models' parameters, and the resulting χ^2/dof . For the last three fits, both γ and β were fit simultaneously.

$K_3^*(1780) \rightarrow K\rho$ and $f_4(2050) \rightarrow \omega\omega$ for example, are fit better using RPSN. Also, if we wished to remove the dominant effect that the experimentally well known decays have on the fit, we could follow Geiger and Swanson [14] and look at the spread of the values of γ needed to match the model predictions to the experimental values exactly; if $\bar{\gamma}$ is the mean of these γ values, and σ_γ the standard deviation of the distribution, then $\sigma_\gamma/\bar{\gamma}$ provides a measure of the spread of the results that ignores the experimental errors. Using this measure, RPSN is consistently better than KIPSN, as can be seen in Table 3.3.

We can make more specific observations using the SHO wavefunctions: Decays with two pseudoscalars in the final state tend to do better with KIPSN, but KIPSN generally underestimates decays of high L mesons with vector mesons in the final

Meson Decay Model	Wavefunctions	Phase Space/Normalization	β (MeV)	$\bar{\gamma}$	σ_γ	$\sigma_\gamma/\bar{\gamma}$
3P_0	SHO (common β)	RPSN	400	8.73	2.84	0.325
		NRPSN		19.3	10.1	0.527
		KIPSN		8.17	3.15	0.386
3P_0	SHO (effective β 's)	RPSN	varies	25.7	16.3	0.634
		NRPSN		76.4	108	1.41
		KIPSN		26.5	23.0	0.868
Flux-tube Breaking	SHO (common β)	RPSN	400	14.3	4.86	0.339
		NRPSN		31.6	16.9	0.537
		KIPSN		13.4	5.13	0.384
Flux-tube Breaking	SHO (effective β 's)	RPSN	varies	31.0	18.7	0.604
		NRPSN		90.5	124	1.37
		KIPSN		31.9	26.6	0.834
Flux-tube Breaking	RQM	RPSN	varies	18.1	5.02	0.278
		NRPSN		42.1	27.6	0.656
		KIPSN		17.1	6.01	0.351

Table 3.3: The values of $\bar{\gamma}$, σ_γ and $\sigma_\gamma/\bar{\gamma}$ for the 28 decays used in the fits, where the γ (γ_0) value for a decay matches the model prediction to the experimental value. Thus $\sigma_\gamma/\bar{\gamma}$ provides a measure of the spread of the results that ignores the experimental errors.

state. On the other hand RPSN tends to overestimate decays with two pseudoscalars in the final state. Trends can also be observed with the flux-tube breaking model using the RQM wavefunctions. Having said all this we stress that these are only general observations and exceptions can be found to any of them in Table 3.1. One must therefore be very careful not to take any predictions of these models at face value but should try if possible to compare the predicted decay to a similar one that is experimentally well known.

Finally, we consider the sensitivity of our results to β , which we must choose for the SHO wavefunctions. Different quark models predict different values of β , so there is no clear theoretical prediction to draw upon. It should be noted that although meson decay widths can depend strongly on the value of β , to some extent we alleviate this effect because we fit γ to experimental data after selecting a value

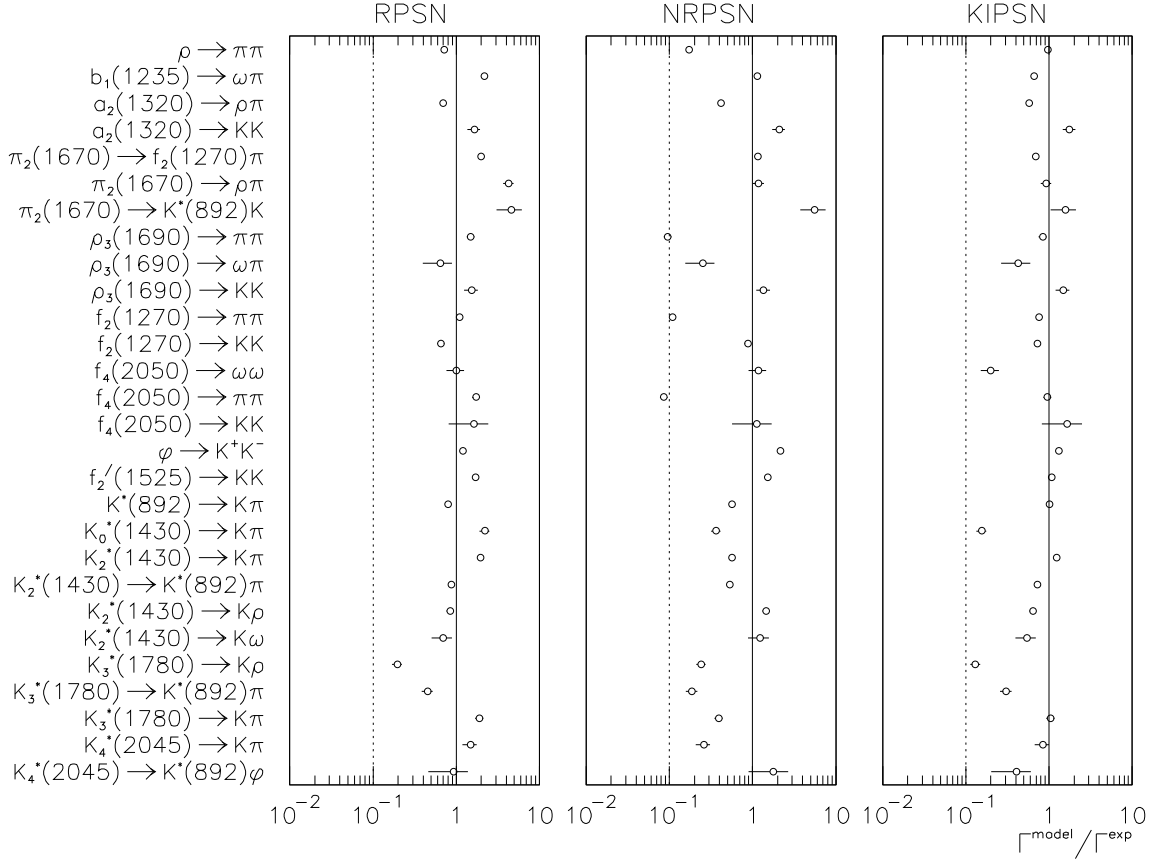


Figure 3.6: Ratios of the predictions of the 3P_0 model of meson decay to the experimental values, for the widths of the 28 decays used in the fits. In this figure SHO wavefunctions with a common β were used, and both β and γ were fit simultaneously. The three graphs use different phase space/normalization schemes.

of β . In the fits discussed above, we took $\beta = 400$ MeV which is the value used by Kokoski and Isgur [5]. In addition to these fits, we performed simultaneous fits of both γ and β to the 28 decay widths – see Figure 3.6. The overall fits improved, but as usual some widths were in better agreement and some in worse agreement with experiment when compared to the fits for $\beta = 400$ MeV. In general we found that the deviation in the results lies within the overall uncertainty we assign to the models, and so we choose to follow the literature and use $\beta = 400$ MeV.

3.2 The $f_4(2220)$ Reexamined - What Is it Really?

The $f_4(2220)$ (formerly known as the $\xi(2220)$) state was discovered by the Mark III Collaboration [16] in 1983, in the decay $e^+e^- \rightarrow J/\psi \rightarrow \gamma f_4(2220) \rightarrow \gamma K^+K^-$ – see Figure 3.7. It attracted considerable attention because of its narrow width of approximately 30 MeV, which was thought to be too small for a conventional meson of that mass. Over the years this has led to speculation that it might be a Higgs boson [17], a bound state of coloured scalars [18], a four quark state [19, 20], a $\Lambda\bar{\Lambda}$ bound state [21], or a meson hybrid or a glueball [22], among others (we only reference early works on each suggestion).

The $f_4(2220)$ has since been seen by other experiments, the results of which are summarized in Table 3.4. The rather broad state seen by DM2 is unlikely to be the same state seen by the other experiments. The recent measurements by the BES Collaboration are of particular interest, because the previously unseen $\pi^+\pi^-$ and $p\bar{p}$ decay modes indicate a decay pattern that is roughly flavour-symmetric, in keeping with the glueball interpretation (see for example, the recent paper by Chao [23]). The $f_4(2220)$ has not been seen by $p\bar{p}$ experiments, but the limits set are not stringent enough to exclude the meson identification (for example see Barnes *et al.* [24]).

The intermediate state J/ψ and the final observed states indicate that the parity and charge conjugation quantum numbers of the $f_4(2220)$ are $^{++}$ and that its spin J must be even, although as can be seen from Table 3.4 the actual value of J is rather uncertain. The Particle Data Group [1] has tentatively identified the $f_4(2220)$ as the 3F_4 $s\bar{s}$ meson (hence its presence in Table 1.2), but notes that this needs confirmation.

In order to determine whether the $f_4(2220)$ is a high-spin meson or something new and much more interesting, we need theoretical predictions of the properties of the various options in order to make the identification. In this work we carefully examine the decays of the 3F_2 and 3F_4 $s\bar{s}$ mesons in order to see if the meson identification is

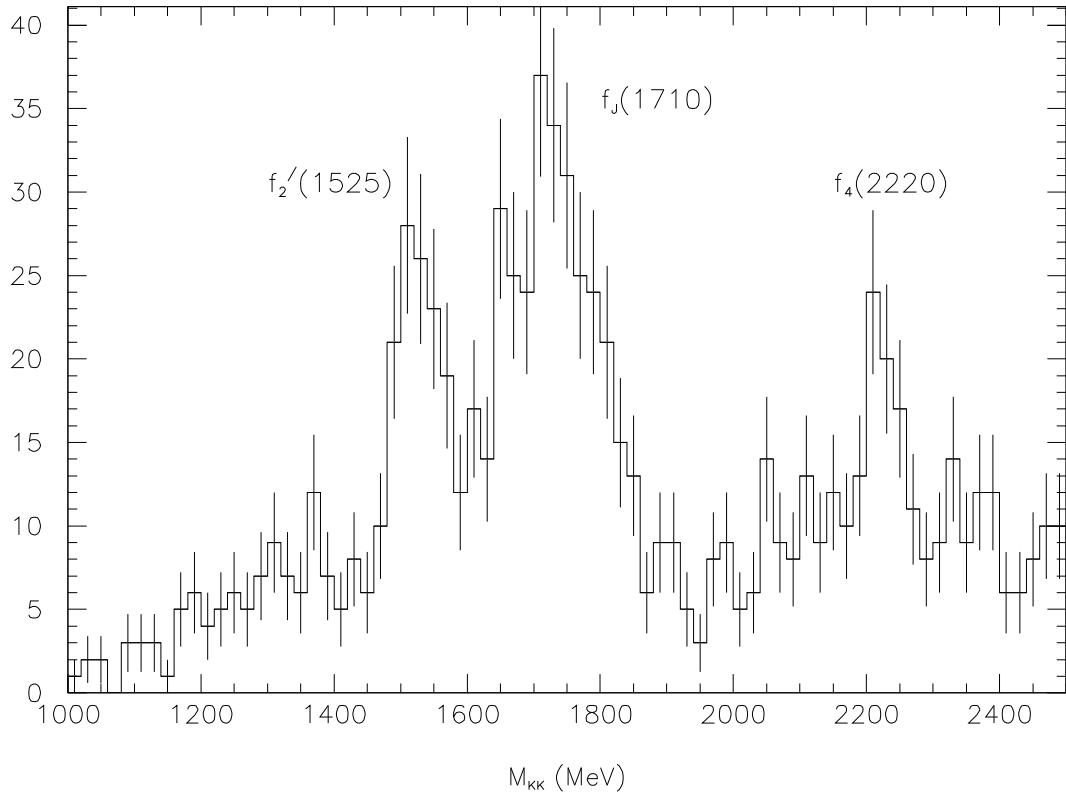


Figure 3.7: The original data from the discovery of the $f_4(2220)$ by the MARK III Collaboration [16]. The distribution of the K^+K^- invariant mass in $e^+e^- \rightarrow J/\psi \rightarrow \gamma K^+K^-$ is shown, revealing three resonances. The errors shown are purely statistical.

tenable. These are the best meson candidates because of their J^{PC} 's of 2^{++} and 4^{++} respectively, and because their masses have been predicted to lie in the right range (Godfrey and Isgur [4] calculated masses of 2240 MeV and 2200 MeV respectively).

The decay widths of these mesons have been calculated previously. The first was by Godfrey, Kokoski and Isgur [30] using the flux-tube breaking model (and somewhat different masses: 2270 MeV and 2210 MeV respectively). Despite the fact that one naïvely expects heavy mesons to be broad, since more phase space and decay channels lead to larger widths, they found the total widths to be approximately 60 MeV and 50 MeV respectively. Based on production rate arguments, they concluded that the $f_4(2220)$ was most likely to be the 3F_2 $s\bar{s}$ state. However, the analysis was not

Experiment	Process	Mass (MeV)	Width (MeV)	J
SLAC-SP-032 (Mark III) ^a	$e^+e^- \rightarrow J/\psi \rightarrow \gamma f_4(2220)$ $\hookrightarrow K^+K^-$ $\hookrightarrow K_S^0\bar{K}_S^0$	$2230 \pm 6 \pm 14$ $2232 \pm 7 \pm 7$	$26_{-16}^{+20} \pm 17$ $18_{-15}^{+23} \pm 10$	
(GAMS-2000, GAMS-4000) ^b	$\pi^-p \rightarrow f_4(2220) n$ $\hookrightarrow \eta\eta'$	2220 ± 10		≥ 2
SERP-E-147 (MIS) ^c	$\pi^-p \rightarrow f_4(2220) n$ $\hookrightarrow K_S^0\bar{K}_S^0$	2230 ± 20	80 ± 30	2
SLAC-E-135 (LASS) ^d	$K^-p \rightarrow f_4(2220) \Lambda$ $\hookrightarrow K^+K^-$	$2209_{-15}^{+17} \pm 10$	60_{-57}^{+107}	4
RPP Average ^e		2225 ± 6	38_{-13}^{+15}	4?
(DM2) ^f	$e^+e^- \rightarrow J/\psi \rightarrow \gamma ?$ $\hookrightarrow K_S^0\bar{K}_S^0$	2197 ± 17	201 ± 51	
(BES) ^g	$e^+e^- \rightarrow J/\psi \rightarrow \gamma f_4(2220)$ $\hookrightarrow K^+K^-$ $\hookrightarrow K_S^0\bar{K}_S^0$ $\hookrightarrow p\bar{p}$ $\hookrightarrow \pi^+\pi^-$	$2230_{-7}^{+6} \pm 12$ $2232_{-7}^{+8} \pm 15$ $2235 \pm 4 \pm 5$ $2235 \pm 4 \pm 6$	$20_{-15}^{+20} \pm 12$ $20_{-16}^{+25} \pm 10$ $15_{-9}^{+12} \pm 9$ $19_{-11}^{+13} \pm 12$	

Table 3.4: Summary of measurements of the $f_4(2220)$. The RPP average is for the first four entries in the table only; they feel that the $f_4(2220)$ still needs confirmation. In the case of the DM2 results, the resonance seen was not identified with the $f_4(2220)$, and so it is not included in the RPP average; the BES data is too recent.

^a Reference [16].

^b Reference [25].

^c Reference [26].

^d Reference [27].

^e Reference [1].

^f Reference [28].

^g Reference [29].

exhaustive in that it did not calculate the partial widths to all possible final states. In particular it made the assumption, which we will see to be incorrect, that the decays to an $L = 1$ meson and a K or η were small on the basis of phase space arguments alone.¹⁰

¹⁰In addition, they note that the decay to $K^*(892)\bar{K}^*(892)$ is dominated by the $1, D$ partial wave

In addition, Pakvasa, Suzuki and Tuan [20] have used Regge theory to estimate the partial width of the 3F_4 $s\bar{s}$ state decaying to two 1S_0 mesons as approximately 40 MeV, with the total width expected to be a few times larger. And finally, Ono, Pène and Schöberl [31] have used the 3P_0 model to calculate the partial width of the 3F_2 $s\bar{s}$ state (assuming a mass of 2200 MeV) decaying to 1S_0 and 3S_1 states to be 417 MeV (with the width to $K^*(892)\bar{K}^*(892)$ dominant at 348 MeV). In light of the new data, and these contradictory theoretical results, a new, complete calculation is required.

We have calculated the 3F_2 and 3F_4 $s\bar{s}$ meson decay widths using the six combinations of model, wavefunction, and phase space/normalization discussed in Section 3.1. In order to judge the reliability of the results, it is useful to examine how well our calculations do for similar mesons. We do not have any good candidates for the 3F_2 , but the $f_4(2050)$ and $K_4^*(2045)$ differ only in flavour from the 3F_4 $s\bar{s}$. Examining Figures 3.1, 3.3 and 3.5, we see that for the five decays in question, the choice of phase space/normalization makes a significant difference: RPSN tends to overestimate the partial widths, while KIPSN tends to underestimate them. For the $K_3^*(1780)$, which one would expect to behave similarly to the 3F_4 states (since both are ${}^3L_{L+1}$), the situation is unfortunately less clear. We can also examine the total width of the $f_4(2050)$ and $K_4^*(2045)$ states. In Tables 3.5 and 3.6 we give the partial widths for all significant, kinematically-allowed decays and their sums, in the 3P_0 model and with SHO wavefunctions only. It can be seen that once again the RPSN results are high, and the KIPSN results low. The main conclusion we can draw from these results is that the widths of the 3F_4 $s\bar{s}$ meson probably lie between the RPSN and KIPSN estimates but it is difficult to guess if they are closer to the lower or upper value.

Turning now to our results for the 3F_2 and 3F_4 $s\bar{s}$ mesons, in Tables 3.7 and 3.8 we

(using the S, L notation of Table 3.5). Unfortunately, $S = 1$ is forbidden by conservation of parity and charge conjugation, making the result for this decay questionable.

Decay $f_4(2050) \rightarrow$	Γ (MeV) from Experiment	Γ (MeV) from Models	
		3P_0	
		SHO	
		RPSN	KIPSN
$[\pi\pi]_{0,G}$	35.4 ± 3.8	123	25
$[\pi\pi(1300)]_{0,G}$		3.9	1.9
$[\pi a_1(1260)]_{1,F}$		18	7.5
$[\pi a_2(1320)]_{2,F}$		44	19
$[\pi\pi_2(1670)]_{2,D}$		2.1	1.8
$[\rho\rho]_{0,G}$		1.9	0.4
$[\rho\rho]_{2,D}$		159	33
$[\rho\rho]_{2,G}$		7.3	1.5
$[\eta\eta]_{0,G}$	0.4 ± 0.2	3.2	0.9
$[\eta\eta']_{0,G}$		1.0	0.3
$[\eta f_2(1270)]_{2,F}$		1.1	0.5
$[\omega\omega]_{2,D}$ }	54 ± 13 ^a	50	10
$[\omega\omega]_{2,G}$ }		2.0	0.4
$[K\bar{K}]_{0,G}$	$1.4^{+0.7}_{-0.4}$	5.4	1.6
$[K\bar{K}^*(892) + \text{c.c.}]_{1,G}$		2.7	0.8
$[K\bar{K}_1(1270) + \text{c.c.}]_{1,F}$		2.3	1.2
$[K^*(892)\bar{K}^*(892)]_{2,D}$		7.3	2.1
Total / $\sum_i \Gamma_i$	208 ± 13	435	109

Table 3.5: The calculated partial decay widths and total width of the $f_4(2050)$ meson. The available experimental results [1] are also shown. The model results are given for two combinations of decay model, wavefunctions, and phase space/normalization (specified in the second, third and fourth rows of the heading, respectively). We have calculated the partial widths of all kinematically-allowed, OZI-allowed, two-body strong decays, but only show those partial widths that are ≥ 1 MeV in at least one model. For this reason the total widths may not equal the sum of the partial widths shown. The subscripts on the decays refer to the S and L (see Appendix E) of the given partial wave – the L is in spectroscopic notation (S, P, D, F, G, H). We have used the meson mixings given in Appendix A.7 where applicable.

^a This number is the total for all partial waves.

give the partial widths for all significant, kinematically-allowed decays and their sums, for all six combinations of decay model, wavefunction, and phase space/normalization. For a degree of completeness, in Table 3.9 we also give the results for the other $L = 3$, spin-triplet $s\bar{s}$ meson, the 3F_3 , in the 3P_0 model and with SHO wavefunctions only.

Decay $K_4^*(2045) \rightarrow$	Γ (MeV) from Experiment	Γ (MeV) from Models	
		3P_0	SHO
		RPSN	KIPSN
$[K\pi]_{0,G}$	19.6 ± 3.8	55	13
$[K\rho]_{1,G}$		19	4.4
$[Kb_1(1235)]_{1,F}$		4.9	2.2
$[Ka_1(1260)]_{1,F}$		1.3	0.6
$[Ka_2(1320)]_{2,F}$		2.2	1.0
$[K^*(892)\pi]_{1,G}$		23	5.5
$[K^*(892)\rho]_{2,D}$	$18 \pm 10^{\text{a}}$	76	18
$[K^*(892)\rho]_{2,G}$		2.1	0.5
$[K_1(1270)\pi]_{1,F}$		1.6	0.7
$[K_1(1400)\pi]_{1,F}$		5.3	2.6
$[K_2^*(1430)\pi]_{2,F}$		5.2	2.6
$[K\eta']_{0,G}$		3.3	0.9
$[K\omega]_{1,G}$		6.0	1.4
$[K\phi]_{1,G}$		1.1	0.4
$[Kh_1(1170)]_{1,F}$		2.9	1.3
$[Kf_2(1270)]_{2,F}$		1.3	0.6
$[K^*(892)\eta]_{1,G}$		4.9	1.4
$[K^*(892)\omega]_{2,D}$		24	5.7
$[K^*(892)\phi]_{2,D}$	2.8 ± 1.4	3.2	1.0
Total / $\sum_i \Gamma_i$		198 \pm 30	247
			65

Table 3.6: The calculated partial decay widths and total width of the $K_4^*(2045)$ meson. The available experimental results [1] are also shown. For additional comments, see Table 3.5.

^a This number is actually for the final state $K^*(892)\pi\pi$, and is the total for all partial waves.

For the 3F_2 $s\bar{s}$ state the main decay modes are, in descending order, including charge conjugate pairs:

$$\begin{aligned}
& K_1(1270)\bar{K}, \ K_1(1270)\bar{K}^*(892), \ K^*(892)\bar{K}, \ K^*(892)\bar{K}^*(892), \\
& K_2^*(1430)\bar{K}, \ K\bar{K}, \ f_1(1510)\eta.
\end{aligned}$$

Decay	Γ (MeV) from Models of Meson Decay					
	3P_0		Flux-tube Breaking			
	SHO		SHO		RQM	
3F_2 $s\bar{s} \rightarrow$	RPSN	KIPSN	RPSN	KIPSN	RPSN	KIPSN
$[K\bar{K}]_{0,D}$	51	12	47	12	101	23
$[K_r\bar{K} + \text{c.c.}]_{0,D}$ ^a	2.9	1.5	0.9	0.5	25	12
$[K^*(892)\bar{K} + \text{c.c.}]_{1,D}$	108	26	107	26	165	38
$[K^*(1410)\bar{K} + \text{c.c.}]_{1,D}$	2.6	1.3	0.6	0.3	4.0	1.9
$[K_1(1270)\bar{K} + \text{c.c.}]_{1,P}$	445	187	449	194	1072	426
$[K_1(1270)\bar{K} + \text{c.c.}]_{1,F}$	25	11	27	12	41	16
$[K_1(1400)\bar{K} + \text{c.c.}]_{1,P}$	14	6.3	15	6.9	29	12
$[K_1(1400)\bar{K} + \text{c.c.}]_{1,F}$	0.8	0.4	1.0	0.4	~ 0	~ 0
$[K_2^*(1430)\bar{K} + \text{c.c.}]_{2,P}$	54	24	55	25	112	47
$[K_2^*(1430)\bar{K} + \text{c.c.}]_{2,F}$	9.6	4.3	10	4.7	22	9.1
$[K^*(892)\bar{K}^*(892)]_{0,D}$	24	5.7	24	5.9	39	8.9
$[K^*(892)\bar{K}^*(892)]_{2,D}$	14	3.3	14	3.4	23	5.1
$[K^*(892)\bar{K}^*(892)]_{2,G}$	48	12	52	13	83	19
$[K_1(1270)\bar{K}^*(892) + \text{c.c.}]_{1,P}$	99	40	102	42	209	79
$[K_1(1270)\bar{K}^*(892) + \text{c.c.}]_{1,F}$	0.5	0.2	0.6	0.2	1.1	0.4
$[K_1(1270)\bar{K}^*(892) + \text{c.c.}]_{2,P}$	33	13	34	14	70	26
$[K_1(1270)\bar{K}^*(892) + \text{c.c.}]_{2,F}$	0.8	0.3	0.9	0.4	1.8	0.7
$[\eta\eta]_{0,D}$	14	3.3	13	3.2	20	4.4
$[\eta'\eta]_{0,D}$	29	7.0	29	7.2	29	6.6
$[f_1(1510)\eta]_{1,P}$	45	22	46	24	92	43
$[f'_2(1525)\eta]_{2,P}$	14	6.9	14	7.3	29	14
$[\eta'\eta']_{0,D}$	6.6	1.6	6.7	1.7	4.9	1.1
$[\phi\phi]_{0,D}$	3.9	1.2	3.9	1.3	5.5	1.6
$[\phi\phi]_{2,D}$	2.2	0.7	2.3	0.7	3.1	0.9
$[\phi\phi]_{2,G}$	1.0	0.3	1.0	0.3	1.1	0.3
$\sum_i \Gamma_i$	1046	391	1058	406	2181	797

Table 3.7: The calculated partial decay widths and total width of the 3F_2 $s\bar{s}$ meson. We do not include a decay to $f_0(980)f_0(980)$ because we question its assignment as a 3P_0 meson. At a more likely mass for the 3P_0 $s\bar{s}$ meson, this decay is kinematically inaccessible. For additional comments, see Table 3.5.

^a K_r is our notation for the first radial excitation (2^1S_0) of the K .

Decay $^3F_4 \ s\bar{s} \rightarrow$	Γ (MeV) from Models of Meson Decay					
	3P_0		Flux-tube Breaking			
	SHO		SHO		RQM	
	RPSN	KIPSN	RPSN	KIPSN	RPSN	KIPSN
$[KK]_{0,G}$	118	29	125	31	62	14
$[K_r\bar{K} + \text{c.c.}]_{0,G}$	0.7	0.4	0.4	0.2	2.4	1.2
$[K^*(892)\bar{K} + \text{c.c.}]_{1,G}$	107	27	115	29	112	26
$[K^*(1410)\bar{K} + \text{c.c.}]_{1,G}$	1.7	0.9	0.8	0.4	5.0	2.4
$[K_1(1270)\bar{K} + \text{c.c.}]_{1,F}$	6.4	2.8	7.0	3.1	10	4.2
$[K_1(1270)\bar{K} + \text{c.c.}]_{1,H}$	1.3	0.6	1.4	0.6	3.7	1.5
$[K_1(1400)\bar{K} + \text{c.c.}]_{1,F}$	14	6.4	15	7.0	29	12
$[K_2^*(1430)\bar{K} + \text{c.c.}]_{2,F}$	15	7.0	16	7.7	35	15
$[K^*(892)\bar{K}^*(892)]_{0,G}$	2.1	0.5	2.3	0.6	4.3	1.0
$[K^*(892)\bar{K}^*(892)]_{2,D}$	181	44	184	46	312	72
$[K^*(892)\bar{K}^*(892)]_{2,G}$	8.2	2.0	8.9	2.2	17	3.9
$[\eta\eta]_{0,G}$	14	3.5	15	3.9	5.0	1.2
$[\eta'\eta]_{0,G}$	6.9	1.7	7.5	1.9	2.4	0.6
$[\phi\phi]_{2,D}$	20	6.6	21	7.1	31	9.5
$\sum_i \Gamma_i$	498	132	522	142	633	166

Table 3.8: The calculated partial decay widths and total width of the $^3F_4 \ s\bar{s}$ meson. For additional comments, see Tables 3.5 and 3.7.

It is clearly a mistake to neglect the decays to an $L = 1$ meson and a K or η ; by far the largest partial width is for the decay to $K_1(1270)\bar{K}$, and many of the other decays involving $L = 1$ mesons are significant. The results using RQM wavefunctions are surprisingly large – about double those using SHO wavefunctions. Turning to the results with SHO wavefunctions, we see that if we believe that the KIPSN results give a lower bound for the 3F_2 as well as the 3F_4 , we can expect a total width $\gtrsim 400$ MeV, in keeping with naïve expectations. Even if this width is too large by a factor of 2, the $f_4(2220)$ cannot be the $^3F_2 \ s\bar{s}$ meson. Indeed, the $^3F_2 \ s\bar{s}$ may well be too broad to be found experimentally.

For the $^3F_4 \ s\bar{s}$ state the main decay modes are, in descending order, including

Decay	Γ (MeV) from Models	
	3P_0	
	SHO	
${}^3F_3 \ s\bar{s} \rightarrow$	RPSN	KIPSN
$[K^*(892)K + \text{c.c.}]_{1,D}$	154	38
$[K^*(892)\bar{K} + \text{c.c.}]_{1,G}$	98	24
$[K^*(1410)\bar{K} + \text{c.c.}]_{1,D}$	2.5	1.3
$[K^*(1410)\bar{K} + \text{c.c.}]_{1,G}$	2.2	1.1
$[K_0^*(1430)\bar{K} + \text{c.c.}]_{0,F}$	5.3	2.4
$[K_1(1270)\bar{K} + \text{c.c.}]_{1,F}$	71	30
$[K_2^*(1430)\bar{K} + \text{c.c.}]_{2,P}$	305	137
$[K^*(892)\bar{K}^*(892)]_{2,D}$	66	16
$[K^*(892)\bar{K}^*(892)]_{2,G}$	27	6.6
$[K_1(1270)\bar{K}^*(892) + \text{c.c.}]_{2,P}$	157	63
$[f'_2(1525)\eta]_{2,P}$	73	37
$[\phi\phi]_{2,D}$	10	3.2
$\sum_i \Gamma_i$	974	360

Table 3.9: The calculated partial decay widths and total width of the ${}^3F_3 \ s\bar{s}$ meson. We do not include decays to $f_0(980)\eta$ or $f_0(980)\eta'$ because we question the assignment of the $f_0(980)$ as a 3P_0 meson. At a more likely mass for the ${}^3P_0 \ s\bar{s}$ meson, this decay is kinematically inaccessible. For additional comments, see Table 3.5.

charge conjugate pairs:

$$K^*(892)\bar{K}^*(892), \ K\bar{K}, \ K^*(892)\bar{K}, \ \phi\phi.$$

Note that the total width of the ${}^3F_4 \ s\bar{s}$ is quite a bit less than that of the ${}^3F_2 \ s\bar{s}$. This can be understood in terms of the orbital angular momentum between the mesons in the final state. Because of the higher spin of the 3F_4 , it tends to yield final states with higher orbital angular momentum in order to conserve angular momentum. These decays are then suppressed by the higher angular momentum barrier. Examining Table 3.7, we see that the lowest orbital angular momentum final states in ${}^3F_2 \ s\bar{s}$ decay are in P-waves. All of these decays are relatively broad but the decay to $K_1(1270)\bar{K}$ is the P-wave decay with the largest available phase space. In fact, one

could almost order the P-wave decays using phase space alone. The analogous decay of the ${}^3F_4\ s\bar{s}$ is in an F-wave and therefore is suppressed by a larger angular momentum barrier. The lowest angular momentum partial wave for ${}^3F_4\ s\bar{s}$ decays is a D-wave which, although it has the largest partial width of all ${}^3F_4\ s\bar{s}$ decays, is still smaller than the P-wave ${}^3F_2\ s\bar{s}$ decay.

Looking at the total width of the ${}^3F_4\ s\bar{s}$ state, if we accept that the true result lies between those obtained from RPSN and KIPSN, then we would expect the width to be $\gtrsim 140$ MeV and $\lesssim 600$ MeV. While this is not very specific, we are really interested in the lower bound, and whether this could be the $f_4(2220)$. It is possible to look at the behaviour of the similar $f_4(2050)$ and $K_4^*(2045)$ (and perhaps $K_3^*(1780)$) decays in selected model, wavefunction and phase space/normalization combinations. For example, in the 3P_0 model with SHO wavefunctions and RPSN, the decays to two 3S_1 mesons are well predicted, indicating that the largest partial width of the ${}^3F_4\ s\bar{s}$ (to $K^*(892)\bar{K}^*(892)$) may well be close to the calculated value. On the other hand, the partial widths to two 1S_0 mesons may be less than predicted, and to a 1S_0 and a 3S_1 slightly more. Based on this, we think it possible, but unlikely, that the calculated ${}^3F_4\ s\bar{s}$ width is high by a factor of 2. Indeed, we would expect the actual width to be higher, i.e. > 140 MeV. Unfortunately, the uncertainties associated with the models we are using make it impossible to rule out the identification of the $f_4(2220)$ as the ${}^3F_4\ s\bar{s}$ meson with any surety; however, we feel it is unlikely.

Aside from the total width of the ${}^3F_4\ s\bar{s}$, the roughly flavour symmetric nature of the $f_4(2220)$ decays observed at BES suggest that it is not an $s\bar{s}$ meson, since production of $\pi\pi$ and $p\bar{p}$ would be OZI-suppressed. We thus propose a second explanation of what is being observed in this mass region – that two different hadron states are present: a narrow state produced in J/ψ radiative decay and a broader state seen in hadron beam experiments. The broader state would be identified with the ${}^3F_4\ s\bar{s}$ state. The measured width is consistent with our predictions and the LASS Collabora-

ration [27] shows evidence that its quantum numbers are $J^{PC} = 4^{++}$. We would then identify the narrow hadron state observed in the gluon rich J/ψ radiative decays as a glueball [23]. The narrow state is not seen in hadron beam production because it is narrow, is produced weakly in these experiments through intermediate gluons, and is hidden by the $s\bar{s}$ state. Conversely, the broader state is not seen in J/ψ radiative decays because this mode preferentially produces states with a high glue content. Crucial to this explanation is the experimental verification of the BES results on the flavour symmetric couplings of the state produced in J/ψ radiative decay and the observation of other decay modes for the broader state (primarily $K^*(892)\bar{K}^*(892)$ and $K^*(892)\bar{K}$) in addition to the theoretical verification that the predicted tensor glueball is as narrow as the observed width.

We conclude that the $f_4(2220)$ cannot be the 3F_2 $s\bar{s}$ meson, and that taking all of the data into account, it is unlikely to be the 3F_4 $s\bar{s}$ meson alone. Instead we suggest that the broad state seen in hadron beam experiments is the 3F_4 $s\bar{s}$ meson, and the narrow state seen in J/ψ radiative decay is a glueball. Further experimental data is needed to finally identify the $f_4(2220)$.

3.3 Constraining the K_1 Mixing Angle

As discussed in Appendix A.7, the 1P_1 and 3P_1 strange mesons mix to produce the physical states $K_1(1270)$ and $K_1(1400)$. A possible source of the mixing can be seen in the spin-orbit portion of the Hamiltonian of Godfrey and Isgur's relativized quark model [4], described in Section 1.2.2. We can rewrite Eq. 1.6 as

$$H_{q\bar{q}}^{\text{SO}} = H_{q\bar{q}}^{\text{SO}+} + H_{q\bar{q}}^{\text{SO}-} \quad (3.1)$$

where

$$\begin{aligned} H_{q\bar{q}}^{\text{SO}+} &= \left[-\frac{\alpha_s}{2r^3} \left(\frac{1}{m_q} + \frac{1}{m_{\bar{q}}} \right)^2 \vec{F}_q \cdot \vec{F}_{\bar{q}} - \frac{1}{4r} \frac{\partial H_{q\bar{q}}^{\text{conf}}}{\partial r} \left(\frac{1}{m_q^2} + \frac{1}{m_{\bar{q}}^2} \right) \right] (\vec{S}_q + \vec{S}_{\bar{q}}) \cdot \vec{L}, \\ H_{q\bar{q}}^{\text{SO}-} &= \left(-\frac{\alpha_s}{2r^3} \vec{F}_q \cdot \vec{F}_{\bar{q}} - \frac{1}{4r} \frac{\partial H_{q\bar{q}}^{\text{conf}}}{\partial r} \right) \left(\frac{1}{m_q^2} - \frac{1}{m_{\bar{q}}^2} \right) (\vec{S}_q - \vec{S}_{\bar{q}}) \cdot \vec{L}. \end{aligned} \quad (3.2)$$

Using this quark model Hamiltonian, the mass formulae for the P-wave mesons are

$$\begin{aligned} M(^3P_2) &= M_0 + \frac{1}{4} \langle H_{q\bar{q}}^{\text{cont}} \rangle - \frac{1}{10} \langle H_{q\bar{q}}^{\text{ten}} \rangle + \langle H_{q\bar{q}}^{\text{SO}+} \rangle, \\ \begin{pmatrix} M(^3P_1) \\ M(^1P_1) \end{pmatrix} &= \begin{pmatrix} M_0 + \frac{1}{4} \langle H_{q\bar{q}}^{\text{cont}} \rangle + \frac{1}{2} \langle H_{q\bar{q}}^{\text{ten}} \rangle - \langle H_{q\bar{q}}^{\text{SO}+} \rangle & \sqrt{2} \langle H_{q\bar{q}}^{\text{SO}-} \rangle \\ \sqrt{2} \langle H_{q\bar{q}}^{\text{SO}-} \rangle & M_0 - \frac{3}{4} \langle H_{q\bar{q}}^{\text{cont}} \rangle \end{pmatrix} \begin{pmatrix} ^3P_1 \\ ^1P_1 \end{pmatrix}, \\ M(^3P_0) &= M_0 + \frac{1}{4} \langle H_{q\bar{q}}^{\text{cont}} \rangle - \langle H_{q\bar{q}}^{\text{ten}} \rangle - 2 \langle H_{q\bar{q}}^{\text{SO}+} \rangle, \end{aligned} \quad (3.3)$$

where the $\langle H_{q\bar{q}}^i \rangle$ are the expectation values of the spatial parts of the various terms of the Hamiltonian, M_0 is the center of mass of the multiplet, and we have adopted a phase convention corresponding to the order of coupling $\vec{L} \times \vec{S}_q \times \vec{S}_{\bar{q}}$. It can be seen that $H_{q\bar{q}}^{\text{SO}-}$ leads to mixing between the 1P_1 and 3P_1 states. However, $H_{q\bar{q}}^{\text{SO}-}$ is non-zero only if $m_q \neq m_{\bar{q}}$, so the strange mesons are the lightest states where this mixing can occur.

If we use Eq. A.5 to describe the mixing, we find that to diagonalize the 1P_1 – 3P_1 Hamiltonian we must have

$$\tan(2\theta_K) = -\frac{2\sqrt{2} \langle H_{q\bar{q}}^{\text{SO}-} \rangle}{\langle H_{q\bar{q}}^{\text{cont}} \rangle + \frac{1}{2} \langle H_{q\bar{q}}^{\text{ten}} \rangle - \langle H_{q\bar{q}}^{\text{SO}+} \rangle}, \quad (3.4)$$

where θ_K is the K_1 mixing angle. In this particular quark model, the expectation values of the spatial parts of the various terms for strange mesons are $M_0 = 1378$ MeV, $\langle H_{q\bar{q}}^{\text{cont}} \rangle = 33$ MeV, $\langle H_{q\bar{q}}^{\text{ten}} \rangle = 56$ MeV, $\langle H_{q\bar{q}}^{\text{SO}+} \rangle = 47$ MeV and $\langle H_{q\bar{q}}^{\text{SO}-} \rangle = -1$ MeV

[32]. This gives rise to a prediction of $\theta_K = 6^\circ$.

In this section we compare the predictions of the 3P_0 and flux-tube breaking models of meson decay to experimental data for five decay widths and two ratios of D to S amplitudes¹¹, in order to determine θ_K . This mixing angle is of interest both for its own sake, and for what it can tell us about the quark model Hamiltonian.

The $K_1(1270)$ and $K_1(1400)$ can both decay to $K\rho$ and $K^*(892)\pi$; the $K_1(1400)$ can also decay to $K\omega$. All of the decays occur in the partial waves 1, S and 1, D (in S, L notation). Although decays to other final states are observed they lie below threshold and proceed through the tails of the Breit-Wigner resonances making the calculations less reliable. In addition to these five decay widths, there are also experimental results available for the ratio of D to S amplitudes for both $K_1(1270)$ and $K_1(1400)$ decaying to $K^*(892)\pi$.

We have calculated these seven quantities using the six combinations of model, wavefunction, and phase space/normalization selected in Section 3.1. The $K_1(1270)$ quantities are plotted as a function of the K_1 mixing angle in Figure 3.8, and the $K_1(1400)$ quantities are plotted in Figure 3.9 – the experimental results are also shown in both figures.

In order to determine the best fit values of θ_K , we have carried out a least squares fit for each of the six combinations of decay model, wavefunction, and phase space/normalization. The best fit values of θ_K and their corresponding χ^2/dof are shown in Table 3.10, as are the resulting values of each of the seven quantities being considered, and their experimental values. Examining the results, we see that as usual, the values of χ^2/dof are high, but not as high as were obtained in the 28-decay fits of Section 3.1. This is not unexpected, since the similar decay $b_1(1235) \rightarrow \omega\pi$ was described reasonably well in those fits. It is also clear that the SHO wavefunctions

¹¹By “ratio of D to S amplitudes” we mean the ratio of the $L = 2$ partial wave amplitude for a decay to the $L = 0$ partial wave amplitude for the same decay.

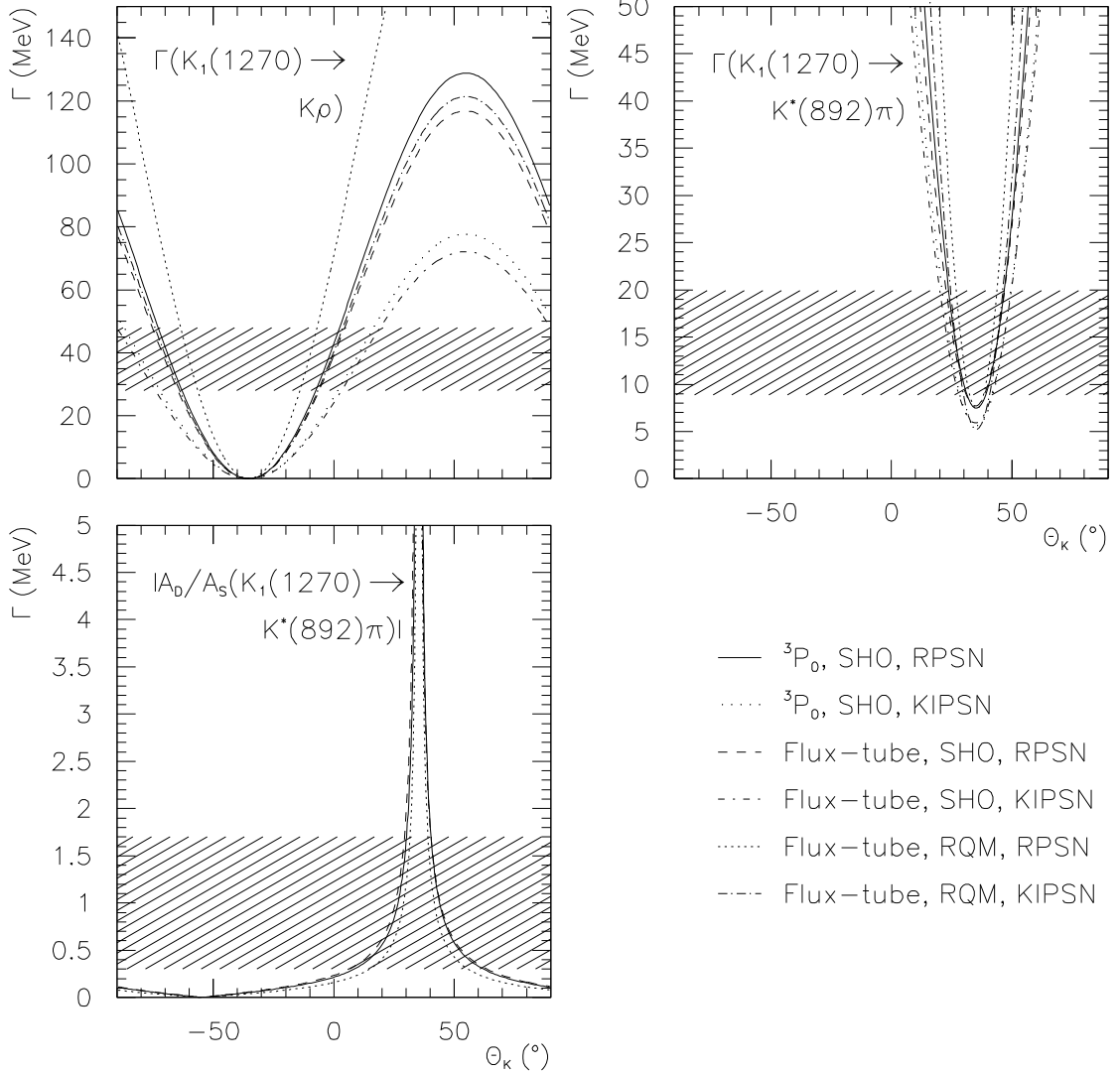


Figure 3.8: Graphs of the $K_1(1270)$ partial decay widths and ratio of D to S amplitudes considered in this work, vs. the mixing angle θ_K . The shaded regions are the $1-\sigma$ limits on the experimental measurements of the quantities [1]. In the key the labels refer to the meson decay model, the wavefunctions used, and the type of phase space/normalization used. Only three curves are shown for $|A_D/A_S(K_1(1270) \rightarrow K^*(892)\pi)|$, because the differences between RPSN and KIPSN cancel in the ratio of amplitudes, making the RPSN and KIPSN curves for the same model and wavefunctions identical.

do better than the RQM, and in terms of phase space/normalization, KIPSN does better than the RPSN.

Quantity	Value from Experiment	Value Calculated from Models of Meson Decay					
		3P_0		Flux-tube Breaking			
		SHO		SHO		RQM	
		RPSN	KIPSN	RPSN	KIPSN	RPSN	KIPSN
Fitted mixing angle θ_K		$48.4 \pm 1.1^\circ$	$45.2_{-1.3}^{+1.4}{}^\circ$	$46.8_{-1.0}^{+1.1}{}^\circ$	$44.2 \pm 1.3^\circ$	$55.4_{-0.8}^{+0.7}{}^\circ$	$50.6_{-1.2}^{+1.3}{}^\circ$
χ^2/dof		38.9	5.3	26.0	3.3	231	51.2
$\Gamma(K_1(1270) \rightarrow K\rho)$	38 ± 10	127	76	115	70	213	121
$\Gamma(K_1(1270) \rightarrow K^*(892)\pi)$	14.4 ± 5.5	24	13	20	12	76	34
$ A_D/A_S(K_1(1270) \rightarrow K^*(892)\pi) $	1.0 ± 0.7	0.65	0.86	0.77	0.99	0.31	0.41
$\Gamma(K_1(1400) \rightarrow K\rho)$	5.2 ± 5.2	15	12	17	12	10	7.0
$\Gamma(K_1(1400) \rightarrow K^*(892)\pi)$	164 ± 16	350	221	306	197	653	402
$ A_D/A_S(K_1(1400) \rightarrow K^*(892)\pi) $	0.04 ± 0.01	0.071	0.054	0.069	0.053	0.080	0.061
$\Gamma(K_1(1400) \rightarrow K\omega)$	1.7 ± 1.7	4.3	3.5	5.0	3.8	2.7	2.0

Table 3.10: The partial decay widths and ratios of D to S amplitudes used in our fits of the $K_1(1270)$ and $K_1(1400)$ mixing angle θ_K . The experimental values [1] are shown, as are the model results for the six combinations of decay model, wavefunctions, and phase space/normalization (specified in the second, third and fourth rows of the heading, respectively). For each combination we also give the fitted value of θ_K , and the corresponding χ^2/dof . The partial widths are given in units of MeV. All errors shown are $1-\sigma$.

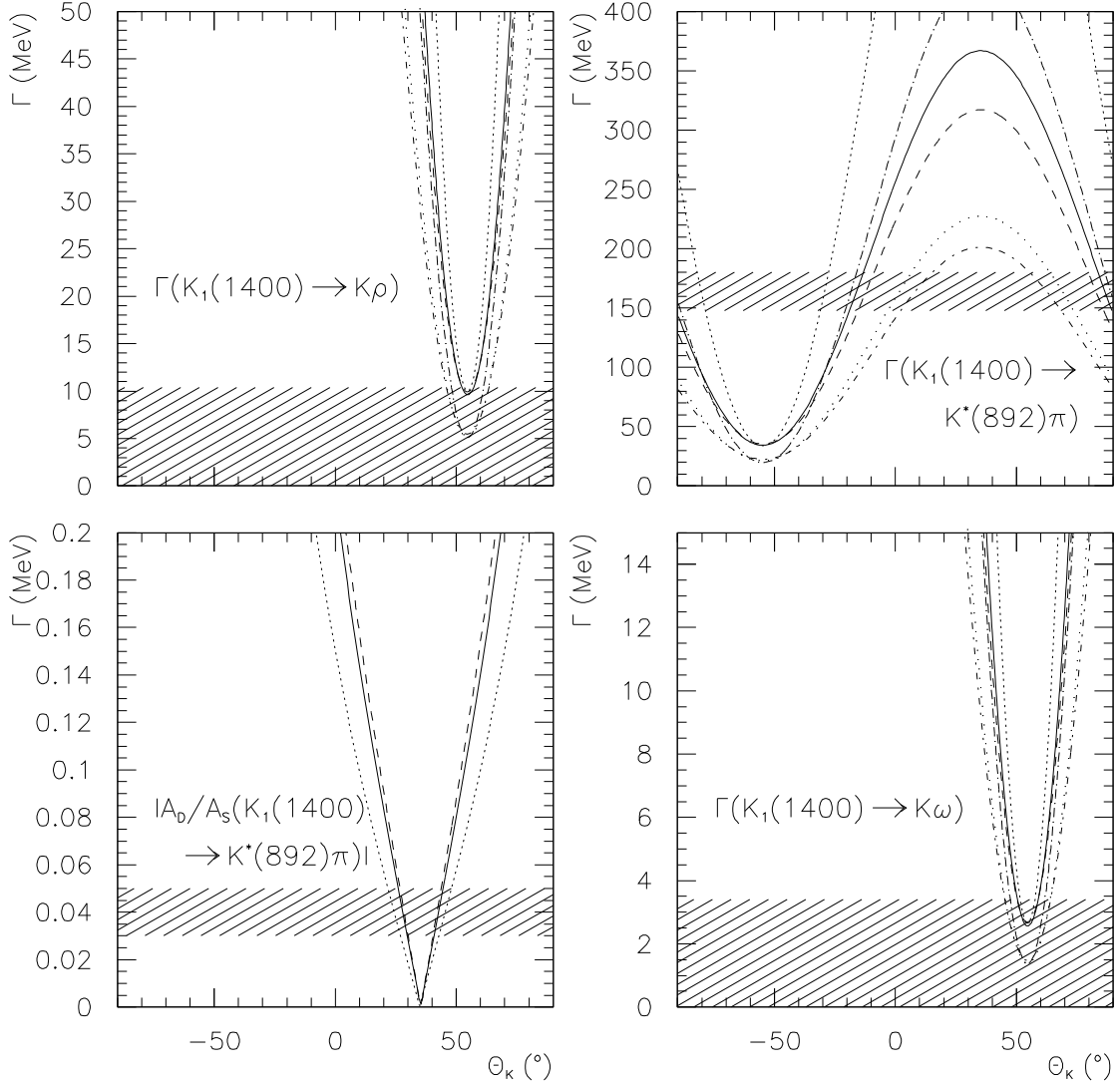


Figure 3.9: Graphs of the $K_1(1400)$ partial decay widths and ratio of D to S amplitudes considered in this work, vs. the mixing angle θ_K . See Figure 3.8 for the explanation of the line labels and additional notes.

The resulting values of θ_K are all fairly similar, falling in the range $44 - 56^\circ$. The lowest values of χ^2/dof occur for fits near 44° , and so we take that as our approximate result. What can this tell us about the quark model Hamiltonian? A mixing angle of 44° implies $\langle H_{q\bar{q}}^{SO-} \rangle = -142$ MeV, rather different from the quark model value. However, the value of $\langle H_{q\bar{q}}^{SO-} \rangle$ is very sensitive to the angle in this region

(e.g. $\theta_K = 41^\circ$ implies $\langle H_{q\bar{q}}^{SO-} \rangle = -35$ MeV, while $\theta_K = 45^\circ$ implies $\langle H_{q\bar{q}}^{SO-} \rangle = -\infty$), so the only conclusion we can really draw is that the quark model value is very low, *if* $\langle H_{q\bar{q}}^{SO-} \rangle$ is responsible for all of the mixing. We cannot rule out the possibility that some other interaction is partly responsible for the mixing, such as mixing via common decay channels.

To consider the SO Hamiltonian further, define $\bar{m} = \frac{1}{2}(m_q + m_{\bar{q}})$ and $\Delta = (m_{\bar{q}} - m_q)$. Next expand $1/m_q = 1/\bar{m} + \Delta/(2\bar{m}^2) + \dots$ and $1/m_{\bar{q}} = 1/\bar{m} - \Delta/(2\bar{m}^2) + \dots$ to first order in Δ/\bar{m} (each of these truncated results has less than an 11% error for the quark masses we used). In terms of these, the contributions to the spin-orbit Hamiltonian become

$$\begin{aligned} H_{q\bar{q}}^{SO+} &\simeq \left(-\frac{2\alpha_s}{\bar{m}^2 r^3} \vec{F}_q \cdot \vec{F}_{\bar{q}} - \frac{1}{2\bar{m}^2 r} \frac{\partial H_{q\bar{q}}^{\text{conf}}}{\partial r} \right) (\vec{S}_q + \vec{S}_{\bar{q}}) \cdot \vec{L}, \\ H_{q\bar{q}}^{SO-} &\simeq \frac{\Delta}{\bar{m}} \left(-\frac{\alpha_s}{\bar{m}^2 r^3} \vec{F}_q \cdot \vec{F}_{\bar{q}} - \frac{1}{2\bar{m}^2 r} \frac{\partial H_{q\bar{q}}^{\text{conf}}}{\partial r} \right) (\vec{S}_q - \vec{S}_{\bar{q}}) \cdot \vec{L}. \end{aligned} \quad (3.5)$$

The $\langle (\vec{S}_q \pm \vec{S}_{\bar{q}}) \cdot \vec{L} \rangle$ factors are roughly the same size, and the Δ/\bar{m} term is not too far from 1 (it is $\geq \frac{1}{2}$ for the quark masses we used), so the factors in the large parentheses contribute at the same order of magnitude. Note that the contributions from the Thomas precession term are equal, but those from the colour magnetic term differ by a factor of 2. The model gives a large $\langle H_{q\bar{q}}^{SO+} \rangle$ of 47 MeV, but a small $\langle H_{q\bar{q}}^{SO-} \rangle$ of -1 MeV arising from a delicate cancellation of the colour magnetic and Thomas precession terms. It is thus conceivable that a small change in the model could lead to a substantially larger $\langle H_{q\bar{q}}^{SO-} \rangle$, so we are unable to draw any conclusions about whether the mixing is largely due to another mechanism, or the quark model Hamiltonian just needs some retuning.

Chapter 4

Effects of Final State Interactions

4.1 Introduction to Final State Interactions

Final state interactions (FSI's) refer to additional interactions between particles in the final state that are not included in the basic interaction.¹ For example, in Chapter 5, we consider the basic interaction $\gamma\gamma \rightarrow \pi^+\pi^-$, which proceeds through a scalar QED vertex. However, there will also be a QCD interaction between the final state pions. In Chapter 5, we attempt to calculate the effects of the FSI for this process. In this chapter, we introduce the techniques that we will apply to the problem of FSI's [33].

The techniques involve nonrelativistic quantum mechanics (including the Schrödinger equation), corrected to include relativistic phase space where possible. The basic interaction may still be calculated relativistically: e.g. $\gamma\gamma \rightarrow \pi\pi$. This mixture of nonrelativistic and relativistic elements is typical of the quark model.

¹The techniques introduced here could also be used to describe additional interactions between particles in the initial state. However, since most physically interesting problems involve FSI's, the term "final state interactions" has become the name of choice.

4.2 Solving the Schrödinger Equation with the FSI Potential

Our first step in calculating the effects of an FSI is to find the wavefunction describing the state of the final state particles due to the presence of the FSI only. We assume that the FSI can be described by a potential between the final state particles, and that the wavefunction can be found by solving the Schrödinger equation.

The relative wavefunction for two bodies in a potential that only depends on their relative position $\vec{r} \equiv \vec{r}_1 - \vec{r}_2$ can be found from the Schrödinger equation for a central-force potential

$$\left[\nabla_{\vec{r}}^2 - 2\mu V(r) + k^2 \right] \psi(\vec{r}) = 0 \quad (4.1)$$

where μ is the reduced mass of the particles, $V(r)$ is the potential between the two particles and k is the relative momentum between the particles in the absence of a potential, given by $k^2 \equiv 2\mu E$, where E is the kinetic energy of the system. Recall that we are using the particle physics convention that $c \equiv \hbar \equiv 1$.

If we now select a solution with a particular orbital angular momentum and set $\psi_{lm}(\vec{r}) \equiv R_l(r) Y_{lm}(\Omega_r)$, then $R_l(r)$ satisfies the radial equation

$$\left[\frac{1}{r} \frac{d^2}{dr^2} r - \frac{l(l+1)}{r^2} - 2\mu V(r) + k^2 \right] R_l(r) = 0. \quad (4.2)$$

If we further set $R_l(r) \equiv y_l(r)/r$, then $y_l(r)$ satisfies the equivalent radial equation

$$\left[\frac{d^2}{dr^2} - \frac{l(l+1)}{r^2} - 2\mu V(r) + k^2 \right] y_l(r) = 0. \quad (4.3)$$

The solution of Eq. 4.1 for $V(r) = 0$ is just a plane wave, which can be broken

up into its partial waves,

$$\phi_{\vec{k}}(\vec{r}) \equiv e^{i\vec{k} \cdot \vec{r}} = 4\pi \sum_{l=0}^{\infty} \sum_{m_l=-l}^l i^l j_l(kr) Y_{lm_l}^*(\Omega_k) Y_{lm_l}(\Omega_r), \quad (4.4)$$

where $j_l(kr)$ is a spherical Bessel function and \vec{k} gives the direction of the incident particle. The equivalent solution of Eq. 4.2 for $V(r) = 0$ (picking the only particular solution that is regular at the origin) is

$$R_l(r) = j_l(kr) \xrightarrow{kr \rightarrow \infty} \frac{1}{kr} \sin(kr - \frac{1}{2}l\pi). \quad (4.5)$$

For the case with a potential, the stationary scattering waves $\psi_{\vec{k}}^{\pm}(\vec{r})$ are solutions of Eq. 4.1. Their asymptotic forms consist of the incoming plane wave, and either an outgoing (+) or incoming (−) spherical wave. We will be interested in $\psi_{\vec{k}}^-(\vec{r})$ because it will be describing the final state, and hence must be propagated backwards in time as an incoming spherical wave to be projected onto the initial state plane waves at an equal time. In nonrelativistic collision theory [34] it is defined to have the following asymptotic form

$$\psi_{\vec{k}}^-(\vec{r}) \xrightarrow{r \rightarrow \infty} e^{i\vec{k} \cdot \vec{r}} + f_{\vec{k}}^-(\Omega_r) \frac{e^{-ikr}}{r} \quad (4.6)$$

where $f_{\vec{k}}^-(\Omega_r)$ is called the scattering amplitude and describes the effect of the scattering.

By symmetry, $\psi_{\vec{k}}^-(\vec{r})$ and $f_{\vec{k}}^-(\Omega_r)$ will be symmetric about the incident axis. It is then reasonable to choose to set the incident axis along \hat{z} (i.e. $\vec{k} = k\hat{z}$), so that neither function is dependent on ϕ_r . We can then make the following expansions in terms of Legendre polynomials

$$\psi_{\vec{k}}^-(r, \theta_r) = \sum_{l=0}^{\infty} \frac{y_l(r)}{r} P_l(\cos\theta_r),$$

$$f_{\vec{k}}^-(\theta_r) = \sum_{l=0}^{\infty} f_l^- P_l(\cos\theta_r). \quad (4.7)$$

where $y_l(r)$ is a regular solution of the equivalent radial equation (Eq. 4.3), and has the following (un-normalized) asymptotic form²

$$y_l(r) \xrightarrow{r \rightarrow \infty} a_l \sin(kr - \frac{1}{2}l\pi + \delta_l). \quad (4.8)$$

We can then match the two asymptotic forms of $\psi_{\vec{k}}^-(r, \theta_r)$ to obtain a_l and f_l^- . Then applying the spherical harmonic addition theorem to the Legendre polynomial gives for the stationary scattering wave (with incoming spherical wave) solution of Eq. 4.1

$$\psi_{\vec{k}}^-(\vec{r}) = 4\pi \sum_{l=0}^{\infty} \sum_{m_l=-l}^l i^l e^{-i\delta_l} u_l(k, r) Y_{lm_l}^*(\Omega_k) Y_{lm_l}(\Omega_r) \quad (4.9)$$

where $u_l(k, r)$ is the regular solution of Eq. 4.2 with asymptotic form

$$u_l(k, r) \xrightarrow{r \rightarrow \infty} \frac{1}{kr} \sin(kr - \frac{1}{2}l\pi + \delta_l). \quad (4.10)$$

4.3 The Fermi Approximation

The simplest way to perform a correction due to FSI's is to use the Fermi approximation [35]. We assume that the FSI interaction is very short range, and hence that only the value at the origin of the relative wavefunction of the final state particles is significant. Since the wavefunction enters into the amplitude, the S-wave cross-section would be enhanced by a factor of $|u_0(k, 0)/j_0(0)|^2 = |u_0(k, 0)|^2$, and the cross-sections of other partial waves would be unaffected.

²We make the usual assumptions about the potential: that it is analytic in the vicinity of the origin, that $\lim_{r \rightarrow 0} r^2 V(r) = 0$ and that $\lim_{r \rightarrow \infty} r V(r) = 0$.

4.4 Applying FSI's to the Flux-tube Breaking Model of Meson Decay

Geiger and Swanson [14] have applied FSI's to the flux-tube breaking model of meson decay. Although we do not apply their methodology in this work, we give the details here for completeness and because: it connects the two topics of this thesis (meson decay and FSI's), we are aware of no *detailed* published discussion of the method, and our derivation includes factors neglected by Geiger and Swanson.

Recognizing that the last exponential function of Eq. 2.23 is the wavefunction between the final state particles in the absence of an FSI potential (Eq. 4.4), Geiger and Swanson replace it with the wavefunction in the presence of such a potential (Eq. 4.9). By doing so they are using a final state in which the FSI effects are included, instead of simple plane waves in which the effects are ignored. This should give a final result that includes the FSI effects.

Let us first examine the partial wave amplitudes from the flux-tube breaking model in the absence of FSI's. In Section 2.4, we used the Jacob-Wick formula to convert to partial-wave amplitudes (see Appendix E) – here we use the recoupling calculation because we have a need for the $\int d\Omega Y_{LM_L}^*(\Omega)$ integral. This gives us, from Eqs. 2.7 and 2.23, using Eqs. 2.28 and E.4

$$\begin{aligned}
M^{SL}(P) = & \gamma_0 \sqrt{8E_A E_B E_C} \sum_{\substack{M_{L_A}, M_{S_A}, M_{L_B}, M_{S_B}, M_{J_B}, \\ M_{L_C}, M_{S_C}, M_{J_C}, M_L, M_S, m}} \langle LM_L S M_S | J_A M_{J_A} \rangle \\
& \times \langle J_B M_{J_B} J_C M_{J_C} | S M_S \rangle \langle L_A M_{L_A} S_A M_{S_A} | J_A (M_{J_B} + M_{J_C}) \rangle \\
& \times \langle L_B M_{L_B} S_B M_{S_B} | J_B M_{J_B} \rangle \langle L_C M_{L_C} S_C M_{S_C} | J_C M_{J_C} \rangle \langle 1m 1-m | 00 \rangle \\
& \times \langle \chi_{S_B M_{S_B}}^{14} \chi_{S_C M_{S_C}}^{32} | \chi_{S_A M_{S_A}}^{12} \chi_{1-m}^{34} \rangle \left[\langle \phi_B^{14} \phi_C^{32} | \phi_A^{12} \phi_0^{34} \rangle I^{\text{FSI}}(P, m_1, m_2, m_3) \right. \\
& \left. + (-1)^{L_A + L_B + L_C + S_A + S_B + S_C} \langle \phi_B^{32} \phi_C^{14} | \phi_A^{12} \phi_0^{34} \rangle I^{\text{FSI}}(P, m_2, m_1, m_3) \right] \quad (4.11)
\end{aligned}$$

where

$$\begin{aligned}
I^{\text{FSI}}(P, m_1, m_2, m_3) = & -\frac{8}{(2\pi)^{\frac{3}{2}}} \int d^3\vec{r} \int d^3\vec{w} \ \psi_{n_B L_B M_{L_B}}^*(-\vec{w} - \vec{r}) \ \psi_{n_C L_C M_{L_C}}^*(\vec{w} - \vec{r}) \\
& \times e^{-\frac{1}{2}bw_{\min}^2} \int d\Omega_P \ Y_{LM}^*(\Omega_P) \ \mathcal{Y}_1^m \left(\left[(\vec{P} + i\vec{\nabla}_{\vec{r}_A}) \psi_{n_A L_A M_{L_A}}(\vec{r}_A) \right]_{\vec{r}_A=-2\vec{r}} \right) \\
& \times e^{i\vec{P} \cdot (m_+ \vec{r} + m_- \vec{w})}.
\end{aligned} \tag{4.12}$$

Note that in evaluating $M^{SL}(P)$ we can pick any value of M_{J_A} ; alternatively, we could sum over M_{J_A} and divide by $(2J_A + 1)$, on the right side.

Next, set

$$\vec{P} e^{i\vec{P} \cdot (m_+ \vec{r} + m_- \vec{w})} = \left[-\frac{i}{m_+} \vec{\nabla}_{\vec{r}_{BC}} e^{i\vec{P} \cdot (m_+ \vec{r}_{BC} + m_- \vec{w})} \right]_{\vec{r}_{BC}=\vec{r}}, \tag{4.13}$$

then use an alternate form of Eq. 4.4 to set

$$e^{i\vec{P} \cdot (m_+ \vec{r}_{BC} + m_- \vec{w})} = 4\pi \sum_{l=0}^{\infty} \sum_{m_l=-l}^l i^l j_l(Ps) Y_{lm_l}(\Omega_P) Y_{lm_l}^*(\Omega_s), \tag{4.14}$$

where $\vec{s} = m_+ \vec{r}_{BC} + m_- \vec{w}$, and finally, apply the orthogonality of spherical harmonics to obtain

$$\begin{aligned}
I^{\text{FSI}}(P, m_1, m_2, m_3) = & -\frac{8}{(2\pi)^{\frac{3}{2}}} \int d^3\vec{r} \int d^3\vec{w} \ \psi_{n_B L_B M_{L_B}}^*(-\vec{w} - \vec{r}) \ \psi_{n_C L_C M_{L_C}}^*(\vec{w} - \vec{r}) \\
& \times \mathcal{Y}_1^m \left(\left[\left(-\frac{i}{m_+} \vec{\nabla}_{\vec{r}_{BC}} + i\vec{\nabla}_{\vec{r}_A} \right) \psi_{n_A L_A M_{L_A}}(\vec{r}_A) \ \psi_{(BC)LM_L}^*(\vec{r}_{BC}, \vec{w}) \right]_{\vec{r}_A=-2\vec{r}, \vec{r}_{BC}=\vec{r}} \right) \\
& \times e^{-\frac{1}{2}bw_{\min}^2}
\end{aligned} \tag{4.15}$$

where, in the absence of FSI's,

$$\psi_{(BC)LM_L}(\vec{r}_{BC}, \vec{w}) = 4\pi i^{-L} j_L(Ps) Y_{LM_L}(\Omega_s). \tag{4.16}$$

Eq. 2.26 can be used to break $Y_{LM}(\Omega_s)$ up into spherical harmonics with arguments $\Omega_{\vec{r}_{BC}}$ and $\Omega_{\vec{w}}$ and of course, s is given by

$$s = \sqrt{m_+^2 r_{BC}^2 + m_-^2 w^2 + 2m_+ m_- r_{BC} w \cos \theta} \quad (4.17)$$

where θ is the angle between \vec{r}_{BC} and \vec{w} .

The above is just another way of expressing the flux-tube breaking model of meson decay of Section 2.3. However, we can include the effects of FSI's by replacing the plane wave $e^{i\vec{P} \cdot (m_+ \vec{r}_{BC} + m_- \vec{w})}$ with $\psi_{\vec{k}}^-(\vec{r})$ (Eq. 4.9), instead of just expanding it with Eq. 4.4. We then get, instead of Eq. 4.16,³

$$\psi_{(BC)LM_L}(\vec{r}_{BC}, \vec{w}) = 4\pi i^{-L} e^{i\delta_L} u_L(P, s) Y_{LM_L}(\Omega_s). \quad (4.18)$$

In the absence of an FSI potential, $\delta_L \Rightarrow 0$, $u_L(P, s) \Rightarrow j_L(Ps)$, and we recover Eq. 4.16.

4.5 Applying FSI's to QED Amplitudes

In order to develop the expression for applying FSI corrections to QED amplitudes, we first find the expression for correcting amplitudes in nonrelativistic collision theory [34], in the Born approximation. Once the expression for the correction is derived, we use the cross-section to relate the collision theory amplitude to the QED amplitude. Applying the resulting relation gives us an expression for correcting QED amplitudes for FSI effects. We specialize to an interaction with two particles in the final state.

In collision theory, consider the Hamiltonian $H = H_0 + V$ where H_0 is the kinetic

³Note that Geiger and Swanson [14] associate a different constant factor with their definition of $\psi_{(BC)LM_L}(\vec{r}_{BC}, \vec{w})$, they neglect the phase i^{-L} , and they do not explicitly mention the factor of $e^{i\delta_L}$.

energy term, and V is the potential. $V = W + U$ is divided into the potential representing the basic interaction, W , and the FSI potential U . The plane waves $\phi_{\vec{k}}(\vec{r})$ are the solutions of the Schrödinger equation in the absence of a potential,

$$(H_0 - E) \phi_{\vec{k}}(\vec{r}) = 0, \quad (4.19)$$

the stationary scattering waves $\chi_{\vec{k}}^{\pm}(\vec{r})$ are the solutions with the full potential,

$$(H_0 + W + U - E) \chi_{\vec{k}}^{\pm}(\vec{r}) = 0, \quad (4.20)$$

and the stationary scattering waves $\psi_{\vec{k}}^{\pm}(\vec{r})$ are the solutions with the FSI potential only,

$$(H_0 + U - E) \psi_{\vec{k}}^{\pm}(\vec{r}) = 0. \quad (4.21)$$

The $\chi_{\vec{k}}^{\pm}(\vec{r})$ are also solutions of the equivalent integral equation,

$$\chi_{\vec{k}}^{\pm} = \left(1 + \frac{1}{E - H_0 - V \pm i\varepsilon} V \right) \phi_{\vec{k}}. \quad (4.22)$$

The regular transition amplitude is defined in terms of the transition operator between plane waves, or in terms of the potential between a plane wave and a stationary scattering wave:

$$\langle f | T | i \rangle \equiv \langle \phi_{\vec{k}_f} | T | \phi_{\vec{k}_i} \rangle = \langle \phi_{\vec{k}_f} | V | \chi_{\vec{k}_i}^+ \rangle = \langle \chi_{\vec{k}_f}^- | V | \phi_{\vec{k}_i} \rangle. \quad (4.23)$$

In the Born approximation, we assume that V is sufficiently small that $\chi_{\vec{k}}^{\pm}(\vec{r}) \simeq \phi_{\vec{k}}(\vec{r})$ and we can replace $\chi_{\vec{k}}^{\pm}(\vec{r})$ by $\phi_{\vec{k}}(\vec{r})$ in the expression for $\langle f | T | i \rangle$:

$$\langle f | T | i \rangle \simeq \langle f | T | i \rangle^{\text{BORN}} \equiv \langle \phi_{\vec{k}_f} | V | \phi_{\vec{k}_i} \rangle. \quad (4.24)$$

We will use the Born approximation from this point on, but will drop the ^{BORN} notation for convenience.

Now consider the problem of FSI's. We have a very good theory (QED) that will calculate the transition amplitude due to just the basic interaction between plane waves, $\langle f|T|i\rangle = \langle \phi_{\vec{k}_f}|W|\phi_{\vec{k}_i}\rangle$, but we need to find a way to include the FSI effects (the potential U). To do this we use a final state that includes the FSI effects, $\psi_{\vec{k}}^- (\vec{r})$, so only the potential W is left between the initial and final states:

$$\langle f|T|i\rangle^{\text{FSI}} = \langle \psi_{\vec{k}_f}^- |W|\phi_{\vec{k}_i}\rangle. \quad (4.25)$$

Next, we make use of the plane wave orthogonality and closure conditions

$$\langle \phi_{\vec{k}} | \phi_{\vec{k}'} \rangle = (2\pi)^3 \delta^3(\vec{k} - \vec{k}'), \quad (4.26)$$

$$\frac{1}{(2\pi)^3} \int d^3 \vec{k} | \phi_{\vec{k}} \rangle \langle \phi_{\vec{k}} | = I \quad (4.27)$$

to obtain

$$\begin{aligned} \langle f|T|i\rangle^{\text{FSI}} &= \frac{1}{(2\pi)^3} \int d^3 \vec{k} \langle \psi_{\vec{k}_f}^- | \phi_{\vec{k}} \rangle \langle \phi_{\vec{k}} | W | \phi_{\vec{k}_i} \rangle \\ &= \frac{1}{(2\pi)^{\frac{3}{2}}} \int d^3 \vec{k} \psi_{\vec{k}_f}^{-*}(\vec{k}) \langle f|T|i\rangle, \end{aligned} \quad (4.28)$$

where $\psi_{\vec{k}_f}^{-*}(\vec{k})$ is the complex conjugate of the momentum-space solution of the Schrödinger equation (Eq. 4.1) with the FSI potential U .

To be able to apply this to QED amplitudes, we need to know how the non-relativistic scattering amplitudes relate to QED amplitudes. A comparison of the expressions for the total cross-section reveals that $|\mathcal{M}|^2 \propto s |\langle f|T|i\rangle|^2$ where s is the Mandelstam variable.⁴ Fourier-transforming Eq. 4.9 to momentum space, we find

⁴In the CM frame, the total energy is given by \sqrt{s} .

that the QED amplitude corrected for FSI effects is

$$\begin{aligned} \mathcal{M}^{\text{FSI}}(\vec{k}_f) &= \frac{2}{\pi} \sqrt{s(k_f)} \sum_{l=0}^{\infty} \sum_{m_l=-l}^l e^{i\delta_l} Y_{lm_l}(\Omega_{k_f}) \int d^3\vec{k} \frac{\mathcal{M}(\vec{k})}{\sqrt{s(k)}} Y_{lm_l}^*(\Omega_k) \\ &\times \int_0^\infty dr r^2 j_l(kr) u_l(k_f, r) \end{aligned} \quad (4.29)$$

where s and \mathcal{M} have been written as functions of the momenta in order to show whether they are calculated with the variable of integration, \vec{k} , or the relative momentum between the final state particles in the CM frame, \vec{k}_f . There is ambiguity as to how to relate k and $s(k)$ – nonrelativistically or relativistically. We follow the usual practice of keeping as much as possible relativistic, and so use for equal-mass final state particles: $s(k) = 4k^2 + 4m^2$.

It is worthwhile to expand each \mathcal{M} into partial waves,

$$\mathcal{M}(\vec{k}) \equiv \sum_{L=0}^{\infty} \sum_{M_L=-L}^L f_{LM_L}(s(k)) Y_{LM_L}(\Omega_k) \quad (4.30)$$

in order to get the FSI correction for a single partial wave

$$f_{LM_L}^{\text{FSI}}(s(k_f)) = \frac{2}{\pi} \sqrt{s(k_f)} e^{i\delta_L} \int_0^\infty dk \int_0^\infty dr r^2 k^2 \frac{f_{LM_L}(s(k))}{\sqrt{s(k)}} j_L(kr) u_L(k_f, r). \quad (4.31)$$

In the absence of an FSI potential, $\delta_L \Rightarrow 0$, $u_L(k_f, r) \Rightarrow j_L(k_f r)$, the orthogonality condition of the spherical Bessel functions gives us a delta function, and we obtain $f_{LM_L}^{\text{FSI}}(s(k_f)) = f_{LM_L}(s(k_f))$ as we should.

Chapter 5

Final State Interactions: An Application

5.1 The Interaction $\gamma\gamma \rightarrow \pi\pi$

In 1986, a group at Orsay (using DM1 on DCI) measured the cross-section of $\gamma\gamma \rightarrow \pi^+\pi^-$ near the $\pi\pi$ threshold, and found a cross-section about twice that expected from scalar QED¹ [36]. Although statistically not very significant (a 2σ effect), the result aroused interest because it differed from theoretical expectations. By Low's low energy theorem [37] the interaction of low energy photons depends only on the static properties of the target. Because at low energies the long wavelength photons cannot make out the individual constituents of the pions, the pion-photon coupling depends only on the charge of the pion, and the pion can be treated as a point particle in scalar QED. The strong final state interactions (FSI's) between the outgoing pions were not expected to be as significant as the electroweak effects.

¹Scalar QED refers to a subset of QED that deals with the interactions of just photons and scalar (spin 0) particles. Because the pions really consist of two spin- $\frac{1}{2}$ quarks, scalar QED is used here as an effective theory that is valid at low energies because the long wavelength photons cannot make out the individual quarks.

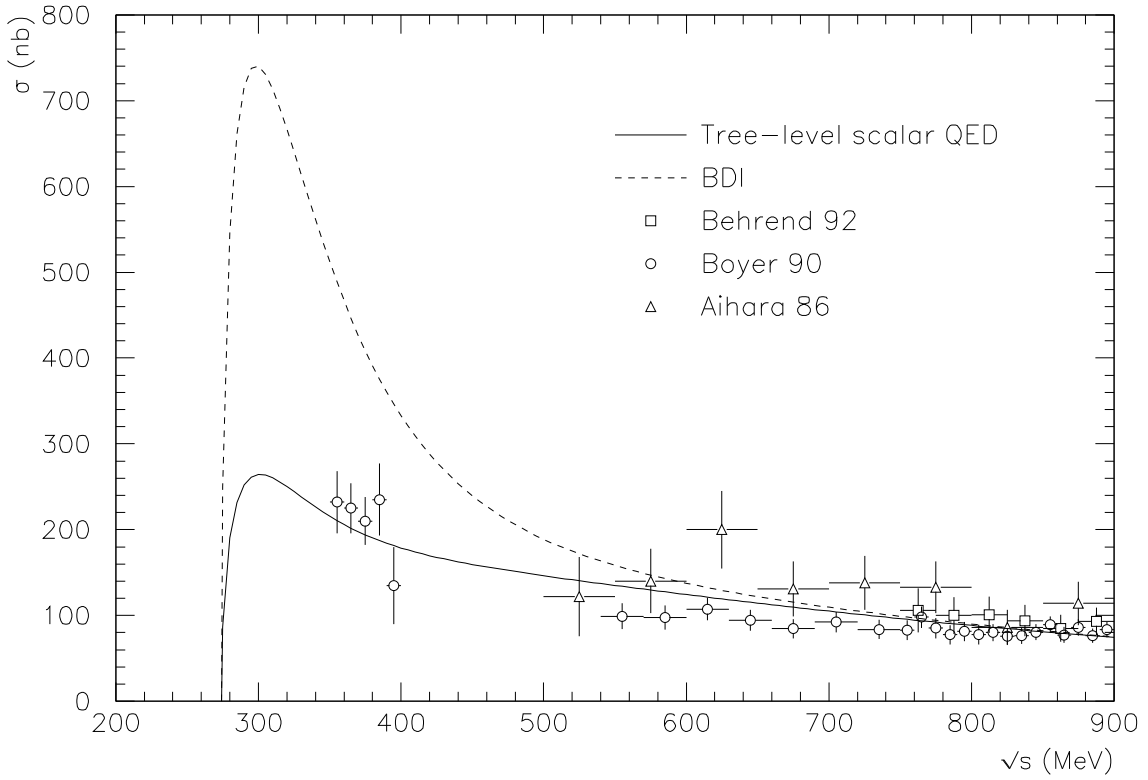


Figure 5.1: Graph of the $\gamma\gamma \rightarrow \pi^+\pi^-$ total cross-section vs. \sqrt{s} , for the tree-level scalar QED and BDI predictions (reproduced by us), and recent data. The curves have been corrected to have a limited polar acceptance to match the data: $|\cos\theta| \leq 0.6$. The data is from Behrend *et al.* [38], Boyer *et al.* [39] and Aihara *et al.* [40]. Some of the data shown in this chapter was obtained by us from References [41] and [42]. The horizontal error bars on the data show the bin sizes; for the vertical error bars all of the given errors were added together in quadrature.

In 1987, Barnes, Dooley and Isgur (BDI) [43] estimated the effects of these FSI's using the Fermi approximation (see Section 4.3) with an effective potential extracted from a quark model, and found a similar enhancement. Unfortunately, the experimental enhancement has since disappeared; the early experiments were apparently plagued by problems with subtracting the lepton background due to low statistics [44], and the later experiments show no such enhancement. Figure 5.1 shows the two curves and the latest experimental data. Note that the data fits the tree-level scalar QED curve well for the whole range shown (up to a CM energy of 900 MeV), even

though we would not necessarily expect it to be accurate at the higher energies.

Calculations of the $\gamma\gamma \rightarrow \pi\pi$ cross-sections have been done using other methods. One-loop chiral perturbation theory has produced mixed results: the $\gamma\gamma \rightarrow \pi^+\pi^-$ cross-section curve [45] shows a small enhancement over the tree-level scalar QED curve near threshold that is still compatible with the latest experimental data, while the $\gamma\gamma \rightarrow \pi^0\pi^0$ cross-section curve [45, 46] has a shape that is rather different from the data. However, a two-loop chiral perturbation theory calculation of the $\gamma\gamma \rightarrow \pi^0\pi^0$ cross-section [47] agrees with the data. The difference is apparently mainly due to $\pi\pi$ rescattering and renormalization of the pion decay constant.

Calculations of the $\gamma\gamma \rightarrow \pi\pi$ cross-sections have also been done with dispersion relations, typically using phase shift data from $\pi\pi$ scattering, and constraints from unitarity, analyticity and crossing. The $\gamma\gamma \rightarrow \pi^+\pi^-$ cross-section results are again quite similar to both the tree-level scalar QED curve and the experimental data near threshold [48, 49]. The $\gamma\gamma \rightarrow \pi^0\pi^0$ cross-section results also do well [44, 49], showing good agreement with the data. It is believed that higher order exchange effects, whose absence is problematic for the one-loop chiral perturbation theory calculation, are included in the dispersive calculation through the unitarity requirement [49].

On the face of it, the failure of the quark model to do as well as these other two approaches represents quite a blow to its reputation. Being able to predict the effects of FSI's is important if we are to understand QCD. In addition, if we understood the situation in $\gamma\gamma \rightarrow$ two pseudoscalar mesons, we could then approach the situation in $\gamma\gamma \rightarrow$ two vector mesons with more confidence; the structures seen in the cross-sections of these processes are not well understood and are a long-standing puzzle.

However, there is room for improvement in the BDI calculation. We will redo the calculation using the full FSI apparatus of Section 4.5, and newer, better potentials. In addition, we will calculate the cross-section for the process $\gamma\gamma \rightarrow \pi^0\pi^0$. Since neutral pions do not couple to long wavelength photons (there is no such process in

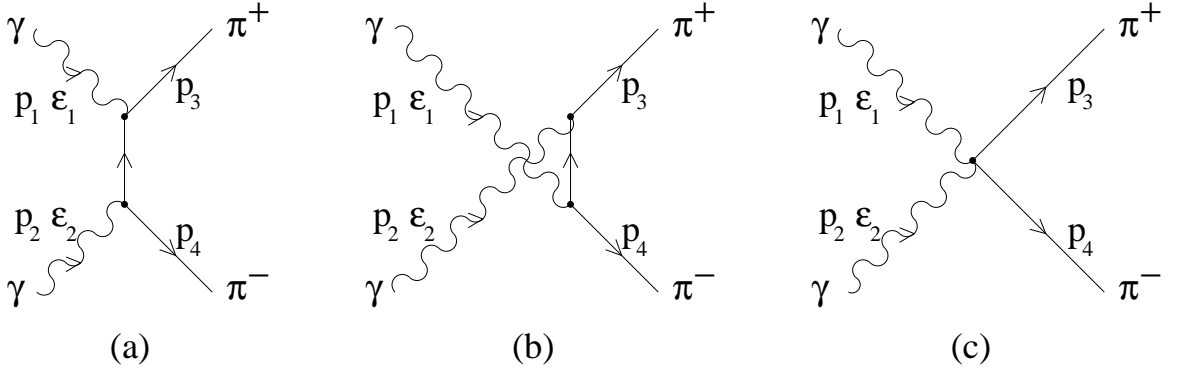


Figure 5.2: The tree-level Feynman diagrams for the scalar QED interaction $\gamma\gamma \rightarrow \pi^+\pi^-$. The labels of the particle momenta (p_i) and photon polarization vectors (ϵ_i) are shown.

scalar QED), $\gamma\gamma \rightarrow \pi^0\pi^0$ is expected to be suppressed relative to $\gamma\gamma \rightarrow \pi^+\pi^-$ making the effects of the FSI's relatively much more significant. In our calculation, it is the FSI potentials that mix the $\pi^+\pi^-$ final state into $\pi^0\pi^0$.

In Section 5.2 we calculate the cross-section for $\gamma\gamma \rightarrow \pi^+\pi^-$ in tree-level scalar QED. In Section 5.3 we discuss the effective potentials and the application of the full FSI apparatus (see Section 4.5) to this problem. In Section 5.4 we give the results of our calculations.

5.2 $\gamma\gamma \rightarrow \pi^+\pi^-$ in Tree-level Scalar QED

The three tree-level scalar QED Feynman diagrams² contributing to the interaction $\gamma\gamma \rightarrow \pi^+\pi^-$ are shown in Figure 5.2.

The corresponding Feynman amplitude (using the momenta and photon polarization labels shown in Figure 5.2) is

$$\mathcal{M} = 4\pi\alpha \left[\frac{\epsilon_1 \cdot (2p_3 - p_1) \epsilon_2 \cdot (2p_4 - p_2)}{(p_2 - p_4)^2 - m^2} + \frac{\epsilon_1 \cdot (2p_4 - p_1) \epsilon_2 \cdot (2p_3 - p_2)}{(p_1 - p_4)^2 - m^2} + 2\epsilon_1 \cdot \epsilon_2 \right] \quad (5.1)$$

²See Appendix A.2 for a brief explanation of Feynman diagrams.

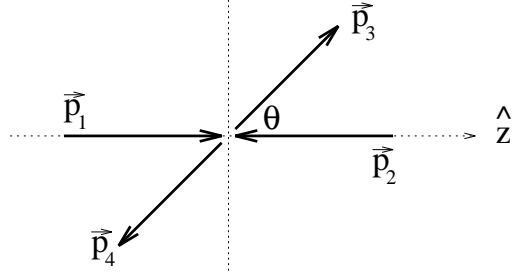


Figure 5.3: The geometry of the $\gamma\gamma \rightarrow \pi^+\pi^-$ interaction in the CM frame.

where α is the fine structure constant and m is the pion mass. Averaging the photon polarizations and integrating over phase space gives us the total cross-section

$$\sigma = \frac{\pi\alpha^2}{4m^2} \left[2x(1+x)\sqrt{1-x} - x^2(2-x) \ln \left(\frac{1+\sqrt{1-x}}{1-\sqrt{1-x}} \right) \right] \quad (5.2)$$

where $x \equiv \frac{4m^2}{s}$ and s is the Mandelstam variable.

We would now like to work out the cross-sections corresponding to different partial waves in the final state. In the CM frame, we take \vec{p}_1 to point in the positive z direction, and the direction of \vec{p}_3 to be described by the spherical polar coordinates θ and ϕ , as shown in Figure 5.3. For the photons we take circular polarizations:

$$\begin{aligned} \epsilon_1(+) = \epsilon_2(-) &= \frac{1}{\sqrt{2}}(0, -1, -i, 0), \\ \epsilon_1(-) = \epsilon_2(+) &= \frac{1}{\sqrt{2}}(0, 1, -i, 0). \end{aligned} \quad (5.3)$$

We calculate the helicity amplitudes

$$\begin{aligned} \mathcal{M}_{++} = \mathcal{M}_{--} &= \frac{8\pi\alpha x}{1 - (1-x)\cos^2\theta}, \\ \mathcal{M}_{\pm\mp} &= \frac{8\pi\alpha (1-x)\sin^2\theta e^{\pm 2i\phi}}{1 - (1-x)\cos^2\theta}, \end{aligned} \quad (5.4)$$

and then expand them in a spherical harmonic basis to obtain the partial waves (e.g. for the $++$ case),

$$\begin{aligned}\mathcal{M}_{++} &\equiv \sum_{L=0}^{\infty} \sum_{M_L=-L}^L f_{LM_L}^{++} Y_{LM_L}(\theta, \phi) \\ \Rightarrow f_{LM_L}^{++} &= \int d\Omega Y_{LM_L}^*(\theta, \phi) \mathcal{M}_{++}.\end{aligned}\quad (5.5)$$

We find that $f_{LM_L}^{++} = f_{LM_L}^{--}$ is only non-zero for $M_L = 0$ and that $f_{LM_L}^{+-} = f_{-M_L}^{-+}$ is only non-zero for $M_L = 2$.³ The cross-section is then written in terms of the partial waves as

$$\sigma = \frac{\sqrt{1-x}}{128\pi^2 s} \left[(f_{00}^{++})^2 + \sum_{L \geq 2, \text{even}}^{\infty} \left[(f_{L0}^{++})^2 + (f_{L2}^{+-})^2 \right] \right]. \quad (5.6)$$

The needed partial waves (see below) are given by

$$\begin{aligned}f_{00}^{++} &= 8\pi^{\frac{3}{2}}\alpha \frac{x}{\sqrt{1-x}} \ln \left(\frac{1+\sqrt{1-x}}{1-\sqrt{1-x}} \right), \\ f_{20}^{++} &= 4\sqrt{5}\pi^{\frac{3}{2}}\alpha \frac{x}{1-x} \left[-6 + \frac{2+x}{\sqrt{1-x}} \ln \left(\frac{1+\sqrt{1-x}}{1-\sqrt{1-x}} \right) \right], \\ f_{22}^{+-} &= 4\sqrt{\frac{15}{2}}\pi^{\frac{3}{2}}\alpha \left[\frac{10}{3} - \frac{2}{1-x} + \frac{x^2}{(1-x)^{\frac{3}{2}}} \ln \left(\frac{1+\sqrt{1-x}}{1-\sqrt{1-x}} \right) \right], \\ f_{40}^{++} &= 3\pi^{\frac{3}{2}}\alpha \frac{x}{1-x} \left[\frac{110}{3} - \frac{70}{1-x} + \frac{3x^2 + 24x + 8}{(1-x)^{\frac{3}{2}}} \ln \left(\frac{1+\sqrt{1-x}}{1-\sqrt{1-x}} \right) \right], \\ f_{42}^{+-} &= 3\sqrt{10}\pi^{\frac{3}{2}}\alpha \left[\frac{-54}{5} + \frac{76}{3(1-x)} - \frac{14}{(1-x)^2} + \frac{x^2(6+x)}{(1-x)^{\frac{5}{2}}} \ln \left(\frac{1+\sqrt{1-x}}{1-\sqrt{1-x}} \right) \right], \\ f_{60}^{++} &= 8\sqrt{13}\pi^{\frac{3}{2}}\alpha \frac{x}{1-x} \left[-\frac{231}{40} + \frac{7(4-15x)}{8(1-x)} - \frac{21(1+5x+5x^2)}{8(1-x)^2} \right. \\ &\quad \left. + \frac{16+120x+90x^2+5x^3}{16(1-x)^{\frac{5}{2}}} \ln \left(\frac{1+\sqrt{1-x}}{1-\sqrt{1-x}} \right) \right].\end{aligned}\quad (5.7)$$

The total cross-section and the cross-sections of the $L = 0, 2, 4$ partial waves are

³The orbital angular momentum L between the pions is even because of charge conjugation invariance.

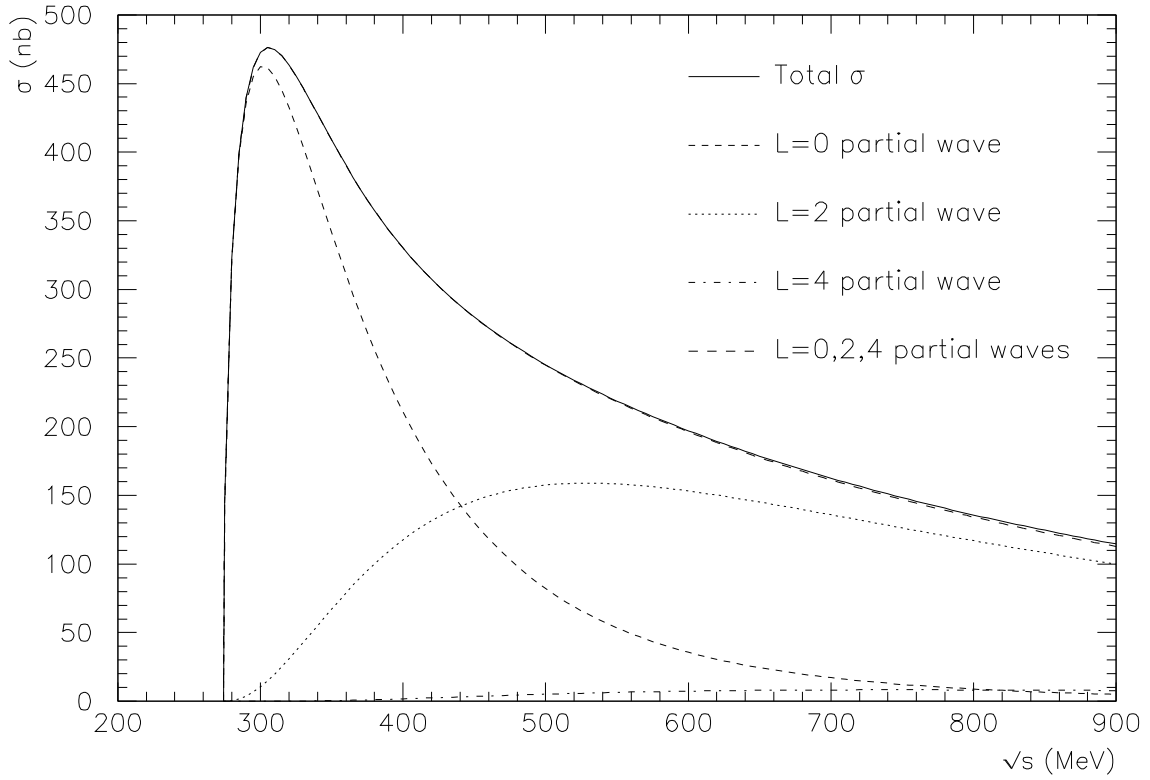


Figure 5.4: Graph of the $\gamma\gamma \rightarrow \pi^+\pi^-$ tree-level scalar QED cross-sections vs. \sqrt{s} . The total cross-section is shown, as well as the cross-sections of the $L = 0, 2, 4$ partial waves, and the cross-section corresponding to the sum of the $L = 0, 2, 4$ partial waves. The curves are for full polar acceptance: $|\cos \theta| \leq 1$, which is why they differ from those shown in Figure 5.1.

shown in Figure 5.4.

5.3 Applying the FSI Correction

5.3.1 The Effective Potentials We Use

The $\pi-\pi$ potentials that we use were calculated by Swanson *et al.* [50, 51, 52] using techniques developed by Barnes and Swanson [53]. The potentials come from equating the T-matrix giving the leading order interactions in a perturbation theory for a nonrelativistic quark model, to the T-matrix for the interactions of point-like mesons,

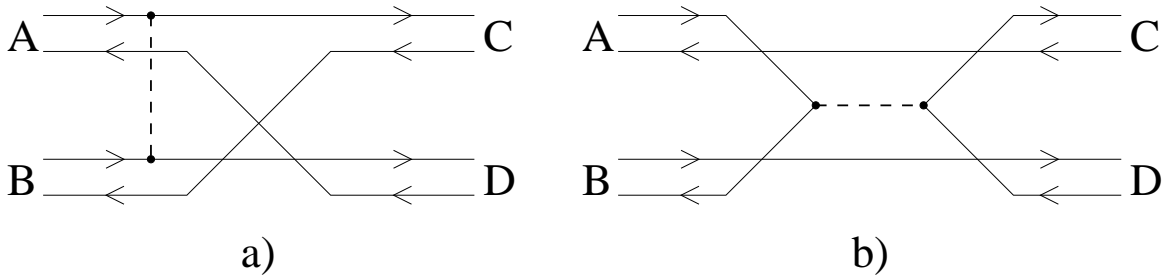


Figure 5.5: Example diagrams of the two classes of interactions included in the quark model used to find the effective potentials: a) t-channel gluon exchange, b) s-channel gluon exchange.

written in terms of the effective potential they were trying to find.

The potentials are different for the different isospin states of the two pions. Because of charge conjugation invariance, the orbital angular momentum L between the two pions must be even. Because of Bose-Einstein symmetry (which holds for members of the same isospin multiplet in the context of the strong interaction [54]), the sum $L + I$ must be even, and hence the total isospin I must be even as well. It then follows that the isospin states (written as $|II_z\rangle$) of the pions are

$$\begin{aligned} |\pi^+\pi^-\rangle &= \sqrt{\frac{2}{3}}|00\rangle + \frac{1}{\sqrt{3}}|20\rangle, \\ |\pi^0\pi^0\rangle &= -\frac{1}{\sqrt{3}}|00\rangle + \sqrt{\frac{2}{3}}|20\rangle. \end{aligned} \quad (5.8)$$

There are two classes of interaction included in the quark model used to find the effective potentials. The first, referred to as t-channel gluon exchange by Swanson *et al.*, involves both one-gluon-exchange and a linear confining potential, followed by quark rearrangement back into colour singlet states. This can occur for both $I = 0$ and $I = 2$ states. The second, referred to as s-channel gluon exchange, involves the annihilation of two of the quarks, producing a meson hybrid in the intermediate state. Because of the intermediate state, this interaction can only occur for $I = 0$ states. Example diagrams of the two classes of interaction are shown in Figure 5.5.

We only present results for FSI corrections to the $L = 0$ partial wave of $\gamma\gamma \rightarrow \pi\pi$ because the $L = 2$ potentials available from the same sources are smaller than those for $L = 0$, and we found that their effect on the cross-section was negligible.

Although relativistic phase space is included in the quark model used to find the effective potentials, the potentials themselves are essentially nonrelativistic. It is our hope that they will contain enough physics to correctly calculate the distortion of the final state wavefunction leading to FSI effects. However, it is known [55, 53, 50] that the t-channel gluon exchange potential is unable to accurately predict the phase shifts resulting from $I = 2$ $\pi\pi$ scattering, apparently because it lacks relativistic phase space. It is expected that the other potentials suffer from the same problem.

Weinstein and Isgur [55] have argued that this is related to the inability of the nonrelativistic quark model to accurately predict the charge radii of the ground state mesons and baryons, and so apply a correction factor $\kappa = 2.0$ to the ranges of the $\pi\pi$ potentials, and an overall normalization factor $\eta = 0.6$ which is fitted to experiment. To be specific, a potential originally parametrized by

$$V(r) = V_0 e^{-\frac{1}{2}\left(\frac{r}{r_0}\right)^2} \quad (5.9)$$

is written as

$$V(r) = \eta V_0 e^{-\frac{1}{2}\left(\frac{r}{\kappa r_0}\right)^2} \quad (5.10)$$

with the corrections. However, it is not clear whether a factor that corrects the phase shift for the nonrelativistic phase space will necessarily give the correct dynamics for the distortion of the wavefunction. A better approach might be to use the potentials without η and κ to obtain the wavefunctions, but to use the phase shifts calculated directly in the quark model⁴ to predict the FSI effects (in Eq. 4.31 for example). Swanson *et al.* [53, 50, 51] found that the quark model, with its relativistic phase

⁴We refer to the specific quark model used by Swanson *et al.* to extract the effective potentials.

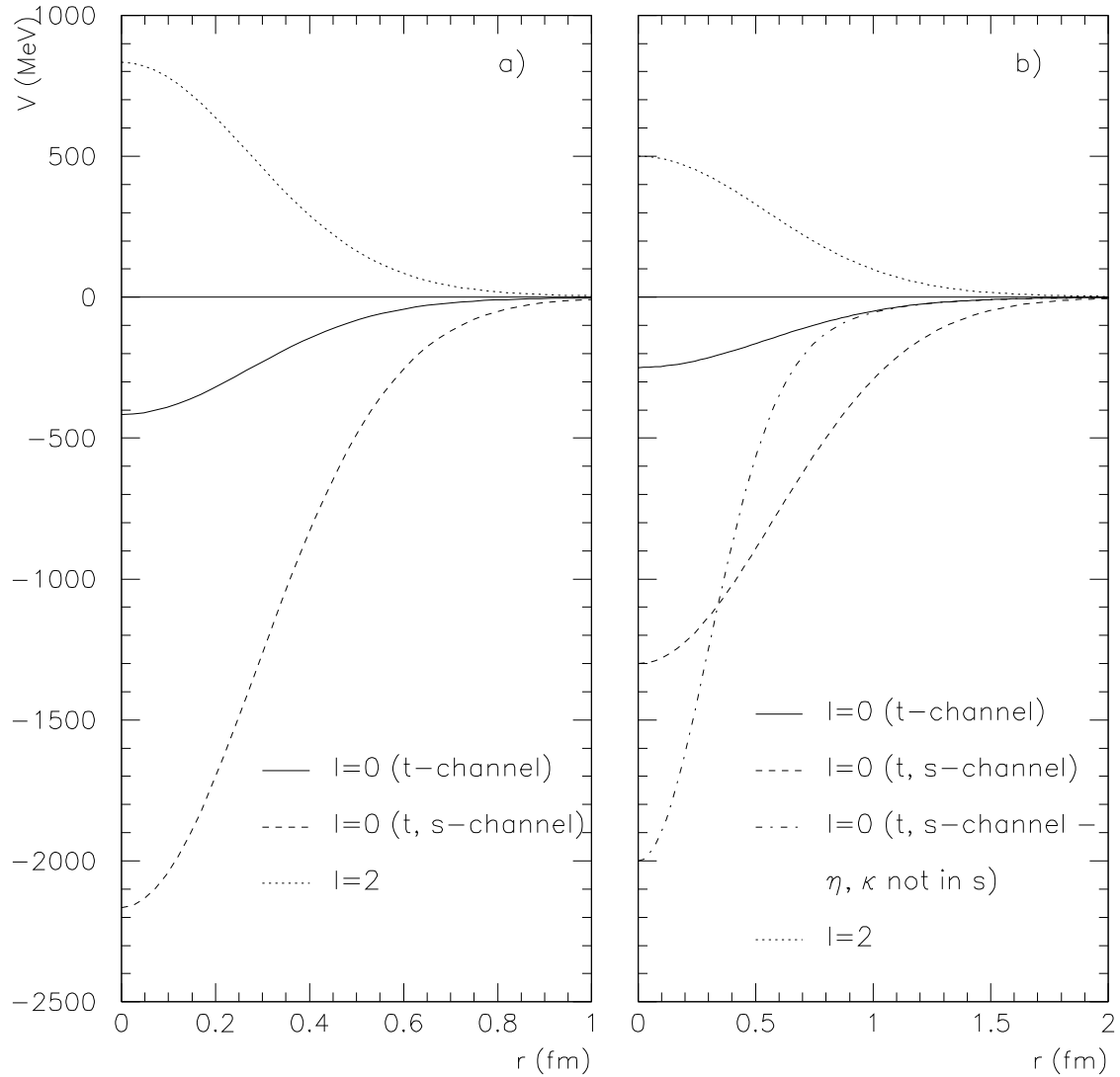


Figure 5.6: Graphs of the $\pi\pi$ potentials used in this work vs. r . Note the different scales on the two r axes. T-channel gluon exchange is present in all potentials. For $I = 0$, the potentials are plotted both with and without the contribution from s-channel gluon exchange. In a), the potentials without the factors η and κ are plotted. In b), the potentials with $\eta = 0.6$ and $\kappa = 2.0$ are plotted, except for one curve where the contribution from t-channel gluon exchange contains η and κ , but that from s-channel gluon exchange does not.

space, does accurately reproduce the $\pi\pi$ scattering phase shifts away from threshold (although resonance effects must be added for $I = 0$ – see below).

In addition, since η and κ have previously been applied only to potentials rep-

Pion State		$\pi-\pi$ Potentials (V_0 in GeV, r_0 in GeV $^{-1}$)					
		t-channel gluon exchange			s-channel gluon exchange		
L	I	hyperfine		confinement		V_0	r_0
		V_0	r_0	V_0	r_0		
0	0	-0.392	1.36	-0.024	2.29	-1.75	1.48
0	2	0.786	1.36	0.047	2.29		
2	0	-0.044	1.40	0.0175	1.49		
2	2	0.088	1.40	-0.035	1.49		

Table 5.1: The parameters of the potentials used in this work [50, 51, 52]. The t-channel gluon exchange potentials have two contributions, due to colour-hyperfine and confinement terms, which must be summed. The potentials are parametrized as in Eqs. 5.9 and 5.10, depending on whether η and κ are to be included or not.

resenting t-channel gluon exchange, it is not entirely clear if they should be applied to the potential representing s-channel gluon exchange. We will examine these three possibilities below. The various potentials, with and without the η and κ , are shown in Figure 5.6. The parameters V_0 and r_0 of the potentials considered (including the $L = 2$ potentials, for completeness) are given in Table 5.1.

5.3.2 The FSI Apparatus Applied to the Pions

Calculating the effects of FSI's on the $\gamma\gamma \rightarrow \pi^+\pi^-$ cross-sections is complicated by the fact that there are two isospin states involved. Because the $I = 0$ and $I = 2$ states feel different potentials, they will be affected differently by the FSI's. This will unbalance the isospin combination that is $\pi^+\pi^-$, leading to some $\pi^0\pi^0$ production. BDI used a single $\pi^+\pi^-$ potential, and hence neglected conversion to $\pi^0\pi^0$.

We have two choices as to how to proceed. We could transform the potentials from the $I = 0$ and $I = 2$ basis to the $\pi^+\pi^-$ and $\pi^0\pi^0$ basis (leading to off-diagonal potential terms that would mix the two states), and then solve a coupled-channel Schrödinger equation to find the final state wavefunctions needed for the FSI calculations (see for example Reference [56]). Alternatively, we could take advantage of the facts that the

potential matrix is diagonal in the isospin basis (since isospin is conserved in strong interactions), and that we are assuming the pion states to be degenerate in mass (at 137 MeV), and just solve uncoupled Schrödinger equations in the isospin basis. We opt for this second choice.

The cross-section for $\gamma\gamma \rightarrow \pi\pi$, corrected for FSI effects, is given by ⁵ (cf. Eq. 5.6)

$$\sigma_{\pi\pi}^{\text{FSI}} = \frac{\mathcal{S}\sqrt{1-x}}{128\pi^2 s} \left[\left| f_{00\pi\pi}^{\text{FSI}} \right|^2 + \sum_{L \geq 2, \text{even}}^{\infty} \left[\left| f_{L0\pi\pi}^{\text{FSI}} \right|^2 + \left| f_{L2\pi\pi}^{\text{FSI}} \right|^2 \right] \right]. \quad (5.11)$$

Note that we have not yet specified the charges of the pions – $\mathcal{S} \equiv 1/(1 + \delta_{\pi\pi})$ is a statistical factor which is needed if the pions are identical particles (i.e. $\pi^0\pi^0$).

The calculation of $f_{LM_L\pi\pi}^{\text{FSI}}$ proceeds similarly to that in Section 4.5 – the first divergence is in Eq. 4.28, which is replaced by

$$\begin{aligned} \langle f | T | i \rangle^{\text{FSI}} &= \frac{1}{(2\pi)^3} \int d^3\vec{k} \langle \psi_{\vec{k}_f}^{-\pi\pi} | \left[|\phi_{\vec{k}}^{\pi^+\pi^-}\rangle \langle \phi_{\vec{k}}^{\pi^+\pi^-}| + |\phi_{\vec{k}}^{\pi^0\pi^0}\rangle \langle \phi_{\vec{k}}^{\pi^0\pi^0}| \right] W | \phi_{\vec{k}_i} \rangle \\ &= \frac{1}{(2\pi)^3} \int d^3\vec{k} \langle \psi_{\vec{k}_f}^{-\pi\pi} | \phi_{\vec{k}}^{\pi^+\pi^-} \rangle \langle \phi_{\vec{k}}^{\pi^+\pi^-} | W | \phi_{\vec{k}_i} \rangle \end{aligned} \quad (5.12)$$

where we have inserted plane waves for both $\pi^+\pi^-$ and $\pi^0\pi^0$ – the $\pi^0\pi^0$ term is then dropped because $\pi^0\pi^0$ isn't produced from $\gamma\gamma$ in tree-level scalar QED, which is what the potential W represents.

We can proceed as before, and relate the final bra-ket to the scalar QED amplitude, and the left-hand side to the corrected scalar QED amplitude. The first bra-ket can be written in the isospin basis using Eq. 5.8 as one of

$$\langle \psi_{\vec{k}_f}^{-\pi^+\pi^-} | \phi_{\vec{k}}^{\pi^+\pi^-} \rangle = \left[\sqrt{\frac{2}{3}} \langle \psi_{\vec{k}_f}^{-0} | + \frac{1}{\sqrt{3}} \langle \psi_{\vec{k}_f}^{-2} | \right] \left[\sqrt{\frac{2}{3}} |\phi_{\vec{k}}^0\rangle + \frac{1}{\sqrt{3}} |\phi_{\vec{k}}^2\rangle \right]$$

⁵Note that we have dropped the $^{++}$ and $^{+-}$ helicity notation on the f 's – it can be identified from the value of M_L anyway ($M_L = 0 \Rightarrow ^{++}$, $M_L = 2 \Rightarrow ^{+-}$).

$$\begin{aligned}
&= (2\pi)^{\frac{3}{2}} \left[\frac{2}{3} \psi_{\vec{k}_f}^{-0*}(\vec{k}) + \frac{1}{3} \psi_{\vec{k}_f}^{-2*}(\vec{k}) \right], \\
\langle \psi_{\vec{k}_f}^{-\pi^0\pi^0} | \phi_{\vec{k}}^{\pi^+\pi^-} \rangle &= (2\pi)^{\frac{3}{2}} \left[-\frac{\sqrt{2}}{3} \psi_{\vec{k}_f}^{-0*}(\vec{k}) + \frac{\sqrt{2}}{3} \psi_{\vec{k}_f}^{-2*}(\vec{k}) \right], \tag{5.13}
\end{aligned}$$

depending on which pion state is produced in the end. Here $\psi_{\vec{k}_f}^{-I*}(\vec{k})$ is the complex conjugate of the momentum-space solution of the Schrödinger equation (Eq. 4.1) with the potential for isospin I . If $u_L^I(k_f, r)$ is the solution of the equivalent radial equation (Eq. 4.2) with orbital angular momentum L , then Eq. 4.31 becomes for $\pi^+\pi^-$ production,

$$\begin{aligned}
f_{LM_L \pi^+\pi^-}^{\text{FSI}}(s(k_f)) &= \frac{2}{\pi} \sqrt{s(k_f)} \int_0^\infty dk \int_0^\infty dr \ r^2 k^2 \frac{f_{LM_L}(s(k))}{\sqrt{s(k)}} j_L(kr) \\
&\times \left[\frac{2}{3} e^{i\delta_L^0} u_L^0(k_f, r) + \frac{1}{3} e^{i\delta_L^2} u_L^2(k_f, r) \right], \tag{5.14}
\end{aligned}$$

where δ_L^I is the phase shift of $u_L^I(k_f, r)$.

In order to keep things real, we define

$$g_{LM_L}^I(s(k_f)) \equiv \frac{2}{\pi} \sqrt{s(k_f)} \int_0^\infty dk \int_0^\infty dr \ r^2 k^2 \frac{f_{LM_L}(s(k))}{\sqrt{s(k)}} j_L(kr) u_L^I(k_f, r), \tag{5.15}$$

which gives

$$|f_{LM_L \pi^+\pi^-}^{\text{FSI}}|^2 = \frac{4}{9} (g_{LM_L}^0)^2 + \frac{1}{9} (g_{LM_L}^2)^2 + \frac{4}{9} g_{LM_L}^0 g_{LM_L}^2 \cos(\delta_L^0 - \delta_L^2). \tag{5.16}$$

Similarly, for $\pi^0\pi^0$ production, we get

$$|f_{LM_L \pi^0\pi^0}^{\text{FSI}}|^2 = \frac{2}{9} (g_{LM_L}^0)^2 + \frac{2}{9} (g_{LM_L}^2)^2 - \frac{4}{9} g_{LM_L}^0 g_{LM_L}^2 \cos(\delta_L^0 - \delta_L^2). \tag{5.17}$$

Note that if there is no FSI potential, $\delta_L^I \Rightarrow 0$, $u_L^I(k_f, r) \Rightarrow j_L(k_f r)$, and the orthogonality condition of the spherical Bessel functions gives us a delta function, so

$g_{LM_L}^I \Rightarrow f_{LM_L}$ and we obtain $f_{LM_L \pi^+ \pi^-}^{\text{FSI}} = f_{LM_L}$ and $f_{LM_L \pi^0 \pi^0}^{\text{FSI}} = 0$, as expected.

In this work, we only correct the $L = 0$ partial wave, because higher partial waves have negligible FSI effects. Thus in Eq. 5.11 only the $f_{00\pi\pi}^{\text{FSI}}$ term survives for $\pi^0\pi^0$, and for $\pi^+\pi^-$ it is the only term that differs from the uncorrected value.

5.3.3 The Problem of Limited Polar Acceptance

Expanding the scalar QED amplitudes in a spherical harmonic basis (Eq. 5.5) to obtain cross-sections for particular partial waves is essential to our calculation, but it requires that we be able to integrate over the entire 4π angular range when calculating the total cross-section. Unfortunately, experiments don't measure data over the whole polar angle ($|\cos \theta| \leq 0.6 - 0.8$ is typical), so we cannot easily compare our results with experiment.

Integrating to get the total uncorrected cross-section for a limited polar acceptance ($-\cos \theta_{\text{acc}} \leq \cos \theta \leq \cos \theta_{\text{acc}}$) is not a problem: Eq. 5.2 is replaced by

$$\sigma_{\text{acc}} = \frac{\pi \alpha^2}{4m^2} \left[2 \cos \theta_{\text{acc}} x \sqrt{1-x} \left(\frac{x^2}{1 - (1-x) \cos^2 \theta_{\text{acc}}} + 1 \right) - x^2 (2-x) \ln \left(\frac{1 + \sqrt{1-x} \cos \theta_{\text{acc}}}{1 - \sqrt{1-x} \cos \theta_{\text{acc}}} \right) \right]. \quad (5.18)$$

However, the expression in terms of partial waves is affected more drastically. Eq. 5.6 becomes (where once again we drop the explicit helicity labels)

$$\begin{aligned} \sigma_{\text{acc}} = & \frac{\sqrt{1-x}}{256\pi^2 s} \int_0^{2\pi} d\phi \int_{-\cos \theta_{\text{acc}}}^{\cos \theta_{\text{acc}}} d(\cos \theta) \left[2 \left| \sum_{L \geq 0, \text{even}}^{\infty} f_{L0} Y_{L0}(\theta, \phi) \right|^2 \right. \\ & \left. + \left| \sum_{L \geq 2, \text{even}}^{\infty} f_{L2} Y_{L2}(\theta, \phi) \right|^2 + \left| \sum_{L \geq 2, \text{even}}^{\infty} f_{L2} Y_{L-2}(\theta, \phi) \right|^2 \right]. \end{aligned} \quad (5.19)$$

For the limited polar acceptance, the spherical harmonics are not orthogonal to each

other, so each magnitude contains an infinite number of terms. As well, the contributions of the partial waves to the total cross-section can no longer be separated.

Because the $L = 0$ partial wave is expected to be the only one affected significantly by FSI's, we assume that all of the observed $\gamma\gamma \rightarrow \pi^0\pi^0$ events are in an $L = 0$ state. Since that distribution is spherically symmetric, we can correct the data to full polar acceptance by simply dividing it by the value of $\cos\theta_{\text{acc}}$ appropriate for the particular experiment.

For $\gamma\gamma \rightarrow \pi^+\pi^-$ the total cross-section observed is a mixture of all partial waves; again, we assume that only the $L = 0$ wave is affected by FSI's. Define

$$h_{l_1 l_2}^m \equiv \int_0^{2\pi} d\phi \int_{-\cos\theta_{\text{acc}}}^{\cos\theta_{\text{acc}}} d(\cos\theta) Y_{l_1 m}^*(\theta, \phi) Y_{l_2 m}(\theta, \phi) \quad (5.20)$$

and note that $h_{l_1 l_2}^m = h_{l_2 l_1}^m$ and $h_{l_1 l_2}^{-2} = h_{l_1 l_2}^2$. We can then write the total cross-section with only the $L = 0$ partial wave corrected for FSI's as the total uncorrected cross-section, plus an infinite number of correction terms, each of which is the difference between the corrected and uncorrected values of a term in Eq. 5.19. Only those terms involving f_{00} , which goes to $f_{00\pi^+\pi^-}^{\text{FSI}}$ in the correction, need correcting. Eq. 5.11 is replaced by

$$\begin{aligned} \sigma_{\text{acc},\pi^+\pi^-}^{\text{FSI}} &= \sigma_{\text{acc}} + \frac{\sqrt{1-x}}{128\pi^2 s} \left[h_{00}^0 \left\{ \left| f_{00\pi^+\pi^-}^{\text{FSI}} \right|^2 - (f_{00})^2 \right\} \right. \\ &\quad \left. + \sum_{L \geq 2, \text{even}}^{\infty} h_{L0}^0 \left\{ f_{00\pi^+\pi^-}^{\text{FSI}} f_{L0} + \left(f_{00\pi^+\pi^-}^{\text{FSI}} \right)^* f_{L0} - 2f_{00} f_{L0} \right\} \right] \\ &= \sigma_{\text{acc}} + \frac{\sqrt{1-x}}{128\pi^2 s} \left[h_{00}^0 \left\{ \frac{4}{9} \left(g_{00}^0 \right)^2 + \frac{1}{9} \left(g_{00}^2 \right)^2 + \frac{4}{9} g_{00}^0 g_{00}^2 \cos(\delta_0^0 - \delta_0^2) - (f_{00})^2 \right\} \right. \\ &\quad \left. + \sum_{L \geq 2, \text{even}}^{\infty} 2 h_{L0}^0 f_{L0} \left\{ \frac{2}{3} g_{00}^0 \cos\delta_0^0 + \frac{1}{3} g_{00}^2 \cos\delta_0^2 - f_{00} \right\} \right]. \end{aligned} \quad (5.21)$$

We find that we get excellent convergence over the energy range we are interested in

when we truncate the series after $L = 6$. Fortunately, the three experiments whose data we use for comparisons all have the same limited polar acceptance ($|\cos \theta| \leq 0.6$), so we only have to correct our results for one value of $\cos \theta_{\text{acc}}$.

5.3.4 Numerical Details

We solved the radial Schrödinger equation (Eq. 4.3) with the appropriate potentials using the Bulirsch-Stoer method for differential equations (with Stoermer's rule for 2nd order conservative equations) [57]. The solutions were started off from the origin with the forms of r times the spherical Bessel functions of the same L , since the effects of the potentials are insignificant at the origin. The amplitudes and phase shifts of the solutions were extracted by fitting the last oscillatory cycle to a general sinusoidal function. We carried out the integrals over r and k using an extended Simpson's rule.

5.4 Results

We have calculated the effects of the FSI's on $\gamma\gamma \rightarrow \pi\pi$ for three primary cases of the FSI potential (see Section 5.3.1 for a full discussion). The three cases are:

Case A. In this case we do not use η and κ in the potentials. We know that the potentials will then fail to accurately predict the phase shifts. In order to avoid problems from this, we use the phase shifts directly calculated in the quark model in our expressions for FSI corrections. For more information, see the detailed discussion on η and κ on pages 78 through 80 .

Case B. In this case we use $\eta = 0.6$ and $\kappa = 2.0$ in all of the potentials, and we use the resulting phase shifts in our expressions for FSI corrections.

Case B1. This case is the same as case B, except that η and κ are used in the t-channel gluon exchange contribution to the potentials, but not in the contri-

bution from s-channel gluon exchange.

In addition, we have three secondary cases, A', B' and B1'. Each of these is similar to the corresponding unprimed case, but does not use the same phase shifts in our expressions for FSI corrections. Instead, they use a simple (straight-line) expression⁶ for the phase shifts that attempts to describe the experimental data. We do this in order to get an idea of how much our results are affected by inaccurate phase shifts. If our results are poor because we have ignored a particular contribution to the potential (such as resonance effects), then using accurate phase shifts in the expressions for FSI corrections would partly correct for this. Of course, we would still need to determine the effect of the neglected contribution on the distortion of the wavefunction, and hence on the FSI effects.

Let us first examine the phase shift results. The $I = 2$ phase shifts are shown in Figure 5.7. For the three cases A, B and B1, the curves shown are the phase shifts that come from solving the Schrödinger equation with the potentials. The phase shift for case A is poor, as expected; in the expressions for FSI corrections we will replace it with the curve calculated directly in the quark model. The phase shifts for cases B and B1 are identical because they only differ in whether or not η and κ are included in the contribution to the potential from s-channel gluon exchange, which is not present for $I = 2$. For the range of data shown, it is not clear which is better: the B and B1 phase shifts from the Schrödinger equation, or that from the quark model. However, data at somewhat higher energies favours the quark model curve. The remaining curve shown is just a straight-line which we used to describe the data for the primed cases.

⁶The straight-line expressions we use to describe the phase shifts are:
 I=0: $\delta_0^0 = 0.0027 \text{ rad/MeV} \times (\sqrt{s} - 250 \text{ MeV})$
 I=2: $\delta_0^2 = -0.00062 \text{ rad/MeV} \times (\sqrt{s} - 250 \text{ MeV})$.

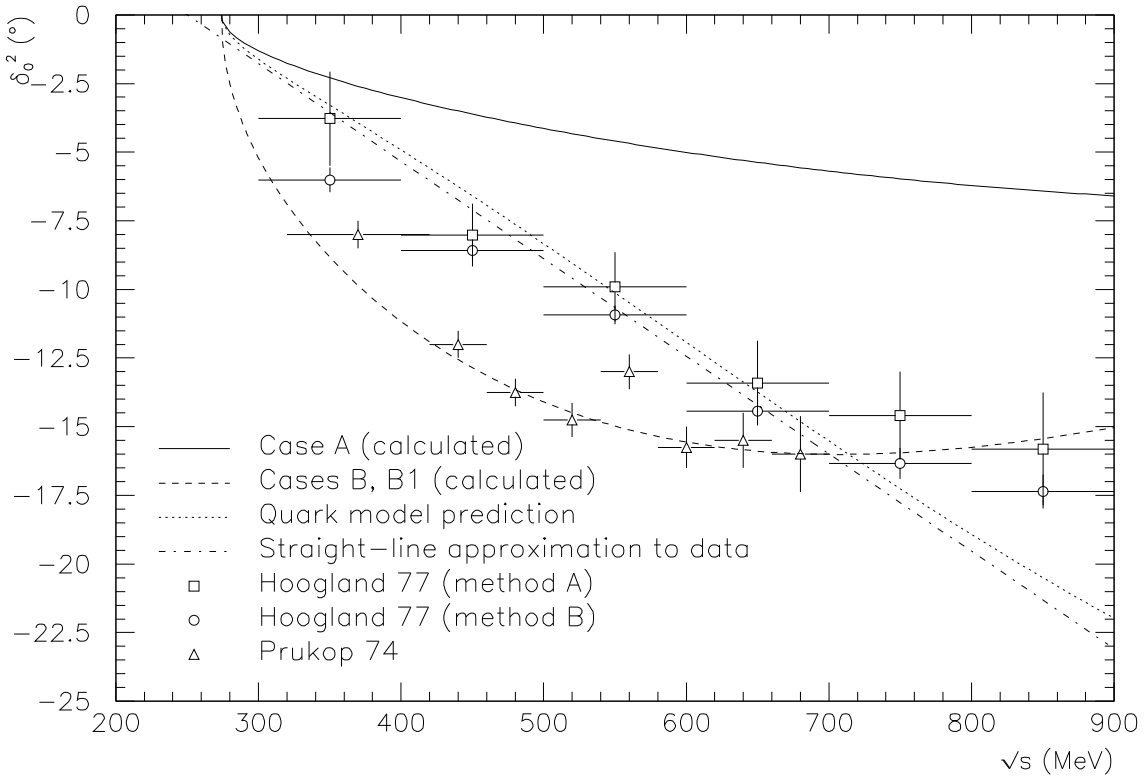


Figure 5.7: Graphs of the $I = 2 \pi\text{--}\pi$ scattering phase shift vs. \sqrt{s} , for our predictions, the quark model prediction, and experimental data. The data is from Hoogland *et al.* [58] – we show the results of both of their methods; and Prukop *et al.* [59] – we show the results of their first fit. For additional comments see Figure 5.1.

The $I = 0$ phase shifts are shown in Figure 5.8. Note the rather unfortunate behaviour of the phase shift for case B, which suggests that η and κ should not be used in the s-channel gluon exchange contribution to the potential. Since there is no *a priori* good reason for not using them in this part of the potential, we must question their use at all. However, we will continue to show the results arising from cases B and B1. Again, the phase shift for case A is poor, and for FSI corrections we will replace it with the curve arising directly from the quark model. Note that this time the quark model curve is low as well; the reason is as follows. When the quark model predictions for the $I = 0$ phase shifts were calculated [51] three contributions were considered: t-channel gluon exchange, s-channel gluon exchange, and contributions

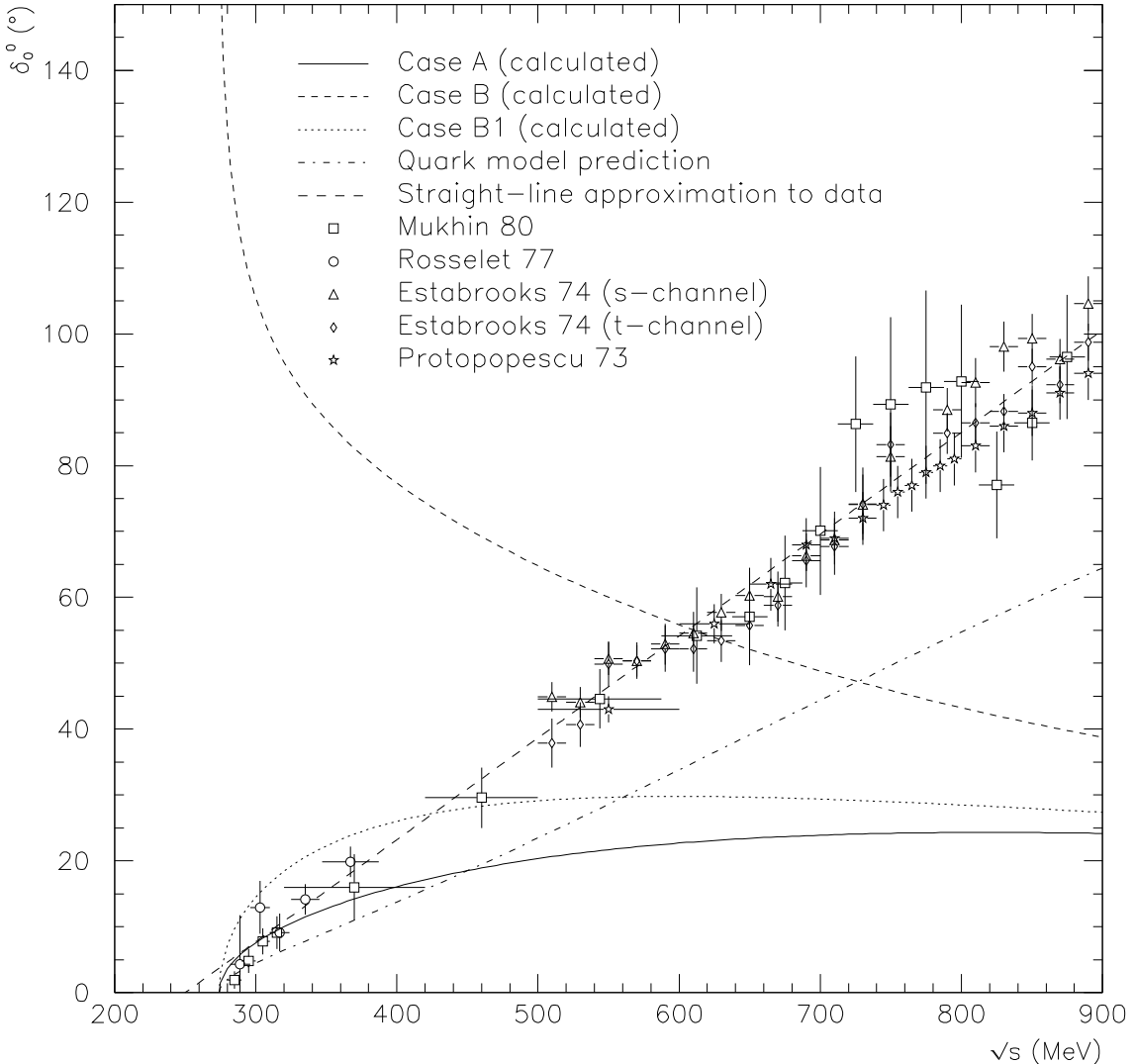


Figure 5.8: Graphs of the $I = 0$ $\pi\pi$ scattering phase shift vs. \sqrt{s} , for our predictions, the quark model prediction, and experimental data. The data is from Mukhin *et al.* [60]; Rosselet *et al.* [61] – the horizontal bars only approximate their bins, and their data is actually for $\delta_0^0 - \delta_1^1$ – we have used the δ_0^0 data extracted from it by Li *et al.* [51]; Estabrooks and Martin [62] – we show the results of both their s- and t-channel fits; and Protopopescu *et al.* [63] – we show the results of their case 1. For additional comments see Figure 5.1.

from interactions with the $f_0(980)$ and $f_0(1300)$ resonances. These contributions were fit to the data, but because we are not including resonance effects in this work, we only include the contributions from the s- and t-channel gluon exchange in our quark

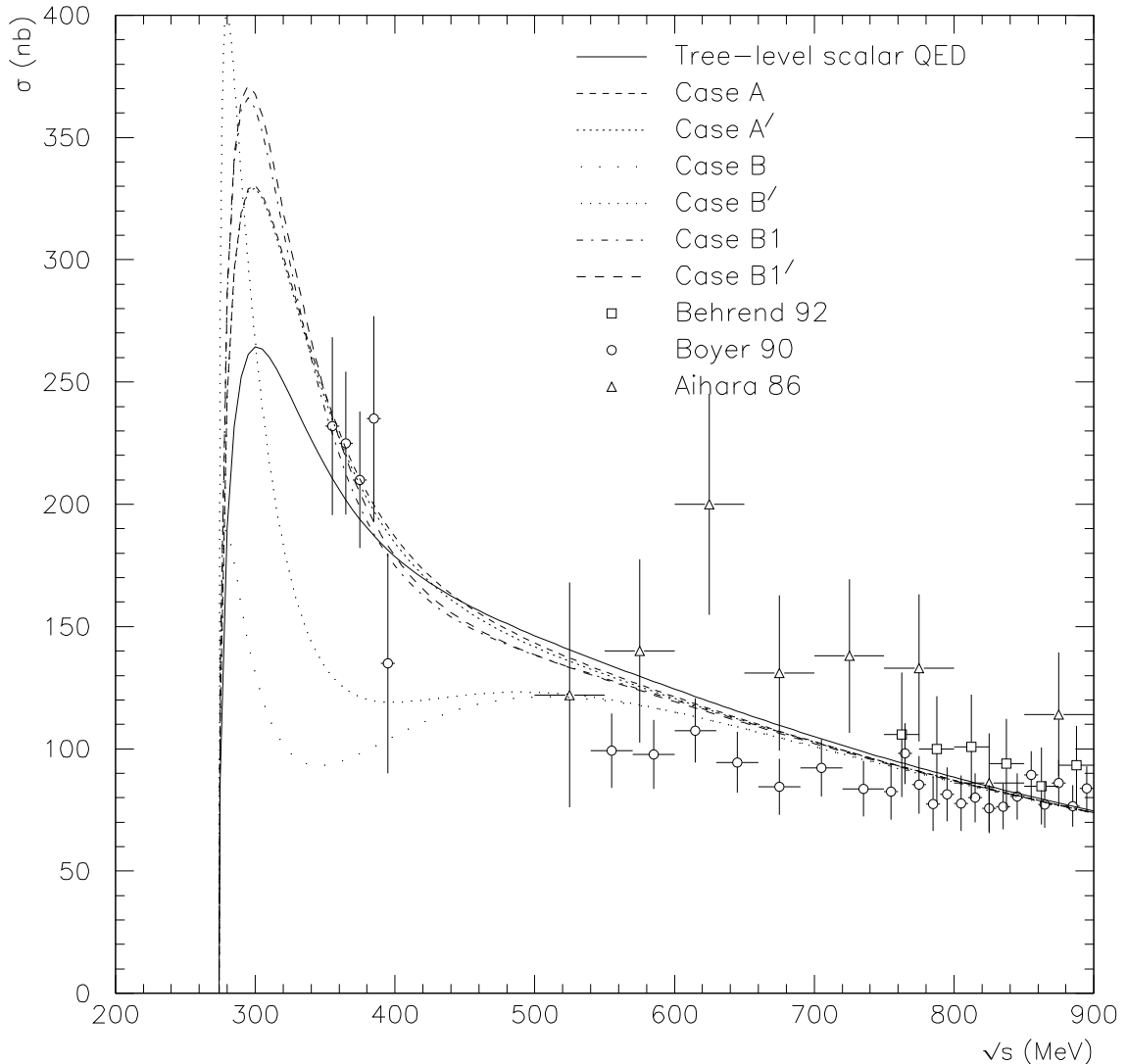


Figure 5.9: Graph of the $\gamma\gamma \rightarrow \pi^+\pi^-$ total cross-section vs. \sqrt{s} , for our predictions, the tree-level scalar QED prediction, and experimental data. The curves have been corrected to have a limited polar acceptance to match the data: $|\cos \theta| \leq 0.6$. For references to the data and additional comments see Figure 5.1.

model curve. When resonance effects are included, the quark model curve fits the data rather well. Again, the remaining curve shown is just a straight-line which we have used to describe the data for the primed cases.

Now let us look at the $\gamma\gamma \rightarrow \pi^+\pi^-$ cross-section results, shown in Figure 5.9. Cases A, A', B1 and B1' all fit the data well (as does the tree-level scalar QED

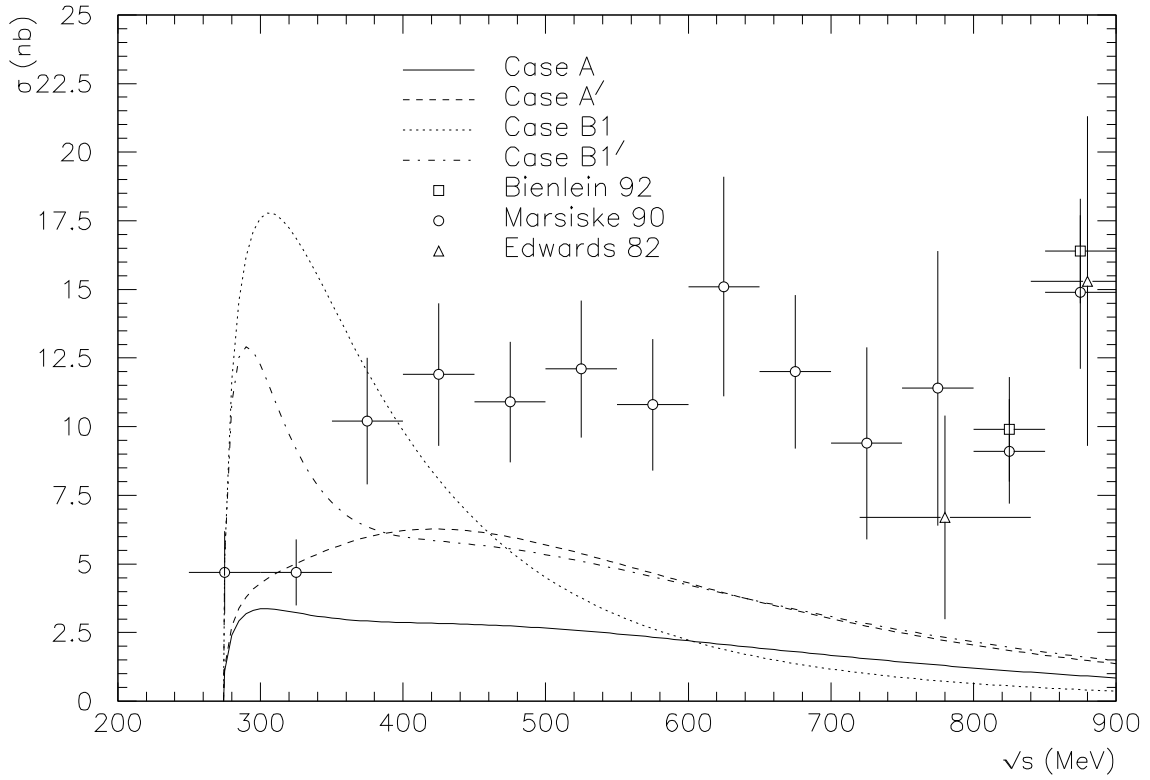


Figure 5.10: Graphs of the $\gamma\gamma \rightarrow \pi^0\pi^0$ cross-section vs. \sqrt{s} , for our predictions (cases A, A', B1 and B1') and experimental data. The data is from Bienlein (*et al.*) [64], Marsiske *et al.* [65] and Edwards *et al.* [66]. The data has been corrected to full polar acceptance: $|\cos \theta| \leq 1.0$. For additional comments see Figure 5.1.

prediction). The effects of using the quark model phase shifts are not significant for these cases. Better data would be needed to differentiate between case A, case B1 and the tree-level scalar QED prediction. Cases B and B' are disfavoured by the data, as might be expected from the poor performance of case B in predicting the phase shifts. Because that prediction differed drastically from the data, cases B and B' do differ appreciably in their predictions of the cross-section.

The $\gamma\gamma \rightarrow \pi^0\pi^0$ cross-section results are shown in Figures 5.10 and 5.11. Here our results do not do as well. This is partly because our $\gamma\gamma \rightarrow \pi^0\pi^0$ cross-section is wholly due to FSI's while in the $\gamma\gamma \rightarrow \pi^+\pi^-$ case the FSI effects are corrections to a more significant curve. This also means that the primed and unprimed cases

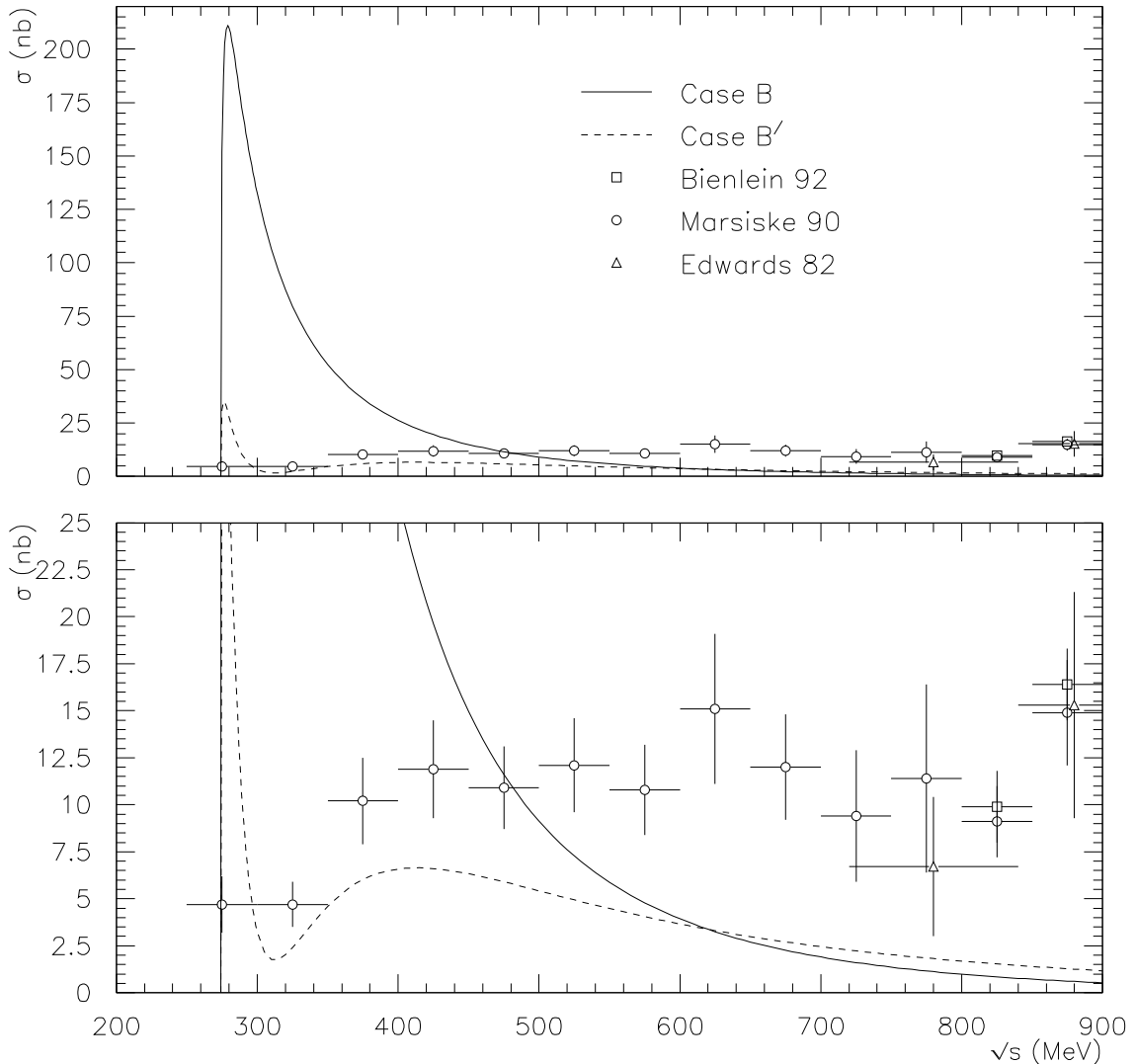


Figure 5.11: Graphs of the $\gamma\gamma \rightarrow \pi^0\pi^0$ cross-section vs. \sqrt{s} , for our predictions (cases B and B') and experimental data. The upper and lower plots differ only in their vertical scales. The data has been corrected to full polar acceptance: $|\cos\theta| \leq 1.0$. For references to the data see Figure 5.10. For additional comments see Figure 5.1.

differ substantially. None of our cases are consistent with the data. Cases B and B' do particularly badly as expected from our previous results. Of the others, case A' comes closest, being roughly a factor of 2 too low. It also shows a local maximum in the cross-section at higher energies, in keeping with the data. It is interesting to note that using the experimental phase shifts instead of the quark model predictions in

our expressions for the FSI corrections greatly improves curve A. Since the difference in these phase shifts is due to resonance effects, we tend to believe that including the effects of resonances in the wavefunction distortion as well would improve the curve still further.

We have demonstrated that the quark model can predict the $\gamma\gamma \rightarrow \pi^+\pi^-$ cross-section in agreement with experimental data when a sufficiently detailed calculation is performed. However, with the present potentials it is unable to accurately predict the $\gamma\gamma \rightarrow \pi^0\pi^0$ cross-section. We find that using Weinstein and Isgur's η and κ factors in the potentials is not helpful when calculating FSI effects; it is better to use the expressions for the phase shifts calculated directly in the quark model in the expressions for the FSI corrections. We believe that the next logical step in this program of work is to include potentials allowing the $I = 0$ $\pi\pi$ state to convert to the $f_0(980)$ and $f_0(1300)$ resonances (and back). This would mean solving a coupled-channel Schrödinger equation in the $I = 0$ channel.

Chapter 6

Conclusions

In this thesis we have examined three problems, split between two general areas of the quark model.

Both of the first two problems involved two models of meson decay: the $3P_0$ model and the flux-tube breaking model. We have developed general routines for these models that can be used for any OZI-allowed strong decay of a meson into two other mesons, as long as the radial portion of the meson wavefunctions can be expanded in terms of SHO radial wavefunctions, and sufficient computer resources are available. The general nature of these routines make them useful tools in the study of meson phenomenology.

While fitting the free parameter of the models and investigating a number of choices that must be made in their application, we evaluated the models by comparing their predictions for the decay widths of 28 of the best known meson decays to the experimental values. We found that these models are not very accurate – the best they can hope for is to predict a decay width to within a factor of 2, and even larger deviations are common. Since they are coarse models of a complicated theory, this is not surprising. We also found that both the use of SHO wavefunctions with the effective β 's of Kokoski and Isgur [5], and the use of nonrelativistic

phase space/normalization give less accurate results than can be obtained with other choices.

The first problem that we investigated was the identity of the $f_4(2220)$. Although tentatively identified as the 3F_4 $s\bar{s}$ meson by the Particle Data Group, its identity has been uncertain since its discovery in 1983. We carried out detailed calculations of the decays of the 3F_2 and 3F_4 $s\bar{s}$ mesons in order to see if a meson identification for the $f_4(2220)$ is tenable. Despite the uncertainties of the decay models, we found that the $f_4(2220)$, with a measured decay width of approximately 30 MeV, cannot be the 3F_2 $s\bar{s}$, whose width we expect to be $\gtrsim 400$ MeV. We expect the width of the 3F_4 $s\bar{s}$ meson to be $\gtrsim 140$ MeV and $\lesssim 600$ MeV, but the uncertainty of the models precludes us from ruling out the identification of the $f_4(2220)$ as the 3F_4 $s\bar{s}$ with any surety. We do feel it is unlikely however, and propose the following explanation: that the broad state seen in hadron beam experiments is the 3F_4 $s\bar{s}$ meson, and the narrow state seen in J/ψ radiative decay is a glueball. Further experimental data is needed to finally identify the $f_4(2220)$.

The second problem that we investigated was the determination of the mixing angle between the $K_1(1270)$ and $K_1(1400)$ mesons. This was done by comparing predictions of the meson decay models for five partial decay widths and two ratios of D to S amplitudes with experimental data. We found the mixing angle θ_K to be approximately 44° . If the mixing is due only to the spin-orbit interactions already included in the quark model of Godfrey and Isgur, then this implies that the responsible term in the Hamiltonian, $\langle H_{q\bar{q}}^{\text{SO-}} \rangle$, has a value far larger than calculated. However, because of the delicate cancellation that leads to the small calculated value, we are unable to draw any conclusions about whether the mixing is largely due to another mechanism, or the quark model Hamiltonian just needs retuning somewhat.

The third problem that we investigated was the effect of the strong final state interactions (FSI's) in the reaction $\gamma\gamma \rightarrow \pi\pi$ near threshold. Using effective potentials

extracted from a quark model, we found that our preferred set of potentials (without the η and κ correction factors) successfully described the experimental data for the $\gamma\gamma \rightarrow \pi^+\pi^-$ cross-section. However, the prediction in the absence of FSI's also described the data, so better data is need to distinguish between the two. This still represents a vindication for the use of effective potentials extracted from a quark model, which has been in disrepute because the latest data does not agree with the results of a previous, less-comprehensive calculation. We were also able to conclude that the use of Weinstein and Isgur's η and κ correction factors for the potentials is inappropriate for the calculation of FSI effects.

Unfortunately, we were unable to reproduce the data for the $\gamma\gamma \rightarrow \pi^0\pi^0$ cross-section. This is partly because the $\gamma\gamma \rightarrow \pi^0\pi^0$ cross-section is wholly due to FSI's while in the $\gamma\gamma \rightarrow \pi^+\pi^-$ case the FSI effects are corrections to a more significant quantity. However, we have indications that including the effects of resonance production in the $I = 0$ channel may bring our results in line with the data. The next step in our program would be to solve a coupled-channel Schrödinger equation to include these effects. In light of our poor results for the $\gamma\gamma \rightarrow \pi^0\pi^0$ cross-section, it would be premature to investigate the structures seen in the cross-sections of $\gamma\gamma \rightarrow$ two vector mesons at this time.

Appendix A

Some Tools of Particle Physics

In this appendix we introduce some of the terms and tools of particle physics, to help specialists in other fields in understanding the work of this thesis. For an excellent introduction to the field, see Griffiths [67].

A.1 Cross-section and Width

In most particle physics experiments two particles are collided and the outgoing particles are collected and identified. Due to the interactions between the particles, they may be scattered in different directions, and/or they may be transformed into other particles. The probability of a particular reaction occurring is related to the cross-section σ which is a function of the total energy of the particles and is measured in units of barns, or b ($1 \text{ b} = 10^{-28} \text{ m}^2$).

A particle will decay eventually if there is an interaction that permits it to be transformed into other particles with less total mass. The average lifetime of the particle is denoted by τ ; by Heisenberg's uncertainty principle, this finite lifetime leads to an uncertainty in the mass of the particle. In a collision of two particles, the production of a short-lived particle in the intermediate state (which then decays

to give the final state particles) shows up in the cross-section plot as a resonance described by a Breit-Wigner curve with width $\Gamma = 1/\tau$ (see for example Figure 3.7).

For a particle that can decay into two or more different final states we can define its branching ratios, which are the probabilities that the particle will decay into the various final states. From these we can define the partial width for a particular decay mode as the product of the branching ratio for that mode, and the total width. The sum of all the partial widths gives the total width, which is what is used to get the particle's average lifetime. We may sometimes refer to a partial width as the width for a particular decay mode.

Similarly for the cross-section for a particular initial state, there are the cross-sections going to specific final states, which sum to give the total cross-section. Note that in a plot of the cross-section to a specific final state, a resonance in the intermediate state still produces a Breit-Wigner curve with a width equal to the total width for that resonance. (Even though we are only looking at a particular decay mode, the lifetime of the resonance is still that determined by all of the possible decay modes.)

A.2 Feynman Diagrams

In a perturbation theory such as that normally used to calculate quantities in QED, each order of perturbation is represented by Feynman diagrams, such as those shown in Figure 5.2 for $\gamma\gamma \rightarrow \pi^+\pi^-$ in scalar QED. In a Feynman diagram the particles are represented by lines, and basic interactions by vertices where a number of lines meet. Since for QED each vertex corresponds to another factor of $\sqrt{\alpha}$ in the Feynman amplitude¹ the order of the perturbation is given by the number of vertices in the diagram.

¹The Feynman amplitude is similar to the amplitude of quantum mechanics. Its magnitude squared is combined with the phase space of the final state particles to obtain the cross-section or width.

A tree-level diagram is one in which there is only one path of lines connecting any two vertices (i.e. there are no loops). For QED at least, if a tree-level diagram exists for a particular process then it is the lowest order diagram.

A.3 Clebsch-Gordan Coefficients and the Wigner nj Symbols

An angular momentum state, be it spin, orbital angular momentum, or a vector sum of some combination of these, is represented (in an SU(2) algebra) by the usual quantum numbers $|jm\rangle$ where the magnitude of the total angular momentum is $\sqrt{j(j+1)}$ and the z -component is m . To combine two angular momentum states we use the Clebsch-Gordan coefficients, defined by

$$|j_1 m_1\rangle |j_2 m_2\rangle \equiv \sum_{j=|j_1-j_2|}^{j_1+j_2} \langle j_1 m_1 j_2 m_2 | JM \rangle |JM\rangle \quad (\text{A.1})$$

where $\langle j_1 m_1 j_2 m_2 | JM \rangle$ is the Clebsch-Gordan coefficient and $M = m_1 + m_2$.

The Wigner $3j$ symbol is related to the Clebsch-Gordan coefficient by

$$\begin{pmatrix} j_1 & j_2 & J \\ m_1 & m_2 & -M \end{pmatrix} \equiv \frac{(-1)^{j_1-j_2+M}}{\sqrt{2J+1}} \langle j_1 m_1 j_2 m_2 | JM \rangle. \quad (\text{A.2})$$

The Wigner $6j$ symbol

$$\left\{ \begin{array}{ccc} j_1 & j_2 & j_3 \\ J_1 & J_2 & J_3 \end{array} \right\}$$

is used to combine three angular momentum states, and the Wigner $9j$ symbol

$$\left\{ \begin{array}{ccc} j_1 & j_2 & J_{12} \\ j_3 & j_4 & J_{34} \\ J_{13} & J_{24} & J \end{array} \right\}$$

is used to combine four angular momentum states. We will not define these here, though the $9j$ symbol is defined in Appendix D.3. For more information, see for example Reference [34].

A.4 Conservation Laws and Invariance Principles

Because of symmetries in the theories of the interactions, the interactions themselves obey a number of conservation laws and invariance principles (see for example Reference [54]). We will only discuss the ones of interest here.

There is the usual conservation of energy, momentum, angular momentum and charge.

If one thinks of an antiparticle as being -1 particles, then the numbers of leptons and quarks are separately conserved as well – this is enforced by the allowed interaction vertices (e.g. if an e^+e^- pair is created, the change in lepton number is $(-1) + (+1) = 0$).

Because the strong interaction is independent of the type of quark involved, and the u and d quarks have very similar masses, we can think of them as different projections of the same state which we represent by the angular momentum-like quantity called isospin (where $u = |\frac{1}{2} \frac{1}{2}\rangle$ and $d = |\frac{1}{2} -\frac{1}{2}\rangle$). Isospin is conserved in the strong interaction to the extent that the masses of the u and d quarks are degenerate.

The spin-statistics theorem governs how systems of identical particles behave when two of the particles are exchanged (boson wavefunctions are unaffected, fermion

wavefunctions pick up a factor of -1). It is important that the wavefunctions we construct obey these symmetries. In the context of the strong interactions, members of the same isospin multiplet also obey the spin-statistics theorem, even though they are not strictly identical.

The parity of a system indicates how the wavefunction behaves under the space inversion $\vec{r} \rightarrow -\vec{r}$; the wavefunction is either unchanged ($\mathcal{P} = +1$) or picks up a factor of -1 ($\mathcal{P} = -1$). The total parity of a system is conserved in the electromagnetic and strong interactions, but not the weak interaction.

Under the charge conjugation operator, particles are changed to their antiparticles (and vice versa). Systems which are eigenstates of \mathcal{C} (such as π^0 , or the $\pi^+\pi^-$ system) may have $\mathcal{C} = +1$ or -1 . Charge conjugation is also conserved in the electromagnetic and strong interactions, but not the weak interaction. Charge conjugation can be extended by combining it with isospin to get G-parity, which is conserved in the strong interaction only.

A.5 Relative Coordinates

The wavefunction of two particles in position-space depends on the coordinates of the two particles, \vec{r}_1 and \vec{r}_2 . When solving the Schrödinger equation it is convenient to separate it into equations involving the centre of mass (CM) coordinate of the particles, R , and their relative coordinate r :

$$\begin{aligned} \vec{R} &= \frac{m_1 \vec{r}_1 + m_2 \vec{r}_2}{m_1 + m_2} & \iff & \vec{r}_1 &= \vec{R} + \frac{m_2}{m_1 + m_2} \vec{r} \\ \vec{r} &= \vec{r}_1 - \vec{r}_2 & & \vec{r}_2 &= \vec{R} - \frac{m_1}{m_1 + m_2} \vec{r} \end{aligned} \quad (A.3)$$

The conjugate momenta \vec{p}_1 and \vec{p}_2 , and \vec{P} and \vec{p} , are related by:

$$\begin{aligned}\vec{P} &= \vec{p}_1 + \vec{p}_2 & \vec{p}_1 &= \frac{m_1}{m_1 + m_2} \vec{P} + \vec{p} \\ \vec{p} &= \frac{m_2 \vec{p}_1 - m_1 \vec{p}_2}{m_1 + m_2} & \vec{p}_2 &= \frac{m_2}{m_1 + m_2} \vec{P} - \vec{p}\end{aligned}\quad (\text{A.4})$$

This is a nonrelativistic construction: p remains unchanged when both particles are given the same velocity boost only for nonrelativistic velocities.

The CM frame refers to the inertial reference frame in which $\vec{P} = 0$; i.e. in which the centre of mass of the system is motionless.

A.6 The OZI Rule

Okubo, Zweig and Iizuka (OZI) noticed that QCD interactions in which all of the initial quarks are annihilated, and are not present in the final state, are suppressed. This is thought to be because for interactions of this type, asymptotic freedom means that the strong coupling constant α_s (which enters the cross-section as at least α_s^4) becomes small since all of the energy of the initial state particles must be included in the momentum transferred through the gluons (see for example Reference [68]).

A.7 Meson Mixings

Particles with the same “good” quantum numbers (i.e. a complete set of commuting observables) “mix” if there exists an interaction through which one particle can be transformed into the other, and vice versa. For example, the strange mesons $(-u\bar{s}, -d\bar{s}, -s\bar{d}, s\bar{u})$ with states 1P_1 and 3P_1 only differ in the sum of the quark spins, and can mix via the spin-orbit interaction (and possibly others) to produce the physical states $K_1(1270)$ and $K_1(1400)$. Another example is found in the flavour

wavefunctions: the $u\bar{u}$, $d\bar{d}$ and $s\bar{s}$ are all flavourless (since the flavour of the u cancels that of the \bar{u}) and so there is nothing to prevent the flavour states in a 1S_0 spin/space state (for example) from mixing by an annihilation interaction to produce the physical states π^0 , η and η' .

By mix, we mean that the basis of quantum number states (e.g. $K({}^1P_1)$ and $K({}^3P_1)$) differs from the basis of the physical states (e.g. $K_1(1270)$ and $K_1(1400)$). When we are only talking about two states, we can represent the mixing by a rotation:

$$\begin{pmatrix} K_1(1270)^+ \\ K_1(1400)^+ \end{pmatrix} = \begin{pmatrix} \cos \theta & \sin \theta \\ -\sin \theta & \cos \theta \end{pmatrix} \begin{pmatrix} K({}^1P_1)^+ \\ K({}^3P_1)^+ \end{pmatrix}. \quad (\text{A.5})$$

For this particular mixing, we take $\theta = 45^\circ$ [1] for the calculations of Section 3.2. In Section 3.3, we attempt to determine this mixing angle by comparing predictions of meson decay models to experimental data.

In terms of the amplitudes and widths, Eq. E.2 becomes with mixing, using a decay involving the $K_1(1270)^+$ for example,

$$\Gamma_{K_1(1270)^+}^{SL} = \frac{\pi}{4} \frac{P\mathcal{S}}{M_A^2} |M_{K_1(1270)^+}^{SL}|^2 = \frac{\pi}{4} \frac{P\mathcal{S}}{M_A^2} |\cos \theta M_{K({}^1P_1)^+}^{SL} + \sin \theta M_{K({}^3P_1)^+}^{SL}|^2. \quad (\text{A.6})$$

In Eq. A.5, note that we specified the positively charged mesons, because the flavour makes a difference to the mixing angle for these particular mesons. This comes about in the quark model Hamiltonian – the term that causes the mixing, $\langle H_{q\bar{q}}^{SO-} \rangle$, changes sign when the antiquark instead of the quark is the heavier strange, and this leads to a mixing angle of opposite sign when the 1P_1 – 3P_1 Hamiltonian is diagonalized (see Eqs. 3.3 and 3.4). Thus if we have a mixing angle of 45° for the $K_1(1270)^+$ and $K_1(1400)^+$ (and $K_1(1270)^0$ and $K_1(1400)^0$), we must use -45° for the $K_1(1270)^-$ and $K_1(1400)^-$ (and $\bar{K}_1(1270)^0$ and $\bar{K}_1(1400)^0$).

The other meson mixing that we use in this work² is due to the tensor part of the colour-hyperfine interaction [4]:

$$\begin{pmatrix} K^*(1410) \\ K^*(1680) \end{pmatrix} = \begin{pmatrix} 1.00 & 0.04 \\ -0.04 & 1.00 \end{pmatrix} \begin{pmatrix} K(2^3S_1) \\ K(1^3D_1) \end{pmatrix}. \quad (\text{A.7})$$

²We did initially consider similar mixings of other mesons, but the widths of the decays involving these mesons were too small to be included in our results.

Appendix B

Meson Wavefunctions Used in this Work

As can be seen from Eq. 2.1, meson wavefunctions contain four different component wavefunctions: space, spin, flavour and colour. The space and flavour wavefunctions are given below. The spin wavefunctions are given in Appendix D.3. The colour wavefunction is trivially a colour singlet (see Appendix D.1).

B.1 Space Wavefunctions

In this work we investigate three different sets of meson space wavefunctions, though only two are used for calculations. All three are expressed in terms of simple harmonic oscillator (SHO) wavefunctions. In momentum-space the SHO wavefunctions are

$$\psi_{nLM_L}^{\text{SHO}}(\vec{p}) = R_{nL}^{\text{SHO}}(p) Y_{LM_L}(\Omega_p) \quad (\text{B.1})$$

where the radial wavefunctions are given by

$$R_{nL}^{\text{SHO}}(p) = \frac{(-1)^n(-i)^L}{\beta^{\frac{3}{2}}} \sqrt{\frac{2 n!}{\Gamma(n+L+\frac{3}{2})}} \left(\frac{p}{\beta}\right)^L e^{-p^2/(2\beta^2)} L_n^{L+\frac{1}{2}}(p^2/\beta^2), \quad (\text{B.2})$$

the oscillator parameter β contains all the parameters of the Hamiltonian, and $L_n^{L+\frac{1}{2}}(p^2/\beta^2)$ is an associated Laguerre polynomial. The quantum numbers n and L are unrelated, and have the ranges: n : 0,1,2,..., and L : 0,1,2,...

In position-space we have the Fourier transform of the above,

$$\psi_{nLM_L}^{\text{SHO}}(\vec{r}) = R_{nL}^{\text{SHO}}(r) Y_{LM_L}(\Omega_r), \quad (\text{B.3})$$

where the radial wavefunctions are given by

$$R_{nL}^{\text{SHO}}(r) = \beta^{\frac{3}{2}} \sqrt{\frac{2 n!}{\Gamma(n+L+\frac{3}{2})}} (\beta r)^L e^{-\beta^2 r^2/2} L_n^{L+\frac{1}{2}}(\beta^2 r^2). \quad (\text{B.4})$$

In some cases it may be convenient to pull the p^L or r^L out of the radial wavefunction, and associate it with the spherical harmonic to create a solid harmonic.

The first set of meson space wavefunctions that we use for this work are just the SHO wavefunction with the same L and M_L as the meson, and the same degree of radial excitation (so a meson in its radial ground state, normally denoted with $n = 1$ in the $n^{2S+1}L_J$ spectroscopic notation, uses $\psi_{n=0,LM_L}^{\text{SHO}}$). The oscillator parameter β is taken to be the same for all mesons, and we examine the choice of it in Section 3.1. SHO wavefunctions are expected to be coarse approximations to the true wavefunctions, since they neglect all but the linear confining part of the meson potential, and that they only approximate. However, they are qualitatively similar, and are useful for generating analytical results.

The second set of meson space wavefunctions that we use are those of Godfrey and Isgur [4], calculated in the highly successful relativized quark model described

in Section 1.2.2. We will label these wavefunctions by RQM. The radial parts of these wavefunctions are expressed as linear combinations of the first $N + 1$ radial SHO wavefunctions (as in Eq. 2.9), where N was chosen to give a good description of the particular wavefunction. The oscillator parameter was fit individually for each meson, and the quark masses were also fitted: $m_u = 220$ MeV, $m_d = 220$ MeV, and $m_s = 419$ MeV.

The third set of meson space wavefunctions that we use are single SHO wavefunctions like the first set, but with the effective oscillator parameters (different for each meson) of Kokoski and Isgur [5]. The effective parameters were obtained by fitting the rms momenta of the SHO wavefunctions to be equal to those obtained from the second set of wavefunctions. We do not use this third set of wavefunctions for actual calculations because of their poor performance in Section 3.1.

B.2 Flavour Wavefunctions

We use the following meson flavour wavefunctions in this work:

For the isovectors:

$$\begin{aligned}\pi^+ &= -u\bar{d} \\ \pi^0 &= \frac{1}{\sqrt{2}}(u\bar{u} - d\bar{d}) \\ \pi^- &= d\bar{u}.\end{aligned}$$

For the strange mesons:

$$\begin{aligned}K^+ &= -u\bar{s} \\ K^0 &= -d\bar{s} \\ \bar{K}^0 &= -s\bar{d}\end{aligned}$$

$$K^- = s\bar{u}.$$

For the isoscalars we assumed “ideal mixing”,

$$\begin{aligned}\phi_{\text{nonstrange}} &= \frac{1}{\sqrt{2}}(u\bar{u} + d\bar{d}) \\ \phi_{\text{strange}} &= s\bar{s},\end{aligned}$$

except for the pseudoscalars in a radial ground state, where we assumed “perfect mixing”,

$$\begin{aligned}\eta &= \frac{1}{\sqrt{2}}(\phi_{\text{nonstrange}} - \phi_{\text{strange}}) = \frac{1}{2}(u\bar{u} + d\bar{d}) - \frac{1}{\sqrt{2}}s\bar{s} \\ \eta' &= \frac{1}{\sqrt{2}}(\phi_{\text{nonstrange}} + \phi_{\text{strange}}) = \frac{1}{2}(u\bar{u} + d\bar{d}) + \frac{1}{\sqrt{2}}s\bar{s}.\end{aligned}$$

In terms of the SU(3) flavour representation [1],

$$\begin{aligned}\eta &= \eta_8 \cos \theta_P - \eta_1 \sin \theta_P \\ \eta' &= \eta_8 \sin \theta_P + \eta_1 \cos \theta_P\end{aligned}$$

where

$$\begin{aligned}\eta_1 &= \sqrt{\frac{2}{3}}\phi_{\text{nonstrange}} + \frac{1}{\sqrt{3}}\phi_{\text{strange}} \\ \eta_8 &= \frac{1}{\sqrt{3}}\phi_{\text{nonstrange}} - \sqrt{\frac{2}{3}}\phi_{\text{strange}},\end{aligned}$$

ideal mixing corresponds to $\theta_P = -54.7^\circ$, while perfect mixing corresponds to $\theta_P = -9.7^\circ$. The latter number is consistent with the angle obtained from the η – η' mass matrix, while data from decay to two photons suggests $\theta_P \simeq -20^\circ$ [1]. The use of this second value is considered in Chapter 3.

Appendix C

Field Theory Conventions Used in this Work

We use the following field theory conventions in this work:

For the spinor normalizations,

$$\begin{aligned} u^{(\alpha)\dagger}(p) u^{(\beta)}(p) &= v^{(\alpha)\dagger}(p) v^{(\beta)}(p) = \frac{E}{m} \delta_{\alpha\beta} \\ u^{(\alpha)\dagger}(p) v^{(\beta)}(\bar{p}) &= v^{(\alpha)\dagger}(p) u^{(\beta)}(\bar{p}) = 0, \end{aligned}$$

where if $p = (E, \vec{p})$, then $\bar{p} \equiv (E, -\vec{p})$.

We define the spinor field

$$\Psi(x) = \sum_{\alpha} \int \frac{d^3 \vec{p}}{(2\pi)^{\frac{3}{2}}} \sqrt{\frac{m}{E}} [b_{\alpha}(p) u^{(\alpha)}(p) e^{-ip \cdot x} + d_{\alpha}^{\dagger}(p) v^{(\alpha)}(p) e^{ip \cdot x}],$$

and use the anticommutators

$$\begin{aligned} \{\Psi_i(t, \vec{x}), \Psi_j^{\dagger}(t, \vec{x}')\} &= \delta^3(\vec{x} - \vec{x}') \delta_{ij} \\ \{\Psi_i(t, \vec{x}), \Psi_j(t, \vec{x}')\} &= \{\Psi_i^{\dagger}(t, \vec{x}), \Psi_j^{\dagger}(t, \vec{x}')\} = 0 \end{aligned}$$

$$\begin{aligned}
 \{b_\alpha(p), b_{\alpha'}^\dagger(p')\} &= \{d_\alpha(p), d_{\alpha'}^\dagger(p')\} = \delta^3(\vec{p} - \vec{p}') \delta_{\alpha\alpha'} \\
 \{b_\alpha(p), b_{\alpha'}(p')\} &= \{d_\alpha(p), d_{\alpha'}(p')\} = 0 \\
 \{b_\alpha^\dagger(p), b_{\alpha'}^\dagger(p')\} &= \{d_\alpha^\dagger(p), d_{\alpha'}^\dagger(p')\} = 0,
 \end{aligned}$$

which gives for the normalization of one particle states

$$\langle b_\alpha(p) | b_{\alpha'}(p') \rangle = \langle d_\alpha(p) | d_{\alpha'}(p') \rangle = \delta^3(\vec{p} - \vec{p}') \delta_{\alpha\alpha'}.$$

Appendix D

Evaluating the Colour, Flavour and Spin Overlaps for Models of Meson Decay

In the 3P_0 and flux-tube breaking models of meson decay, the overlaps of the colour, flavour, spin and space wavefunctions of the mesons and the created pair must be calculated. The overlap of the space wavefunctions is accomplished by the integrals of Eqs. 2.8 and 2.23. The other overlaps are discussed below.

D.1 Colour Overlap

The calculation of the colour overlap is particularly simple, because the mesons and the created pair are all colour singlets, with the wavefunction $\omega = \frac{1}{\sqrt{3}}(R\bar{R}+G\bar{G}+B\bar{B})$ (using the arbitrary three colours Red, Green, Blue).

This may be represented in matrix form (this may seem excessive now, but will

be useful for the flavour overlaps as well) by

$$\omega = \frac{1}{\sqrt{3}} \begin{pmatrix} 1 & 0 & 0 \\ 0 & 1 & 0 \\ 0 & 0 & 1 \end{pmatrix} \quad (\text{D.1})$$

where the rows indicate a quark of colour R, G, B , and the columns indicate anti-quarks of color $\bar{R}, \bar{G}, \bar{B}$.

Consider a simple case with only one meson on each side, $\langle \omega_A^{12} | \omega_B^{12} \rangle$. The superscripts indicate that the quark of A (labelled 1) is also the quark of B , and similarly for the antiquark (labelled 2). A particular colour combination (e.g. $R\bar{R}$) will only contribute to the overlap if it is found on both sides of the bra-ket, and the resulting term is just the product of the coefficients in the matrices for that colour combination. Then the total result is just the sum of these terms over the possible colours,

$$\langle \omega_A^{12} | \omega_B^{12} \rangle = \sum_{c_1, c_2} (\omega_A)_{c_1 c_2} (\omega_B)_{c_1 c_2} = \sum_{c_1, c_2} (\omega_A)_{c_1 c_2} (\omega_B^T)_{c_2 c_1} = \text{Tr}[\omega_A \omega_B^T], \quad (\text{D.2})$$

where c_1 (c_2) runs over the quark (antiquark) colours.

This is easily expanded to the case where there are two mesons on each side (e.g. for the first diagram of Figure 2.1):

$$\begin{aligned} \langle \omega_B^{14} \omega_C^{32} | \omega_A^{12} \omega_0^{34} \rangle &= \sum_{c_1, c_2, c_3, c_4} (\omega_B)_{c_1 c_4} (\omega_C)_{c_3 c_2} (\omega_A)_{c_1 c_2} (\omega_0)_{c_3 c_4} \\ &= \sum_{c_1, c_2, c_3, c_4} (\omega_A^T)_{c_2 c_1} (\omega_B)_{c_1 c_4} (\omega_0^T)_{c_4 c_3} (\omega_C)_{c_3 c_2} = \text{Tr}[\omega_A^T \omega_B \omega_0^T \omega_C]. \end{aligned} \quad (\text{D.3})$$

For the case where everything is a colour singlet, the results are

$$\langle \omega_B^{14} \omega_C^{32} | \omega_A^{12} \omega_0^{34} \rangle = \langle \omega_B^{32} \omega_C^{14} | \omega_A^{12} \omega_0^{34} \rangle = \frac{1}{3}. \quad (\text{D.4})$$

D.2 Flavour Overlap

The overlap of the flavour wavefunctions of the mesons and the created pair can be calculated using the matrix notation introduced in Appendix D.1. The flavour of a meson may be represented by a matrix where the rows indicate a quark of flavour u , d , s, \dots and the columns indicate antiquarks of color \bar{u} , \bar{d} , \bar{s}, \dots For example, consider the π^0 ,

$$\phi_{\pi^0} = \frac{1}{\sqrt{2}}(u\bar{u} - d\bar{d}) = \frac{1}{\sqrt{2}} \begin{pmatrix} 1 & 0 & 0 \\ 0 & -1 & 0 \\ 0 & 0 & 0 \end{pmatrix}, \quad (\text{D.5})$$

and the K^+ ,

$$\phi_{K^+} = -u\bar{s} = \begin{pmatrix} 0 & 0 & -1 \\ 0 & 0 & 0 \\ 0 & 0 & 0 \end{pmatrix}. \quad (\text{D.6})$$

The 3P_0 and flux-tube breaking models assume that the pair is created in an $SU(N)$ flavour singlet; we take $N = 3$, since we are not concerned with any mesons involving c, b or t quarks:

$$\phi_0 = \frac{1}{\sqrt{3}}(u\bar{u} + d\bar{d} + s\bar{s}) = \frac{1}{\sqrt{3}} \begin{pmatrix} 1 & 0 & 0 \\ 0 & 1 & 0 \\ 0 & 0 & 1 \end{pmatrix}. \quad (\text{D.7})$$

Taking N to be some other number would change the value of γ (γ_0) needed to fit the data (because of the normalization in Eq. D.7), but would not change the calculated decay widths.

The overlap is given by expressions similar to Eq. D.3:

$$\langle \phi_B^{14} \phi_C^{32} | \phi_A^{12} \phi_0^{34} \rangle = \text{Tr}[\phi_A^T \phi_B \phi_0^T \phi_C] = \frac{1}{\sqrt{3}} \text{Tr}[\phi_A^T \phi_B \phi_C] \quad (\text{D.8})$$

$$\langle \phi_B^{32} \phi_C^{14} | \phi_A^{12} \phi_0^{34} \rangle = \text{Tr}[\phi_A^T \phi_C \phi_0^T \phi_B] = \frac{1}{\sqrt{3}} \text{Tr}[\phi_A^T \phi_C \phi_B]. \quad (\text{D.9})$$

In many cases only one of these overlaps will be non-zero.

As an example, consider the flavour overlaps in the decay $K^*(892)^+ \rightarrow K^+ \pi^0$; $\phi_{K^*(892)^+} = \phi_{K^+}$, giving us

$$\begin{aligned} \langle \phi_B^{14} \phi_C^{32} | \phi_A^{12} \phi_0^{34} \rangle &= 0 \\ \langle \phi_B^{32} \phi_C^{14} | \phi_A^{12} \phi_0^{34} \rangle &= \frac{1}{\sqrt{6}}. \end{aligned} \quad (\text{D.10})$$

D.3 Spin Overlap

Since quarks have spin $\frac{1}{2}$, their spins may only combine to give 0 or 1 in a meson. They combine in the usual singlet and triplet states (given as e.g. $|S_A M_{S_A}\rangle$):

$$\begin{aligned} |00\rangle &= \frac{1}{\sqrt{2}} [|\frac{1}{2}\frac{1}{2}\rangle |\frac{1}{2}-\frac{1}{2}\rangle - |\frac{1}{2}-\frac{1}{2}\rangle |\frac{1}{2}\frac{1}{2}\rangle] \\ \left\{ \begin{array}{lcl} |11\rangle &= & |\frac{1}{2}\frac{1}{2}\rangle |\frac{1}{2}\frac{1}{2}\rangle \\ |10\rangle &= & \frac{1}{\sqrt{2}} [|\frac{1}{2}\frac{1}{2}\rangle |\frac{1}{2}-\frac{1}{2}\rangle + |\frac{1}{2}-\frac{1}{2}\rangle |\frac{1}{2}\frac{1}{2}\rangle] \\ |1-1\rangle &= & |\frac{1}{2}-\frac{1}{2}\rangle |\frac{1}{2}-\frac{1}{2}\rangle \end{array} \right. \end{aligned} \quad (\text{D.11})$$

The overlap of the spin wavefunctions of the mesons and the created pair can be calculated by angular momentum algebra. It can be expanded in a sum over possible total spins (e.g. for the first diagram of Figure 2.1)

$$\begin{aligned} \langle \chi_{S_B M_{S_B}}^{14} \chi_{S_C M_{S_C}}^{32} | \chi_{S_A M_{S_A}}^{12} \chi_{1-m}^{34} \rangle &= \\ \sum_{S, M_S} \langle (j_1 j_4) S_B, (j_3 j_2) S_C; S M_S | (j_1 j_2) S_A, (j_3 j_4) 1; S M_S \rangle \\ \times \langle S_B M_{S_B} S_C M_{S_C} | S M_S \rangle \langle S_A M_{S_A} 1-m | S M_S \rangle \end{aligned} \quad (\text{D.12})$$

where the j_i 's are all $\frac{1}{2}$, but are necessarily written this way to show the connection between the left and right sides of the first factor. The first factor is a transformation between two different bases for combining four angular momenta, and is independent of M_S . On the left side, j_1 and j_4 are added together to obtain S_B , which is added to S_C to obtain S – a similar procedure is carried out on the right side. The $9j$ symbol is defined in terms of this transformation,

$$\begin{aligned} & \langle (j_1 j_4) J_{14}, (j_3 j_2) J_{32}; JM | (j_1 j_2) J_{12}, (j_3 j_4) J_{34}; JM \rangle = & (D.13) \\ & (-1)^{2J_{12}+2J_{14}+j_2-j_4+J_{32}-J_{34}} \sqrt{(2J_{12}+1)(2J_{34}+1)(2J_{14}+1)(2J_{32}+1)} \\ & \times \left\{ \begin{array}{ccc} j_1 & j_2 & J_{12} \\ j_4 & j_3 & J_{34} \\ J_{14} & J_{32} & J \end{array} \right\}, \end{aligned}$$

which allows us to write the spin overlap in terms of a $9j$ symbol:

$$\begin{aligned} & \langle \chi_{S_B M_{S_B}}^{14} \chi_{S_C M_{S_C}}^{32} | \chi_{S_A M_{S_A}}^{12} \chi_{1-m}^{34} \rangle = \\ & (-1)^{S_C+1} \sqrt{3(2S_A+1)(2S_B+1)(2S_C+1)} \sum_{S, M_S} \langle S_B M_{S_B} S_C M_{S_C} | S M_S \rangle \\ & \times \langle S_A M_{S_A} 1-m | S M_S \rangle \left\{ \begin{array}{ccc} \frac{1}{2} & \frac{1}{2} & S_A \\ \frac{1}{2} & \frac{1}{2} & 1 \\ S_B & S_C & S \end{array} \right\}. & (D.14) \end{aligned}$$

Using an alternative definition of the $9j$ symbol that couples the quarks differently, we can get a similar expression for the spin overlap for the second diagram of Figure 2.1 which satisfies

$$\langle \chi_{S_B M_{S_B}}^{32} \chi_{S_C M_{S_C}}^{14} | \chi_{S_A M_{S_A}}^{12} \chi_{1-m}^{34} \rangle = (-1)^{1+S_A+S_B+S_C} \langle \chi_{S_B M_{S_B}}^{14} \chi_{S_C M_{S_C}}^{32} | \chi_{S_A M_{S_A}}^{12} \chi_{1-m}^{34} \rangle. & (D.15)$$

Eq. D.15 was used to simplify Eq. 2.7.

Appendix E

Converting to Partial Wave Amplitudes for Models of Meson Decay

The decay amplitudes of the 3P_0 and flux-tube breaking models derived in Sections 2.1 and 2.3, $M^{M_{J_A}M_{J_B}M_{J_C}}$, are given for a particular basis of the final state: $|\theta, \phi, M_{J_B}, M_{J_C}\rangle \equiv |\Omega, M_{J_B}, M_{J_C}\rangle$. Here θ and ϕ are the spherical polar angles of the outgoing momentum of meson B ($\vec{P} \equiv \vec{P}_B$) in the CM frame.

We would prefer to calculate amplitudes for particular outgoing partial waves, $|J, M, S, L\rangle$, since they are what are measured experimentally. Here $|J, M\rangle$ are the quantum numbers of the total angular momentum of the final state, $|S, M_S\rangle$ are the quantum numbers for the sum of the total angular momenta of B and C, and $|L, M_L\rangle$ are the quantum numbers for the orbital angular momentum between B and C.

The formula for the decay width in terms of partial wave amplitudes is different from Eq. 2.5:

$$\Gamma = \sum_{S,L} \Gamma^{SL} \quad (\text{E.1})$$

where

$$\Gamma^{SL} = \frac{\pi P \mathcal{S}}{4 M_A^2} |M^{SL}|^2. \quad (\text{E.2})$$

M^{SL} is a partial wave amplitude, and Γ^{SL} is the partial width of that partial wave.

We use two methods to convert our calculated amplitudes to the partial wave basis [69]: by use of a recoupling calculation, and by use of the Jacob-Wick Formula.

E.1 Converting by a Recoupling Calculation

The recoupling transformation directly relates the bases $|\Omega, M_{J_B}, M_{J_C}\rangle$ and $|J, M, S, L\rangle$:

$$\begin{aligned} |J, M, S, L\rangle &= \sum_{M_{J_B}, M_{J_C}, M_S, M_L} \langle LM_L S M_S | JM \rangle \langle J_B M_{J_B} J_C M_{J_C} | S M_S \rangle \\ &\quad \times \int d\Omega Y_{LM_L}(\Omega) |\Omega, M_{J_B}, M_{J_C}\rangle. \end{aligned} \quad (\text{E.3})$$

In terms of the amplitudes, the net result we want is the transformation

$$\begin{aligned} M^{SL}(P) &= \sum_{M_{J_B}, M_{J_C}, M_S, M_L} \langle LM_L S M_S | J_A M_{J_A} \rangle \langle J_B M_{J_B} J_C M_{J_C} | S M_S \rangle \\ &\quad \times \int d\Omega Y_{LM_L}^*(\Omega) M^{M_{J_A} M_{J_B} M_{J_C}}(\vec{P}). \end{aligned} \quad (\text{E.4})$$

Note that this result holds for any value of M_{J_A} , since $M^{SL}(P)$ is independent of M_{J_A} . If we wanted to avoid favouring one particular value, we could sum over M_{J_A} , and convert the sum on the left side to a factor of $1/(2J_A + 1)$ on the right side.

E.2 Converting with the Jacob-Wick Formula

The Jacob-Wick formula

$$|J, M, S, L\rangle = \sum_{\lambda_B, \lambda_C} \sqrt{\frac{2L+1}{2J+1}} \langle L0S\lambda | J\lambda \rangle \langle J_B\lambda_B J_C - \lambda_C | S\lambda \rangle |J, M, \lambda_B, \lambda_C\rangle \quad (\text{E.5})$$

relates the partial wave basis $|J, M, S, L\rangle$ to the helicity basis $|J, M, \lambda_B, \lambda_C\rangle$, where λ_B and λ_C are the helicities of B and C, respectively. To use it we must first relate the helicity basis to the basis $|\Omega, \lambda_B, \lambda_C\rangle$,

$$|J, M, \lambda_B, \lambda_C\rangle = \sqrt{\frac{2J+1}{4\pi}} \int d\Omega D_{M\lambda}^{J*}(\phi, \theta, 0) |\Omega, \lambda_B, \lambda_C\rangle \quad (\text{E.6})$$

where $D_{M\lambda}^{J*}(\phi, \theta, 0)$ is a rotation matrix, and then choose \vec{P} to lie along the positive z axis (in the CM frame still), so that $\lambda_B = M_{J_B}$, $\lambda_C = -M_{J_C}$, and $|\Omega, M_{J_B}, M_{J_C}\rangle = |\Omega, \lambda_B, -\lambda_C\rangle$.

The final transformation between the amplitudes is

$$\begin{aligned} M^{SL}(P) &= \frac{\sqrt{4\pi(2L+1)}}{2J_A+1} \sum_{M_{J_B}, M_{J_C}} \langle L0S(M_{J_B} + M_{J_C}) | J_A(M_{J_B} + M_{J_C}) \rangle \\ &\quad \times \langle J_B M_{J_B} J_C M_{J_C} | S(M_{J_B} + M_{J_C}) \rangle M^{(M_{J_A} = M_{J_B} + M_{J_C}) M_{J_B} M_{J_C}}(P\hat{z}). \end{aligned} \quad (\text{E.7})$$

Note that M_{J_A} in the calculated amplitude is replaced by $M_{J_B} + M_{J_C}$.

Bibliography

- [1] Particle Data Group, L. Montanet *et al.*, “Review of Particle Properties”, Phys. Rev. D **35**, 1173 (1994) and 1995 off-year partial update for the 1996 edition available on the PDG WWW pages (URL: <http://pdg.lbl.gov/>).
- [2] John Kogut and Leonard Susskind, Phys. Rev. D **11**, 395, (1975).
- [3] Nathan Isgur and Jack Paton, Phys. Rev. D **31**, 2910 (1985).
- [4] Stephen Godfrey and Nathan Isgur, Phys. Rev. D **32**, 189 (1985).
- [5] Richard Kokoski and Nathan Isgur, Phys. Rev. D **35**, 907, (1987).
- [6] Harry G. Blundell and Stephen Godfrey, Phys. Rev. D **53**, 3700 (1996).
- [7] Harry G. Blundell, Stephen Godfrey and Brian Phelps, Phys. Rev. D **53**, 3712 (1996).
- [8] The 3P_0 model of meson decay was first discussed by A. Le Yaouanc, L. Oliver, O. Pène and J.-C. Raynal, Phys. Rev. D **8**, 2223 (1973). See also their book, Reference [68]. For further references to the model, see R. Kokoski, Ph.D thesis, University of Toronto, 1984.
- [9] W. Roberts and B. Silvestre-Brac, Few-Body Systems, **11**, 171 (1992).
- [10] Cameron Hayne and Nathan Isgur, Phys. Rev. D **25**, 1944 (1982).

- [11] Richard N. Zare, Angular Momentum: Understanding Spatial Aspects in Chemistry and Physics (John Wiley & Sons, New York, 1988).
- [12] Stephen Wolfram, Mathematica: A System for Doing Mathematics by Computer, 2nd ed. (Addison-Wesley, Redwood City, 1991). For the flux-tube breaking model of meson decay, FORTRAN code was created using the Mathematica packages Format.m and Optimize.m, written by M. Sofroniou and available from MathSource (URL: <http://www.wri.com/>).
- [13] G. Peter Lepage, J. Comput. Phys. **27**, 192 (1978); “VEGAS - An Adaptive Multi-dimensional Integration Program”, Cornell University Technical Note CLNS-80/447, 1980.
- [14] Paul Geiger and Eric S. Swanson, Phys. Rev. D **50**, 6855 (1994).
- [15] Stephen Godfrey (private communication: Nathan Isgur (private communication)).
- [16] MARK III Collaboration. First reported in a presentation by K.F. Einsweiler, International Europhysics Conference on High Energy Physics, Brighton, U.K., July 20-27, 1983; final analysis presented in R.M. Baltrusaitis *et al.*, Phys. Rev. Lett. **56**, 107 (1986).
- [17] R. Michael Barnett, Goran Senjanović, L. Wolfenstein, and D. Wyler, Phys. Lett. B **136**, 191 (1984); R.S. Willey, Phys. Rev. Lett. **52**, 585 (1984); Howard E. Haber and G.L. Kane, Phys. Lett. B **135**, 196 (1984).
- [18] Michael P. Shatz, Phys. Lett. B **138**, 209 (1984).
- [19] Kuang-Ta Chao, Commun. Theor. Phys. **3**, 757 (1984).
- [20] Sandip Pakvasa, Mahiko Suzuki and S.F. Tuan, Phys. Lett. B **145**, 135 (1984).

- [21] Seiji Ono, Phys. Rev. D **35**, 944 (1987).
- [22] Michael S. Chanowitz and Stephen R. Sharpe, Phys. Lett. B **13**, 413, (1983).
- [23] Kuang-Ta Chao, Commun. Theor. Phys. **24**, 373 (1995).
- [24] P.D. Barnes *et al.*, Phys. Lett. B **309**, 469 (1993).
- [25] Serpukhov-Brussels-Los Alamos-Annecy (LAPP) Collaboration, D. Alde *et al.*, Phys. Lett. B **177**, 120 (1986).
- [26] B.V. Bolonkin *et al.*, Nucl. Phys. B **309**, 426 (1988).
- [27] D. Aston *et al.*, Phys. Lett. B **215**, 199 (1988).
- [28] DM2 Collaboration, J.E. Augustin *et al.*, Phys. Rev. Lett. **60**, 2238 (1988).
- [29] BES Collaboration, “Study of $\xi(2230)$ in J/ψ decays”, presented at the 17th International Symposium on Lepton Photon Interactions, Beijing, August 10-15, 1995.
- [30] Stephen Godfrey, Richard Kokoski and Nathan Isgur, Phys. Lett. B **141**, 439 (1984).
- [31] Seiji Ono, O. Pène and F. Schöberl, Prog. Theor. Phys. **74**, 545 (1985).
- [32] Stephen Godfrey and Richard Kokoski, Phys. Rev. D **43**, 1679 (1991); Stephen Godfrey (private communication).
- [33] See for example John Gillespie, Final-State Interactions (Holden-Day, San Francisco, 1964).
- [34] Albert Messiah, Quantum Mechanics, translated from the French by G.M. Temmer (vol. 1) and J. Potter (vol. 2) (John Wiley & Sons, New York, 1961-5).

- [35] Enrico Fermi, Elementary Particles (Yale University Press, New Haven, 1951).
- [36] A. Courau *et al.*, Nucl. Phys. B **271**, 1 (1986).
- [37] F.E. Low, Phys. Rev. **96**, 1428 (1954); M. Gell-Mann and M.L. Goldberger, Phys. Rev. **96**, 1433 (1954); Henry D.I. Abarbanel and Marvin L. Goldberger, Phys. Rev. **165**, 1594 (1968).
- [38] CELLO Collaboration (H.J. Behrend *et al.*), Z. Phys. C **56**, 381 (1992).
- [39] J. Boyer *et al.*, Phys. Rev. D **42** 1350 (1990).
- [40] TPC/Two Gamma Collaboration (H. Aihara *et al.*), Phys. Rev. Lett. **57**, 404 (1986).
- [41] Some of the data shown for the $\gamma\gamma \rightarrow \pi\pi$ work was downloaded from the Durham/RAL HEP Reaction Data Database at
<http://durpdg.dur.ac.uk/HEPDATA>.
- [42] Some of the data shown for the $\gamma\gamma \rightarrow \pi\pi$ work was obtained from D. Morgan, M.R. Pennington and M.R. Whalley, J. Phys. G **20**, A1 (1994).
- [43] Ted Barnes, Kevin Dooley and Nathan Isgur, Phys. Lett. B **183**, 210 (1987).
- [44] D. Morgan and M.R. Pennington, Phys. Lett. B **272**, 134 (1991).
- [45] Johan Bijnens and Fernando Cornet, Nucl. Phys. B **296**, 557 (1988).
- [46] John F. Donoghue, B.R. Holstein and Y.C. Lin, Phys. Rev. D **37**, 2423 (1988).
- [47] S. Bellucci, J. Gasser and M.E. Sainio, Nucl. Phys. B **423**, 80 (1994); Erratum **431**, 413 (1994).
- [48] D. Morgan and M.R. Pennington, Phys. Lett. B **192**, 207 (1987).

- [49] John F. Donoghue and Barry R. Holstein, Phys. Rev. D **48**, 137 (1993).
- [50] Eric S. Swanson, Ann. Phys. (N.Y.) **220**, 73 (1992).
- [51] Z. Li, M. Guidry, T. Barnes and E.S. Swanson, “I=0, 1 $\pi\pi$ and I=1/2 $K\pi$ Scattering Using Quark Born Diagrams”, Preprint hep-ph/9401326, 1994.
- [52] Eric S. Swanson (private communication).
- [53] T. Barnes and E.S. Swanson, Phys. Rev. D **46**, 131 (1991).
- [54] U. Nguyen-Khac and J. Six, in Analysis of Scattering and Decay, edited by M. Nikolić (Gordon and Breach, New York, 1968).
- [55] John Weinstein and Nathan Isgur, Phys. Rev. D **41**, 2236 (1990).
- [56] John Weinstein, “The Multichannel Quark Model”, Preprint UMHEP 96-021, University of Mississippi, nucl-th/9606037, 1996.
- [57] William H. Press *et al.*, Numerical Recipes in C: The Art of Scientific Computing, 2nd ed., (Cambridge University Press, Cambridge, 1992).
- [58] W. Hoogland *et al.*, Nucl. Phys. B **126**, 109 (1977).
- [59] J.P. Prukop *et al.*, Phys. Rev. D **10**, 2055 (1974).
- [60] K.N. Mukhin *et al.*, Zh. Eksp. Teor. Fiz. **32**, 616 (1980).
- [61] L. Rosselet *et al.*, Phys. Rev. D **15**, 574 (1977).
- [62] P. Estabrooks and A.D. Martin, Nucl. Phys. B **79**, 301 (1974).
- [63] S.D. Protopopescu *et al.*, Phys. Rev. D **7**, 1279 (1973).

- [64] Crystal Ball Collaboration (J.K. Bienlein for the collaboration) in Proceedings of the IX International Workshop on Photon-Photon Collisions, edited by D. Caldwell and H.P. Paar (World Scientific, Singapore, 1992), p. 241.
- [65] Crystal Ball Collaboration (H. Marsiske *et al.*), Phys. Rev. D **41**, 3324 (1990).
- [66] C. Edwards *et al.*, Phys. Lett. B **110**, 82 (1982).
- [67] David Griffiths, Introduction to Elementary Particles (John Wiley & Sons, New York, 1987).
- [68] Alain Le Yaouanc, Lluis Oliver, Olivier Pène and Jean-Claude Raynal, Hadron Transitions in the Quark Model (Gordon and Breach Science Publishers, New York, 1988).
- [69] Suh Urk Chung, “Spin Formalisms”, Technical Note CERN 71-8, CERN, 1971; Jeffrey D. Richman, “An Experimenter’s Guide to the Helicity Formalism”, Technical Note CALT-68-1148, California Institute of Technology, 1984; M. Jacob and G.C. Wick, Ann. Phys. **7** 404 (1959).